Characterization of Traffic-Related Air Pollutants near a Major Roadway in Albuquerque Using a Mobile Monitoring Approach

Lyndsey Banks

A thesis

submitted in partial fulfillment of the

requirements for the degree of

Master of Science

University of Washington

2013

Committee:

Christopher Simpson

Timothy Larson

Michael Yost

Program Authorized to Offer Degree:

Occupational and Environmental Exposure Sciences

University of Washington

Abstract

Characterization of Traffic-Related Air Pollutants near a Major Roadway in Albuquerque by Using a Mobile Monitoring Approach

Lyndsey Banks

Chair of the Supervisory Committee:

Associate Professor Christopher D. Simpson, PhD, MSc

Department of Environmental and Occupational Health Sciences

In order to assess the characteristics of air pollutants in proximity to major roadways, a mobile monitoring campaign took place using the University of Washington Center for Clean Air Research (CCAR) mobile instrument platform designed to measure concentrations of particles and gases while continuously on the move. The CCAR platform followed a predetermined route in Albuquerque, New Mexico, over seven sequential days in April, 2012 during the evening commute timeframe. A series of roads, parallel to each other and Interstate 40, and beginning approximately 30 meters from the interstate, were traversed at least two times per observation day in an effort to tease-out changes in the chemical and physical properties of traffic-related pollutants as they age with distance from roadway. Metrics obtained during the monitoring campaign include: light scattering coefficients, light absorption coefficients, particle-bound polycyclic aromatic hydrocarbons (PAHs), particle optical diameters, particle number concentrations, ozone (O_3), nitric oxide (NO), oxides of nitrogen (NO_x), carbon monoxide (CO), carbon dioxide (CO_2), integrated volatile organic compounds (VOCs) and location.

Spatially resolved measurements were obtained for several of these reactive species as well as non-reactive tracers of vehicle exhaust. Two distinctive dispersion patterns were captured: 1) a symmetric pattern on either side of the interstate associated with low wind speeds; and 2) an asymmetric pattern with a dominant downwind influence. An expected decline with distance from

roadway for several traffic-related pollutants, indicative of the dispersion process, was observed for the downwind near-roadway region. Additionally, an expected decrease in O_3 nearing the interstate was observed due to its consumption by NO from roadway emissions.

The innovative use of mobile monitoring allows for improved estimates of near-roadway gradients in air pollution, when compared with traditional stationary site sampling. Spatially resolved measurements allow for additional insight into the physical and chemical aging phenomena of traffic-related pollutants in the vicinity of major roadways.

Table of Contents

List of Figures

List of Tables

Acknowledgment

The author would like to thank Dr. Christopher Simpson, Dr. Michael Yost and Dr. Timothy Larson for their guidance and support. Additional acknowledgements go to Kris Hartin and Timothy Gould for their efforts on the mobile monitoring campaign. Extended thanks go to the entire University of Washington Center for Clean Air Research (CCAR) Project 1 Research Group.

This publication was made possible by USEPA grant (RD-83479601-0). Its contents are solely the responsibility of the grantee and do not necessarily represent the official views of the USEPA. Further, USEPA does not endorse the purchase of any commercial products or services mentioned in the publication.

Background and Significance

Air pollutants encompass a diversity of chemicals, among which diesel and gasoline vehicle exhaust components are some of the highest priority air toxics nationally. These vehicle emissions consist of complex chemical mixtures, encompassing both particulate and vapor phase components, which undergo further physical and chemical transformations as they age in the environment. Human health effects due to exposure to these components throughout the aging process may, therefore, vary greatly due to the differences in physical and chemical properties of the agents at the various aging stages. With the literature reporting statistically significant associations between proximity to roadways and various health effects, including cancer, asthma and additional respiratory symptoms, (Peters et al., 2004; Dockery et al., 2007), it, therefore, becomes critical to further our understanding of the near-roadway pollutant gradients.

Many studies have shown statistically significant associations between proximity to major roadways and adverse health effects. In the United States alone, an estimated 45 million residents live within 100 meters of a highway (HEI Panel, 2010). Studies have shown that concentrations of pollutants associated with vehicle emissions decrease exponentially with distance from major traffic areas, with traffic-related pollutants being elevated above background concentrations 50 to 1500 meters from major highways, depending on the weather and particular pollutant (Peltier et al., 2011). Quantification of these traffic-related pollutants is, therefore, critical in estimating their impact on the health of local communities. Subsequently, development of temporal and spatial models of air pollutants surrounding roadways has been significant in furthering our understanding of the health impacts associated with traffic-related exposures.

Pollution from vehicles occurs through the formation of by-products during the combustion process, as well as through incomplete fuel combustion and vaporization. Motor vehicle emissions

primarily consist of large quantities of carbon dioxide (CO_2), carbon monoxide (CO), hydrocarbons, oxides of nitrogen (NO_x), particulate matter, and mobile-source air toxics (MSATs), which include substances such as benzene, aldehydes and various trace metals (e.g. Cu, V). There are also secondary by-products to consider, such as ozone (O_3) and secondary aerosols.

Additional chemical and physical processes at and near roadways can modify the properties of these original pollutants and, in turn, modify their health effects. These aging processes typically occur through one of three major pathways: reactions of primary emitted gases with entrained oxidants during mixing of exhaust with ambient air, aerosol dynamic processes (condensation, evaporation, coagulation) affecting the primary emitted particles, and new particle production through chemical reactions during plume dilution (Pirjola et al., 2006). Vehicle exhaust emission transformations occur both during the initial plume dilution and during the subsequent mixing with ambient air. The relatively high temperatures and concentrations associated with tail pipes foster environments which favor chemical reactions and condensation processes.

Nitrogen oxide compounds are particularly useful in characterizing the chemical aging process of vehicle emissions. During combustion, the nitrogen bound in the fuel is released as a free radical and ultimately reacts with oxygen to form nitrogen dioxide (NO_2) or nitric oxide (NO) (Beer et al., 1981). Typically, NO_x (NO_x = NO + NO_2) from combustion sources is initially in the form of NO, and then undergoes atmospheric oxidation for conversion into the more toxic NO_2. A major pathway for conversion of NO to NO_2 in the atmosphere is by reaction with ozone, whereby at high NO concentrations, such as occurs near roadways, the reaction is ozone limited. Corresponding ozone depletion can, therefore, also be used to determine the aging of traffic-related pollution. Although, ozone can be depleted by a number of free radicals, the NO radical is of interest in the aging process.

Particulate matter emissions from road vehicles include tailpipe emissions and emissions due to wear and tear of vehicle parts, as well as re-suspension of road surface dust due to vehicle induced turbulence (Pant et al., 2013). Exhaust emissions contribute primarily to ultrafine particles, those less than 0.1 μm in diameter. Changes in ultrafine particulate matter with distance from roadways have been noted in the literature (Pirjola et al., 2006, Zhu et al., 2002), with greater average particle size observed with increasing distance from the source. It is believed that particle growth through chemical and physical surface modifications is responsible for these changes in the particle size distribution. In addition to photochemistry, meteorology and aerosol thermodynamics also play important roles in governing particulate matter composition and size.

The spatial extent of pollutant types is influenced by both the respective pollutant properties, as well as background concentration, and is commonly defined in the literature by comparing downwind concentrations with that of the upwind "background" concentrations. Inert pollutants, such as CO, show a decrease in concentration downwind of a major roadway as a result of dilution with ambient air. The near-roadway profiles of reactive pollutants, however, are influenced by the rate of chemical reaction in addition to dilution with surrounding air. This typically results in a rapid decrease in concentration downwind of the roadway. Those pollutants dominated by formation processes, such as NO_2, however, are slowed in their dilution and, subsequently, decrease at a more gradual rate (Zhou et al., 2007).

The effects of noise barriers on the pollution levels in the surrounding near-roadway areas are commonly discussed throughout the literature. Notably lower concentrations have been observed in areas which extend downwind behind these barriers, whereby reductions up to 50% or more in pollutant levels have been noted (Finn et al., 2010). This effect has been explained by a combination of upward deflection of airflow, increased vertical mixing, in addition to an enhanced initial mixing due to turbulence on the roadway as a result of the barrier. These well-mixed lower concentration zones

behind the barriers can extend from 3 to 12 wall heights downwind (Baldauf et al., 2008b). Furthermore, noise barriers inhibit lateral movements of pollutants and, subsequently, more elevated concentrations on-road may be detected. A study of the impact of noise barriers on near-road air quality conducted by Baldauf et al. (2008b), however, also observed elevated concentrations of several pollutants behind the barrier, whereby concentrations increased between 70 and 100 meters of the road. It was believed these elevated concentrations to be a result of traffic activity on the residential roads behind the barrier. Considerations as to the noise barriers and structures on either side of the roadway may, therefore, shed some additional insight into the dispersion process.

Recent developments in the literature include the use of mobile platforms for characterizing pollutant mixtures in the vicinity of roadways (Clements et al, 2009; Pirjola et al., 2005, Weijers et al., 2004). Measurement results have demonstrated the temporal and spatial impact of traffic emissions on near-road air quality. Profiles of fine and ultrafine particulates, carbon monoxide, oxides of nitrogen and black carbon, in the vicinity of roadways, have all been studied throughout the literature in several cities across the world (Clements et al., 2009). Pollutant profiles typically remain elevated near roadways and exponentially decrease to background levels with distance from roadway (Clements et al., 2009). Studies have relied upon mobile platforms that have required stopping at near-road locations in order to capture concentrations as limited by instrument response. Mobile monitoring platforms with more rapid sampling instruments, however, have led to innovations in sampling with high temporal and spatial resolution. Hagler et al. (2010), for instance, conducted a high resolution mobile monitoring study of a small 3 by 3 kilometer near-roadway region in Durnham, North Carolina. This study noted that background concentrations were not reached until a distance of approximately 2600 m downwind and up to 600 m upwind. Baldauf et al.'s (2008b) noise barrier studies also characterized with high spatial resolution a near road environment transect spanning 3600 meters from a major roadway. Little research, however, has been done on characterizing the behavior of the pollutant mixture as a whole

and studies have typically focused on single stationary site samples along a perpendicular road transect at broader spatial scales, as opposed to a clearly defined smaller scale gradient neighborhood (Weijers et al., 2004; Zhu et al., 2002; Zwack et al., 2011a).

Specific Aims

This particular study is a sub-component of a larger Center for Clean Air Research (CCAR) exposure mapping project with an overreaching aim of characterizing gases and particles near roadways, in multiple cities, for future exposure assessment in health effect studies. The overall objective of this specific study is, therefore, to characterize the chemical and physical aging of air pollutant components as they are transported away from a major roadway in Albuquerque, New Mexico. By examining the spatial extent of several traffic-related pollutants, we hope to gain insight into near-roadway pollutant gradients and their subsequent potential impact on human health.

More specifically we aim to:

1) Obtain temporally and spatially resolved measurements of traffic-related pollutants through the use of mobile monitoring techniques
2) Characterize the spatial gradients of 'non-reactive' (e.g. carbon monoxide, black carbon, large particle sizes (> 1 μm)) vehicle emitted pollutant species as a function of distance from roadway
3) Characterize the spatial gradients of 'reactive' (e.g. ozone, nitric oxide, ultrafine particles) vehicle emitted pollutant species as a function of distance from roadway

Mobile Monitoring Campaign

In order to assess the characteristics of air pollutants in proximity to roadways, a mobile monitoring campaign took place using an instrument platform developed by the University of Washington (UW) Center for Clean Air Research (CCAR) that was designed to measure concentrations of particles and gases while continuously on the move. The CCAR platform followed a predetermined route in Albuquerque, New Mexico. Mobile monitoring offers particular advantages over sampling at stationary sites. In comparison to sampling at a few stationary sites, the higher number of measurements obtained through mobile sampling provides information that facilitates disentangling the sources of a variety of pollutant concentrations over spatial gradients. Additionally, real-time mobile measurements are able to capture the rapid dynamics of atmospheric processes near roadways. Mobile monitoring also requires less resources than deploying many stationary site continuous monitors at many different locations.

Albuquerque was selected as the location for the current study primarily due to opportunistic reasons, whereby the prevailing wind patterns are ideal for capturing both upwind and downwind variations in air pollutants surrounding a major roadway, Interstate 40 (Coronado Freeway). In addition, the specific location in Albuquerque allows for the definition of a clear gradient due to the parallel nature of the neighboring roads on either side of the interstate. Two gradient areas were established for the purpose of this study, one on each of the north and south sides of Interstate 40 (I-40), as shown in Figure 1. This theoretically ensured that both upwind and downwind gradients were captured during the monitoring campaign. The measurements in Albuquerque additionally allow for pollutant analysis at a smaller spatial scale than previously studied cities.

The entire mobile monitoring campaign for Albuquerque took place over seven sequential days in April, 2012 (April 18, 2012 through April 24, 2012). A series of roads, parallel to each other and the

interstate, and beginning approximately 30 meters from the interstate, were traversed at least two times per observation day in an effort to tease-out changes in air pollutant concentrations and composition associated with "aging" of fresh traffic related air pollution. Measurements were taken during the evening commute, between approximately 3pm and 7pm (Table 1). We chose to monitor during the evening commute exclusively because this represents a period of maximum roadway emissions, when the near roadway gradients are likely to be strong and not confounded by the rapid changes in the atmospheric mixing height that occur during the morning commute.

Table 1 - Approximate Sampling Periods of Gradient Sites during Mobile Monitoring Campaign

Day	Sampling Start Time	Sampling Stop Time
April 18	17:13	19:00
April 19	15:11	17:53
April 20	15:28	18:33
April 21	16:02	18:52
April 22	15:02	19:08
April 23	15:12	18:26
April 24	17:18	18:25

For the purpose of analysis, a 'south' (Figure 2) and a 'north' (Figure 3) gradient route were established, each on the respective north and south sides of the interstate of interest. The north gradient route consists of seven roads approximately parallel to I-40 (street names: Childers, Field, Lester, Luthy, Marron, McKee and an additional service road along the edge of the interstate). The south gradient consists of four roads approximately parallel to I-40 (street names: Winter, Summer, Spring and Mountain Roads). The major roadway of interest, I-40, is approximately an eight-lane highway. The interstate passing the north gradient site is bordered by a noise barrier on the northern side of the roadway. The interstate passing the south gradient location is contained by noise barriers, of varying height, on either side of the interstate. Noise barriers along the I-40 in Bernalillo County can range from 10 to 18 feet in height (U.S. Department of Transportation, 2012).

Figure 1 - Locations of 10 Second Measurements for the Entire Mobile Sampling Campaign *(approximate gradient site locations outlined in red).*

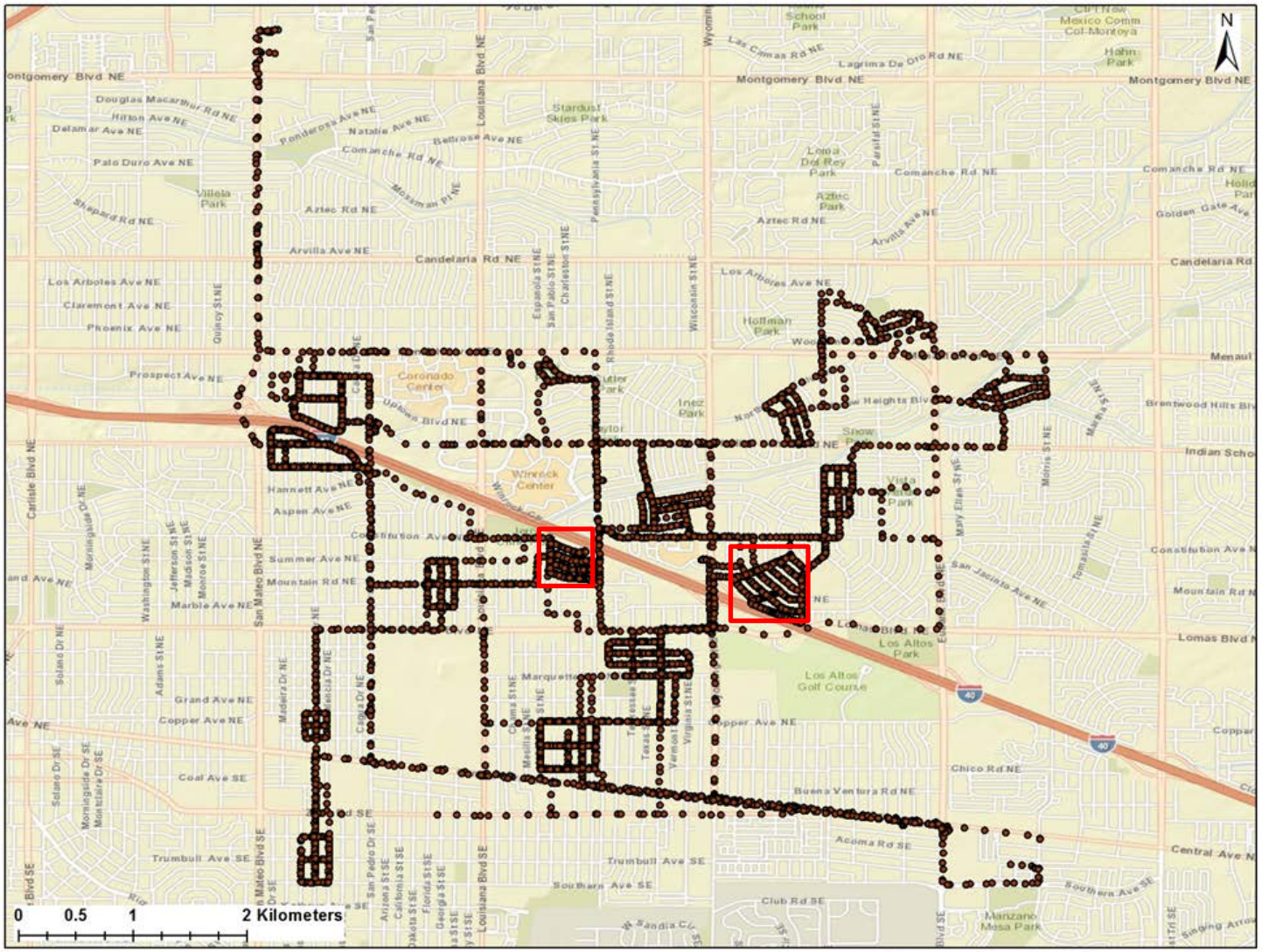

Map prepared by Lyndsey Banks 05/11/2013 using ArcMap10
CCAR Project 1 Mobile Monitoring Campaign Albuquerque, NM

Figure 2 - South Gradient Site

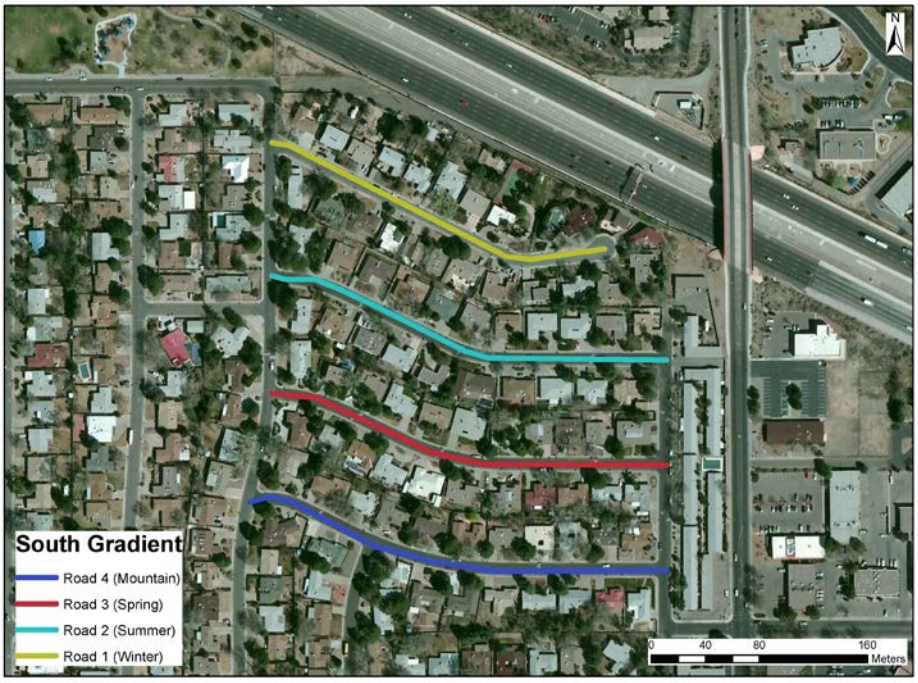

Figure 3 - North Gradient Site

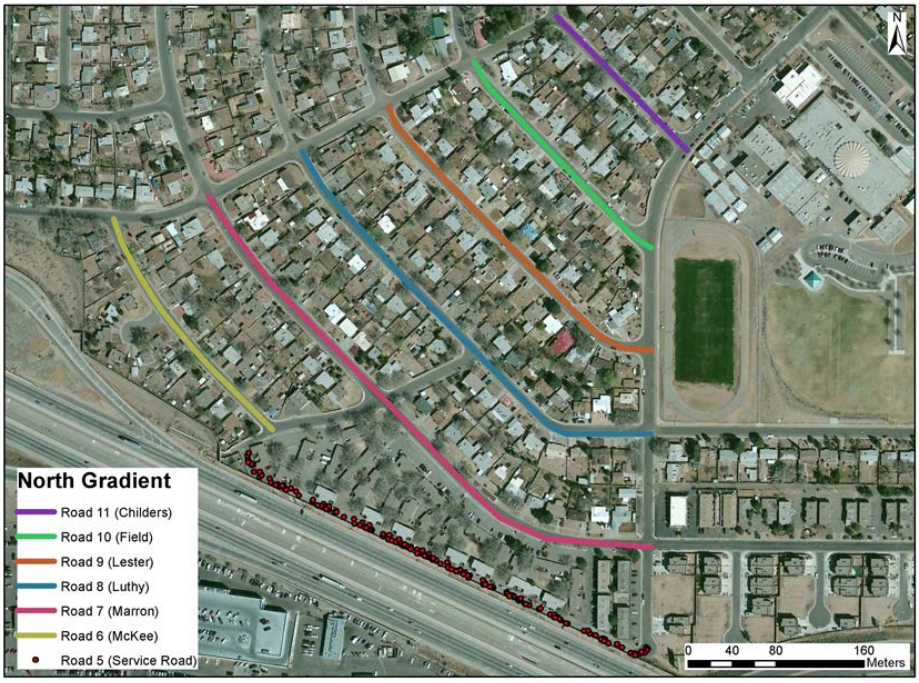

Mobile Instrument Platform

The mobile monitoring platform was developed by the UW CCAR research group as part of a larger effort to understand urban exposures to various air pollutants. It is described in more detail below. This thesis focused on application of this technology for near-roadway data collection and interpretation.

Instrument Manifold

The mobile monitoring campaign was conducted using a gasoline powered Ford Escape (model year 2012) with the sampling inlets, a separate gas and particle inlet, positioned on the driver's side of the vehicle. The instrument platform was located inside the vehicle and connected to sample inlet lines which entered the vehicle through the otherwise sealed left-rear window. The inlets were secured to the top of the vehicle to face forward during the sampling, in order to minimize self-pollution. No dryer was used for dehumidification at the inlet, due to the relatively dry conditions in Albuquerque. The monitoring route was driven at an approximate speed of 22 miles per hour. This speed ensured that the face velocity at the inlets provided pseudo isokinetic sampling. Monitoring instruments that were used in this mobile system are listed in Table 2 along with the measurements that were obtained from the mobile platform.

The particle inlet was made from stainless steel and copper tubing in order to minimize particle loss resulting from deposition due to electrostatic attraction. This inlet draws the sample directly into the GRIMM Aerosol Spectrometer and Nanocheck attachment through a small stainless steel tube in the center of a larger diameter metal Y-fitting where the sample flow for other instruments is separated from that of the GRIMM sample. The Radiance Nephelometer blower was used to draw the air sample at a rate of 7 L/min past this Y connection through a stainless steel manifold. This manifold includes eight potential ports, four on each side, where the other particle instruments were connected to draw

their design flow rates. Unused ports were capped, while the Radiance Nephelometer drew its sample from the opposite end of this manifold from the inlet. The temperature/relative humidity, CO and CO_2 sensors were located within the housing of the manifold.

A separate gas inlet was made from Teflon tubing and this line branched to the analyzers for NO, NO_x, O_3, and volatile organic compounds (VOCs). Each of these devices pulled their own sample with a total gas inlet flow of 5 L/min at the Teflon tube. The entire sampling system was run at 120 volt auxiliary power using inverters to transform the source power of 12 volt direct current (DC) to alternating current (AC). Source power consisted of two extra 12 volt batteries in parallel, in addition to the vehicle's accessory power system.

Table 2 - Mobile Measurements Taken During Monitoring Campaign

Parameter	Instrument
Particle Light Scattering Extinction Coefficient	Radiance Nephelometer M903
Particle-bound Polycyclic Aromatic Hydrocarbons (PAHs)	EcoChem PAS 2000CE
Ultrafine Particle Counts	TSI P-Trak Model 8525 Ultrafine Particle Counter
Black Carbon Ultraviolet Absorbing Particulate Matter (UVPM)	Magee Scientific microAeth Model AE52
31 Distinct Sizes of Particle Counts Total Particle Number Concentration Mean Particle Diameter	GRIMM Portable Aerosol Spectrometer and Dust Monitor Model 1.109 GRIMM Portable NanoCheck 1.320
Nitric Oxide (NO) Oxides of Nitrogen (NO_x) Nitrogen Dioxide (NO_2) (concentration by difference)	2B Technologies Model 410 Nitric Oxide Monitor 2B Technologies Model 410 Nitric Oxide Monitor with NO_2 Converter
Ozone (O_3)	JSC Optec 3.02 P-A Chemiluminescent Ozone Analyzer
Carbon Monoxide (CO)	Langan CO Monitor T15N
Volatile Organic Compounds (VOCs)	Inficon 2020ppbPro Portable Photoionization Detector
Carbon Dioxide (CO_2)	Senseair CO_2 Engine K-30-FS Sensor
Visual Route Record	WebCam
Positioning and Real-Time Tracking	Garmin GPS

All data logging was time synchronized to LabVIEW 2010 before sampling. LabVIEW was programmed with a 10 second data buffer in which data was obtained at the respective collection rate for each instrument and followed by a subsequent “sweep” where the most recent 10 second moving average of the data collected was written to a file. In some occurrences, LabVIEW logging failed for a particular instrument. In this case, the data was downloaded directly from the respective instrument’s internal memory. This data was termed ‘externally downloaded’.

Figure 4 -Eight Port Stainless Steel Manifold

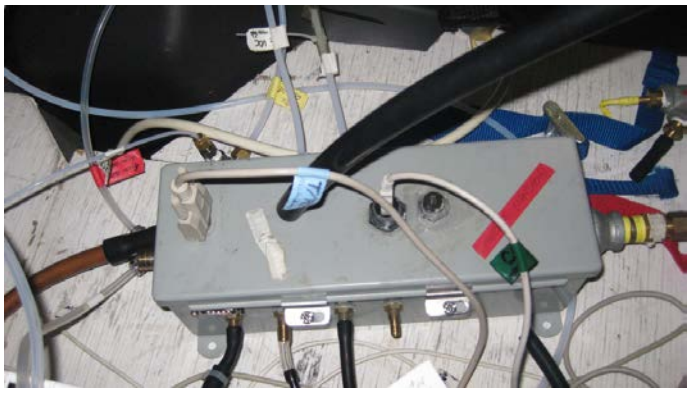

Figure 5 - Instrument Platform in Vehicle

Figure 6 –Sampling Inlets

Data Processing

Initial processing of mobile monitoring data is difficult in that, due to the multidimensional nature of the data, potential biases, such as the sampling of a single vehicle plume, are unavoidable. As an initial step, user defined algorithms were produced in order to flag data resulting from instrument failures, platform errors or other instrument/manifold problems. All data with a platform flag was omitted from the dataset for analysis due to the flag corresponding to a lack of GPS coordinates, rendering the data spatially irrelevant. Flags generated for individual instruments were further used to exclude data from the final dataset. Once the flagged data was removed, further qualitative analysis was performed by generating time series plots (Appendix A) of data on a daily basis using STATA 11.2. All data was uploaded into the statistical software in order to facilitate the manipulation of such a large dataset. Unusually high data points or what appear to visually be unusual incidents were kept within the dataset for this analysis. Further steps would involve video analysis using the video footage recorded throughout the monitoring campaign in order to appropriately identify and establish criteria for removal of such unusual data points.

A complete summary of each individual instrument, along with the criteria for removing respective data points of the final dataset can be seen under the respective instrument summaries in the following pages. Table 3 below summarizes the final dataset for the entire Albuquerque mobile monitoring campaign. During the Albuquerque sampling campaign, a total of 11,142 sets of mobile measurements were collected at ten second intervals, with approximately 22% of these measurements corresponding to data collected on the gradient site roadways.

Table 3 - Final Dataset Completeness Summary for the Entire Albuquerque Monitoring Campaign

	Percent Missing (%)							
Variable	**All Days**	**18-Apr**	**19-Apr**	**20-Apr**	**21-Apr**	**22-Apr**	**23-Apr**	**24-Apr**
NO	8.5	8.6	12	22	6.9	0.44	2.5	1.5
NOx	10	9.5	12	23	11	1.1	4.5	3.5
VOC	30	100	100	21	7.9	2.7	4.1	3.4
CO_2	5.8	4.6	4.1	17	4.8	0.33	1.7	0.77
O_3	17	4.6	6.1	17	4.8	0.33	1.7	74
Particle-bound PAHs	5.9	4.6	4.1	17	4.8	0.33	1.7	0.77
Black Carbon	17	45	18	23	19	13	6.2	3.2
Delta Carbon	17	45	18	23	19	13	6.2	3.2
Light Scattering Extinction Coefficient	34	35	38	42	33	32	28	26
P-Trak Ultrafine Particles	14	56	14	22	14	0.44	3.4	0.77
GRIMM 0.25 - 1.0µm	11	19	14	25	15	0.67	3.7	0.77
GRIMM 1.0 - 2.5µm	12	20	16	26	16	0.78	3.7	0.77
GRIMM 3.0 - 10µm	12	20	16	26	16	0.78	3.7	0.77
GRIMM Nanocheck Conc. (0.025 – 0.3µm)	14	23	21	21	28	2.4	5.3	2.3
GRIMM Nanocheck Median Diam. (0.025 – 0.3µm)	14	23	21	21	28	2.4	5.3	2.3

Instrument Summaries

Instrument: 2B Technologies Model 410 Nitric Oxide Monitor with NO_2 Converter

Parameters: NO concentration (ppb); NOx concentration (ppb) & NO_2 concentration by difference (ppb)

Principle of operation: The instrument operates via continuous titration with ozone, whereby the depletion of ozone is measured using the absolute method of UV absorbance. The NO Monitor is used in combination with the NO_2 monitor, a heated molybdenum converter, for converting NO_2 to NO. The NO_2 concentration is obtained from the difference in the NO_x and NO measurement.

Range of Detection: 0 – 2,000 ppb, precision of ± 1.5 ppb

Limit of detection: 2 ppb

Time/Measurement: 10 sec

Flow Rate: 1 L/min

Data Processing: All measurements maintained for analysis (platform flagged data omitted only). Negative values were maintained in order to observe the relative change of the pollutants. [Appendix A1 and A2]

Instrument: JSC Optec 3.02 P-A Chemiluminescent Ozone Analyzer

Parameters: Ozone (ng/m^3)

Principle of operation: Ozone concentrations obtained via chemiluminescence, whereby the ozone molecules react with a proprietary solid-phase reagent, resulting in emission of light at 560 nm. The emitted light is detected by a photomultiplier tube and the resultant digital signal is linearly proportional to the concentration of ozone.

Range: 0 – 255 ppb

Accuracy: 0.5 ppb

Time/Measurement: 30 sec

Flow Rate: 1.8 L/min

Data Processing: Measurements below 0 ppb were omitted from the final dataset. Additionally, measurements with out of range sensor values were removed. [Appendix A3]

Instrument: Senseair CO_2 Engine K-30 Sensor

Parameters: Carbon dioxide (ppm)

Principle of operation: The K-30-FS is a nondispersive infrared (NDIR) sensor, whereby an optical filter removes all wavelengths of light other than that of the exact wavelength absorbed by CO_2 prior to detection.

Range: 0 – 10000 ppm

Sensitivity: ± 20 ppm; ± 1% of measured value

Accuracy: ± 30 ppm; ± 5% of measured value

Time/Measurement: 20 sec

Flow Rate: 0 L/min; 13.2 L/min flow to manifold

Data Processing: Concentrations less than or equal to 0 ppm were omitted from the final dataset. [Appendix A4]

Instrument: Langan CO Monitor T15N

Parameters: Carbon monoxide (ppm)

Principle of operation: CO is detected in an electrochemical cell, which is exposed to ambient air by means of a diffusion hole.

Range: 0 to 1000 ppm

Resolution: 0.05 ppm

Time/Measurement: ≤ 30 sec

Flow Rate: 0 L/min

Data Processing: All CO data was omitted from the final dataset due to having obtained unrealistic values, likely a result of electrical interference or improper instrument calibration.

Instrument: TSI P-TRAK Model 8525 Ultrafine Particle Counter

Parameters: Ultrafine particle counts (particles/cm^3)

Principle of operation: A built-in pump draws particles through a saturator tube, mixing particles with isopropyl alcohol vapor. The mixture then passes through a condenser tube, causing particles to grow into larger droplets, whereby they become large enough to scatter light. A laser is then used to produce flashes of light which are detected by a photo-detector. A diffusion screen with a 50 nm cut point at the given flow rate was installed on the instrument inlet.

Range: 0.05 – 1 µm; 0 – $5x10^5$ particles/cm^3

Time/Measurement: 1 min

Flow Rate: 0.7 L/min

Data Processing: Measurements with particle counts equal to or less than 0 particles/cm^3 were excluded from the final dataset. Externally downloaded data was used for April 24, 2012. For all other days, LabVIEW data was used. [Appendix A5]

Instrument: GRIMM Portable NanoCheck 1.320

Parameters: Total particle number concentration (particles/cm^3); Mean particle diameter (nm)

Principle of operation: A unipolar diffusion charger, a condenser, plus an aerosol faraday cup electrometer are used in combination for continuous nanoparticle detection. The condenser acts as an ion trap and measures the total current. The current is essentially proportional to the product of particle concentration and mean diameter.

Particle Range: $5x10^2$ to $5x10^5$ particles/cm^3; 25 to 300 nm (0.025 – 0.3 µm)

Accuracy: ± 5% for diameter and concentration

Time/Measurement: 10 sec

Flow Rate: 1.2 L/min

Data Processing: Measurements with negative values were omitted from the final dataset. In addition, particle diameters outside of the instrument's detection range (25 to 300 nm) were removed. Total particle counts were removed if the corresponding 10 second particle diameter measurement had been removed from the dataset for that time. [Appendix A6 and A7]

Instrument: GRIMM Portable Aerosol Spectrometer and Dust Monitor Model 1.109

Parameters: 31 distinct sizes (0.25 to 32 µm) of particle counts (particles/cm^3)

Principle of Operation: Light scattering of particles with a laser diode light source operating in the visible range (655 nm). The particle size is proportional to the intensity of the detected scattered light.

Particle Range: 1 to $2x10^6$ particles/cm^3; 0.25 to 32 µm

Time/Measurement: 10 sec

Flow Rate: 1.2 L/min

Data Processing: Measurements with negative values were omitted from the final dataset. Particle counts were further aggregated into three separate size bins in order to facilitate analysis (GRIMM 0.25 – 1.0 µm; GRIMM 1.0 – 2.5 µm; GRIMM 3.0 – 10 µm). Particle counts less than or equal to zero were removed for the smallest GRIMM bin size (GRIMM 0.25 – 1.0 µm). Additional data was removed from

the medium (1.0 – 2.5 µm) and large (3.0 - 10 µm) particle sized bins if the smallest (0.25 – 1.0 µm) GRIMM bin size had a value less than or equal to zero. [Appendix A8, A9 and A10]

Instrument: Magee Scientific microAeth Model AE52

Parameters: Black carbon concentration (ng/m^3); Ultraviolet Particulate Matter (UVPM) (ng/m^3)

Principle of operation: Real-time analysis measuring the rate of change of absorption of transmitted light due to the continuous collection of aerosol deposit on a filter. Measurements in the infrared range, at 880 nm, are interpreted as concentration of black carbon (BC). Ultraviolet (UV) analysis, at 370 nm, corresponds to that of cigarette smoke, wood and coal smoke, and other aromatic organic compounds.

Range: 0 – 1 mg BC/m^3

Resolution: 0.001 µg BC/m^3

Precision: ± 0.1 µg BC/m^3 (1 min avg., 0.15 L/min flow rate)

Time/Measurement: 10 sec

Flow Rate: 0.15 L/min

Data Processing: Data points with missing values for both black carbon and UVPM were removed. Values out of range (< 0 mg/m^3) were also removed. An additional delta black carbon variable was generated by taking the difference between the corresponding 10 second UVPM and black carbon measurements. [Appendix A11 and A12]

Instrument: Radiance Nephelometer M903

Parameters: Particle light scattering extinction coefficient (m^{-1})

Principle of Operation: Particle light scattering is measured at a single wavelength, whereby pressure and temperature sensors automatically correct for changes in Rayleigh scattering. A variable rate flashlamp is used in conjunction with a wavelength defining optical filter (530nm). Photomultiplier tubes count photons resulting from forward scattering at 530nm, calculating scattering coefficients using calibration constants.

Range: 0 to > 1 km^{-1}

Limit of detection: <0.001 km^{-1}; ($1x10^{-6}$ m^{-1}) at 30 sec average

Time/measurement: 20 sec average

Flow Rate: 7 L/min

Data Processing: The 1E-3 externally downloaded light scattering channel was used for the final dataset. Scattering coefficients equal or less than zero and above 0.05 m^{-1} were omitted. In addition, a large proportion of the original data was excluded due a systematic error display of 0.184 m^{-1} for every other measurement for certain periods of the sampling campaign. [Appendix A13]

Instrument: EcoChem PAS 2000CE

Parameters: Particle-bound polycyclic aromatic hydrocarbons (PAHs) on ultrafine particulate matter (ng/m^3)

Principle of operation: Photoionization of particle-bound PAH whereby an excimer lamp exposes the particle to ultraviolet (UV) radiation at a wavelength of such that only the PAH coated aerosols are ionized. The resulting emitted electrons are subsequently removed through the application of an electric field and the remaining positively charged ions are collected on a filter where the charge is measured. The resulting signal is proportional to the concentration of total particle-bound PAH.

Range: 0 to 1000 ng/m^3

Limit of detection: approximately 10 ng/m^3 total particle-bound PAH

Sensitivity: approximately 10 ng/m^3 total particle-bound PAH

Time/Measurement: < 10 sec

Flow Rate: 1 L/min

Data Processing: PAH concentrations less than or equal to 0 ng/m^3 were removed from the final dataset. [Appendix A14]

Instrument: Inficon 2020ppbPro Portable Photoionization Detector

Parameters: Volatile organic compounds (aromatics, unsaturated hydrocarbons, chlorinated hydrocarbons, ketones, alcohols and organic fuels) (ppm)

Principle of operation: The 2020ppbPRO uses photoionization for detecting low level VOCs and is equipped standard with a high performance 10.6 eV lamp.

Range: 10 ppb to 40 ppm isobutylene equivalent

Resolution: 10 ppb

Lower Detection Limit: 10 ppb isobutylene

Accuracy: ± 10% or ± 2 ppm, whichever is greatest

Precision: 1% of calibration (calibrated with 100 ppm isobutylene)

Time/Measurement: less than 3 seconds

Flow Rate: 0.5 L/min

Data Processing: Measurements with concentrations less than or equal to 0 ppm were omitted from the final dataset. Additional data with corresponding instrument error code was removed. No measurements were collected for April 18 and April 19 of the sampling campaign. [Appendix A15]

Dispersion Modeling

In order to further our understanding of the influence of dispersion on changes in air pollution concentration and composition, dispersion modeling was performed using AERMOD View 8.2 (Lakes Environmental, Waterloo Ontario). AERMOD is a bi-Gaussian plume air dispersion model based on the planetary boundary layer theory. The model's concentration estimates are based on a steady-state plume approach and include advanced dispersion algorithms which consider the effects of convection on atmospheric mixing, the advanced handling of human sources, and links winds with surrounding sources (Cimorelli et al., 2005). The dispersion model was run for NO_x in order to establish appropriate analysis of gradient sites and gain insight into the implications of daily meteorological variations on the results.

Source Characterization

A single line area source was defined along the segment of the interstate that passes both north and south gradient sampling locations. The total defined source length was approximately 3070 meters. The source was assumed to be at the centerline of the interstate as defined by a shapefile of the roadways imported into AERMOD using the Universal Transverse Mercator (UTM) coordinate system. Approximate emission rates for the source were defined daily, estimated by using both traffic density and a vehicle emissions generator software (see below). The initial release height was defined as that of the estimated top of the plume height, approximately 3.06 meters, which is 1.7 times the average vehicle height (1.8 meters), typical of the literature (Shewe et al., 2009). Further source dimensions

were defined, with a source width of 37 meters, accounting for the approximate width of the eight-lane interstate.

Traffic Density

Hourly traffic count data for April, 2012, was obtained from the New Mexico Department of Transportation for their I-40 automatic data recorders in Bernalillo County, sites 2035, I00040:155.087-156.740 (Urban Principal Arterial – Interstate, Coors Blvd. (FL4001) Interchange in Albuquerque). An average of the hourly traffic volumes, including both positive and negative direction traffic counts on the interstate, for the relevant dates and sampling periods in April, 2012 were calculated for further source characterization.

Table 4 - Average Hourly Traffic Counts for Gradient Site Sampling Periods *(in thousands of vehicles)*

	15:00	16:00	17:00	18:00	Average
April 18, Wed	11	11	11	8.5	10
April 19, Thu	11	12	11	8.1	10
April 20, Fri	11	12	11	9.0	11
April 21, Sat	8.4	8.3	8.0	6.6	7.8
April 22, Sun	7.1	7.2	6.8	6.4	6.9
April 23, Mon	10	11	10	7.7	9.8
April 24, Tue	11	11	11	8.3	10

Emissions

Vehicle emissions were estimated using emission factors generated using US EPA MOVES (Motor Vehicle Emission Simulator) 2010b. The user is able to specify calendar year, geographical areas, pollutants, vehicle operating characteristics and road types to be modeled (MOVES User Guide, 2009). For the purpose of this analysis, the model was run for the year 2012 in Bernalillo County, New Mexico. All vehicle types were included and ran for urban restricted access only, typical of freeway modeling (MOVES User Guide, 2009). The following output was obtained for carbon monoxide and oxides of nitrogen:

Table 5 - EPA MOVES 2010b Generated Emission Factors

CO (g)	NO_2 (g)	NO (g)	NO_x (g)	Distance (km)
22830888960	362152384	3429951968	3812796816	2375697408

For the purpose of generating a simple dispersion model in AERMOD, NO_x was used as the primary pollutant for dispersion analysis. The MOVES output was used to generate an emission factor in grams/vehicle-kilometer by dividing NO_x with the distance output. This emission rate could then be multiplied by the source length (3.07 km) in order to obtain an emission estimate of 4.93 grams/vehicle. Hourly traffic counts on I-40 were then used to estimate emissions for input into AERMOD for the respective sampling periods. The average hourly vehicle count was multiplied by the emissions estimate to yield an hourly emission rate estimate in grams/hour, followed by subsequent conversion into grams/second for input into AERMOD.

Table 6 - Generated Emissions Rates for NO_x

Date	**Average Traffic Counts**	**NO_x (grams/sec)**
April 18, Wed	10409	856
April 19, Thu	10427	857
April 20, Fri	10673	878
April 21, Sat	7840	644
April 22, Sun	6853	563
April 23, Mon	9803	806
April 24, Tue	10377	853

Receptors

A series of Cartesian receptor grids were created surrounding and overlapping the source for the purpose of creating visually interpretable dispersion maps.

Meteorology

The AERMET meteorological preprocessor was used to generate a base set of 2012 meteorological data. AERMET analyzes meteorological data along with surface reflectivity (albedo), heat transfer (Bowen ratio), and surface roughness parameters from AERSURFACE to define the wind field and other atmospheric characteristics used by AERMOD. The AERMET file was generated using hourly data collected at Albuquerque International Sunport, KABQ (latitude 35.050N, longitude 106.617W); upper air station ID: 23050 and surface station ID: 23050.

Table 7 - Summary of Average Meteorological Parameters for Gradient Site Sampling Periods

	Wind Speed (mph)	Wind Direction (degrees)	Temperature (°F)	Relative Humidity (%)
April 18	11.2	215	78.6	7.8
April 19	13.2	271	70.9	21.7
April 20	7.8	244	73.5	14.3
April 21	4.6	195	81.3	7.3
April 22	7.8	165	82.0	11.3
April 23	< 5.8	64	82.5	12.0
April 24	9.5	327	85.7	9.8

Results

The defined line area source was modeled separately using AERMOD for each of the daily sampling periods using the respective emission rate. A predicted dispersion map for NO_x was generated for each day of the sampling campaign (see Appendix B). Two distinct patterns can be noted from the resultant maps, whereby there are days showing a somewhat symmetric dispersion on either side of the interstate (April 19, 21, 23 and 24) and other days showing a dominant north side dispersion (April 18, 20 and 22).

Figure 7 - Example of AERMOD Generated Symmetric Dispersion Pattern (April 21, 2012) for NO_x (µg/m^3). ***Approximate locations of the North and South sampling areas outlined in black.***

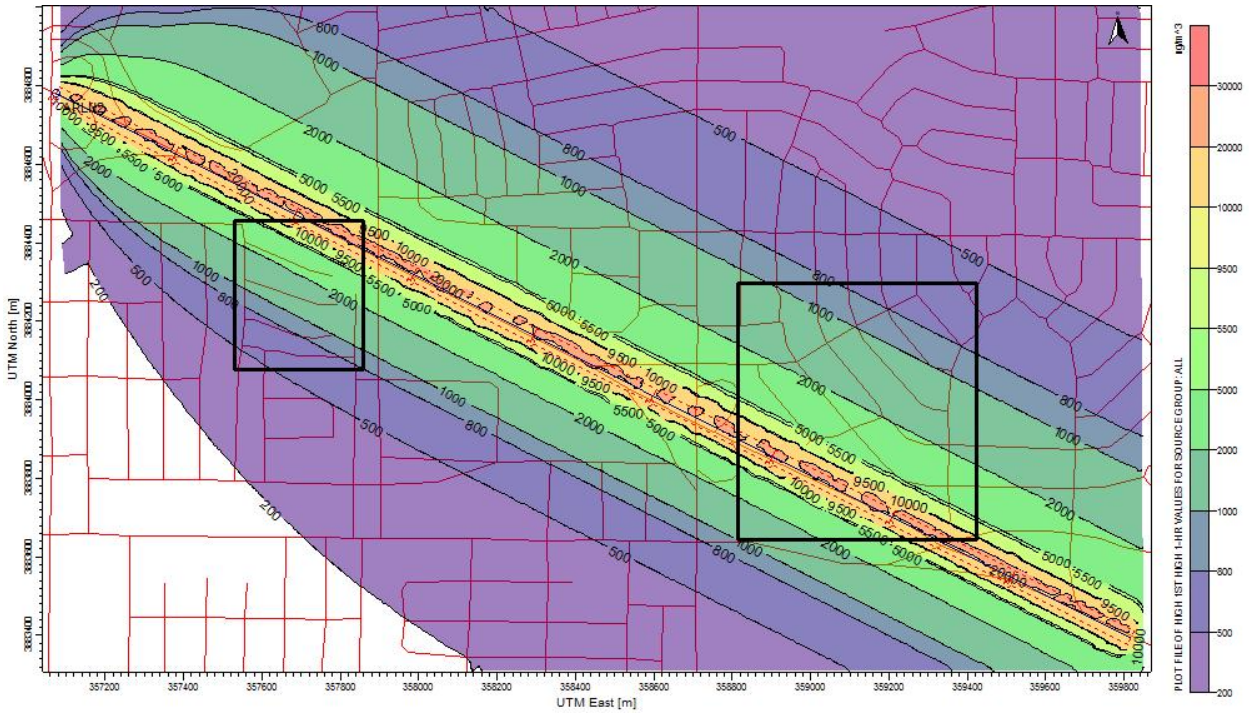

Figure 8 - Example of AERMOD Generated Dominant North Side Dispersion Pattern (April 20, 2012) for NO_x (µg/m^3). ***Approximate locations of the North and South sampling areas outlined in black.***

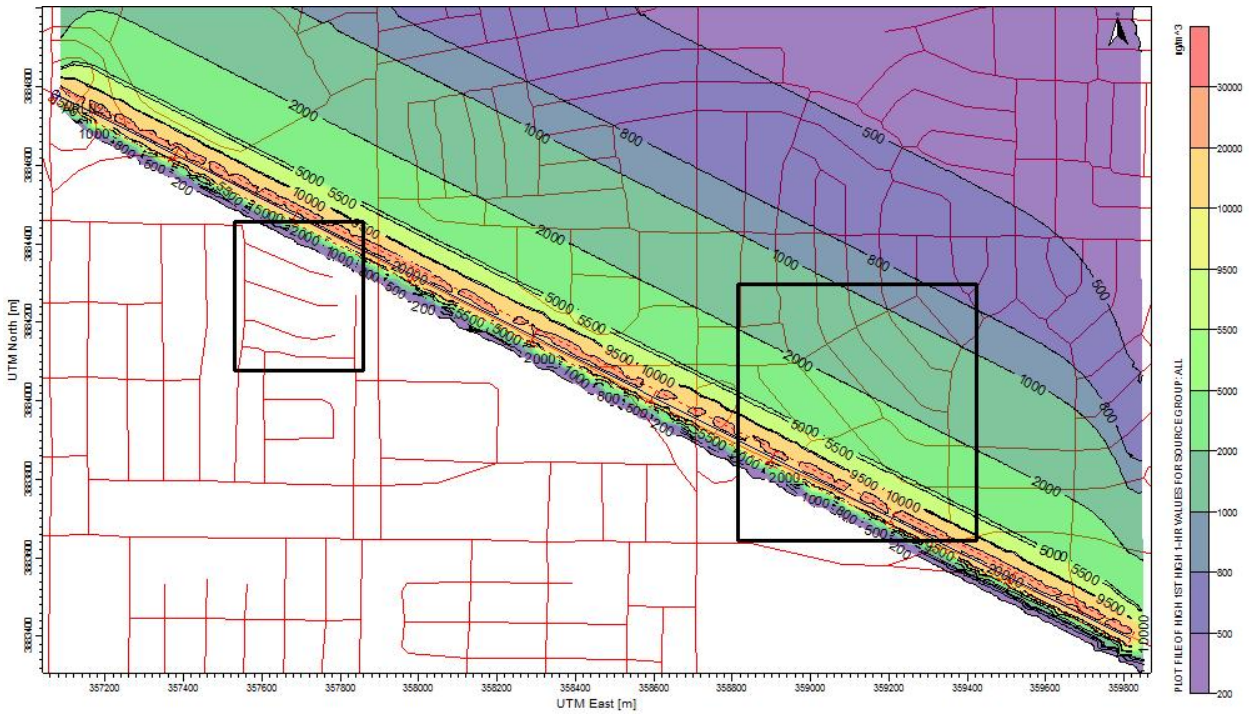

Limitations of this type of dispersion modeling are numerous and include appropriate source characterization, obtaining representative meteorological data, specifying receptors in appropriate areas, and running the model. For instance there is debate over the appropriate use of area versus volume source within the literature for characterizing roadway related emissions (Schewe et al., 2009). Area sources are defined as a near ground level uniform emission line source, whereas a volume source is defined as a source with some initial plume depth with the potential for non-uniform emission characterization. It is typical to consider the road itself as the emission source for dispersion modeling, given the turbulence created by vehicles, temperature changes of the road surface, etc. Despite this, structures such as noise barriers and neighboring buildings may create additional difficulties for characterization by essentially raising the source height. For the purpose of this analysis, however, generated dispersion maps were primarily used qualitatively in order to better understand the potential dispersion behavior at the respective gradient sampling sites. Further considerations as to the most appropriate source characterization should, therefore, be taken into account prior to future quantitative dispersion analyses of the data.

Gradient Site Analysis

Spatially resolved measurements for the tracers of vehicle exhaust were uploaded into ArcMap 10, geographic information system (GIS) software, using the global positioning system (GPS) coordinates logged during the monitoring campaign (NAD 1983 Coordinate System). A shapefile, obtained from the City of Albuquerque, Planning Department, AGIS, defining roadways in Albuquerque was additionally uploaded into ArcMap 10 in order to clearly define the gradient areas for analysis. Initial data manipulation consisted of extracting the gradient data points from those of the much larger mobile monitoring campaign. A select by polygon tool was used in order to visually select all data points on the roadways of interest and exclude the rest of the mobile monitoring data from this specific analysis. A separate north and south gradient were thus established, and respective shapefiles created for each.

Methods for aggregation of mobile measurements were then established through qualitative assessment of the generated AERMOD dispersion maps. Data points were aggregated according to buffer zones parallel to that of the interstate in order to further understand the pollutant behavior with distance from roadway. These zones were determined according to the predicted concentration ranges of the dispersion maps, whereby the width of each buffer zone varied accordingly in order to account for the non-linear behavior of the dispersion process. Similarly, buffer zones were established based on attempting to maintain a somewhat equally distributed number of data points within each zone. Data collected on the south gradient was aggregated into three zones and the north gradient into seven zones. A summary of the total number of mobile measurements aggregated within each zone, along with the distance of the outer edge of the buffer zone (in meters from the interstate) can be seen in Table 8. The geoprocessing buffer tool was used to generate the buffer layers for each of the pre-established linear units from the interstate. A select by location tool was then used to select the data points that were within the buffer layers. A separate layer was thus established for each set of data

contained within a buffer zone. Data points for each zone were then assigned a respective categorical variable for further statistical analysis.

Table 8 - Gradient Analysis Buffer Zones Established Using GIS

Buffer Zone	Distance From Interstate (meters)	Total Number of 10 sec Measurements
S3	< -250 (-350)	398
S2	-100 – -250	587
S1	< -110	58
N1	< 40	148
N2	40 – 80	49
N3	80 – 120	171
N4	120 – 180	264
N5	180 – 260	332
N6	260 – 340	229
N7	> 340 (530)	265

Figure 9 - North Gradient Buffer Zones Defined Using GIS

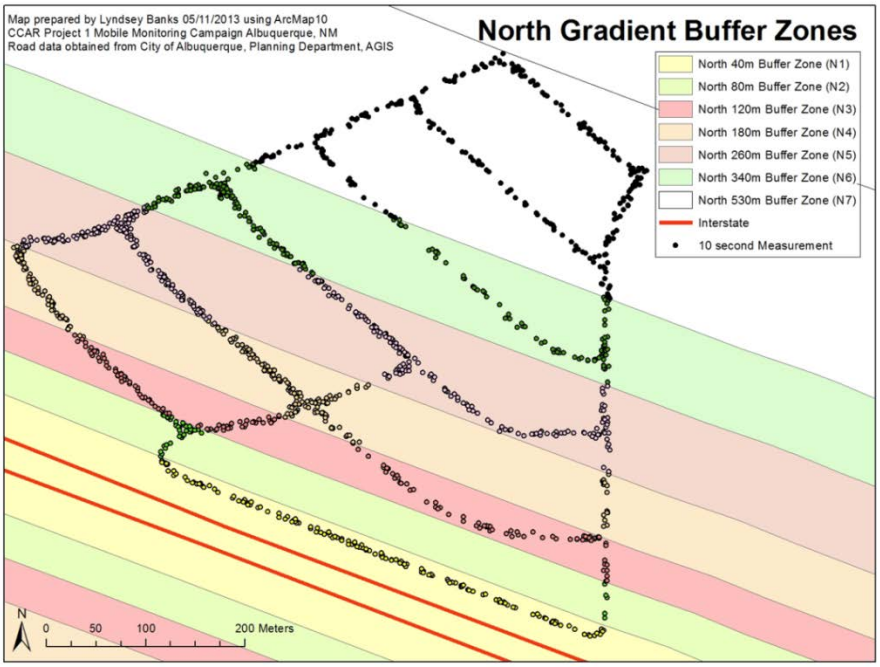

Figure 10 - South Gradient Buffer Zones Defined Using GIS

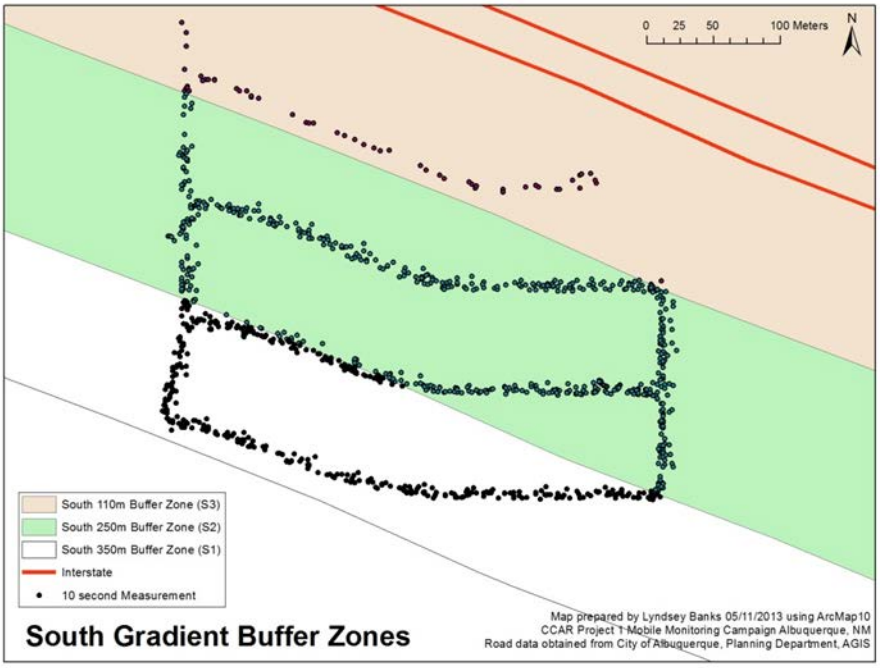

Statistical analysis of the data was performed using STATA 11.2. Time-series plots were generated using this statistical package for the initial qualitative analysis of the data (Appendix A). Further analysis of the gradient sites was dichotomized according to the two notable dispersion patterns, a somewhat symmetric dispersion pattern and a predominantly north dispersion, respectively, as indicated by the AERMOD maps. Generated scatterplots, included in the following discussion section, consist of interconnected points that are indicative of the median pollutant levels across a given buffer region for all sampling days. Vertical bars represent the upper 75^{th} and lower 25^{th} percentiles of the pollutant distributions within the given buffer zone across all days. The vertical line at zero meters is illustrative of the location of the interstate relative to the surrounding buffer locations, and further splits the plots into the respective north and south gradient sites. Vertical dashed lines at both positive and negative 150 meters further define the approximate near-road region.

Results & Discussion

Time Resolved Measurements

Time-resolved plots were generated for each pollutant measured by the instrument platform (Appendix A). Figure 11 shows the complete daily dataset of a single pollutant, separately for NO_x and black carbon, for the entire monitoring campaign, including the data collected on the gradient site locations, as well as on additional monitored roadways. These plots illustrate important aspects of the monitoring campaign, whereby sufficient measurement time-resolution is important for characterization of temporally variable sources (Thoma et al., 2008). The ten second measurements show discernible short time duration spikes in concentration. This variation is attributable to both discrete emission plumes from vehicles, as well as varying wind patterns and the spatial variability in the pollutants measured. The degree of temporal correlation between the measurements of the various instruments is notable. Significant spikes in instrument response are seen to occur across multiple instruments at the same time. This is indicative of discernible pollution events within the dataset. For example, Figure 11, for the entire dataset collected on April 21, 2012, shows two peaks occurring at the same time for a gas (NO_x) and a particle (black carbon) measurement. This is illustrative of extreme events within the data. Further event characterization could be undertaken by attributing specific observations to these discernible peaks through video analysis using the webcam video data collected during the monitoring campaign. For the purpose of this analysis, however, we are most interested in the averages of the data across the gradient locations and these events were maintained within our dataset.

Figure 11 - 10-Second Time-Resolved Measurements of (a) NO_x and (b) Black Carbon on April 21, 2012

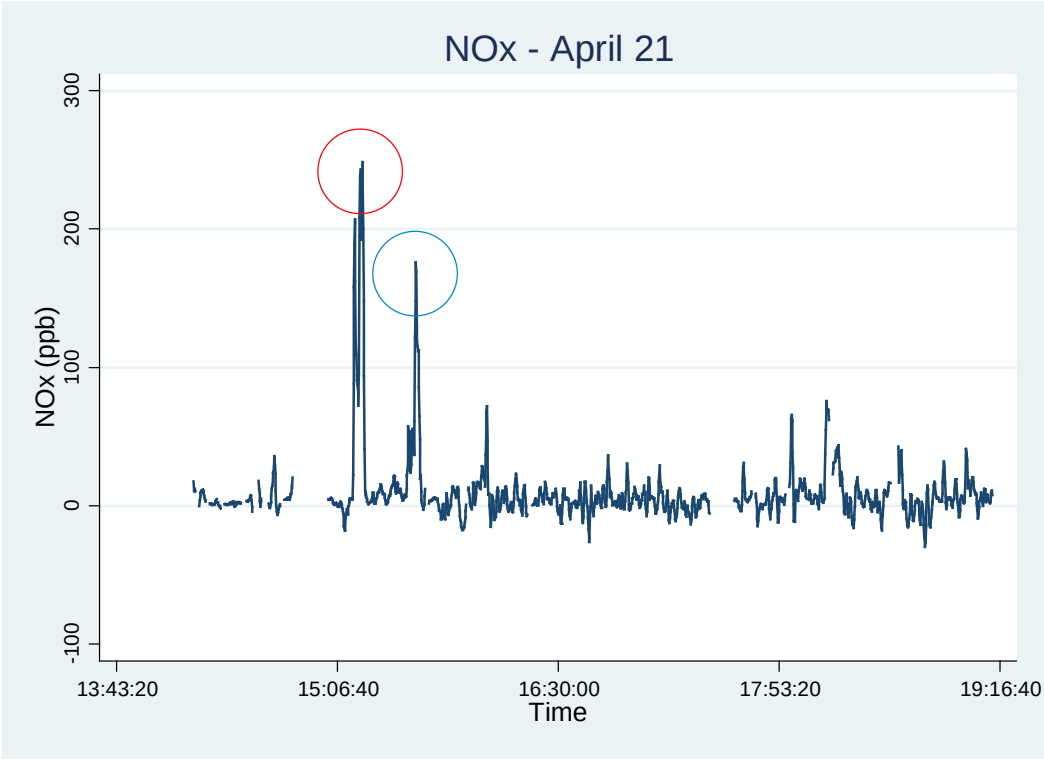

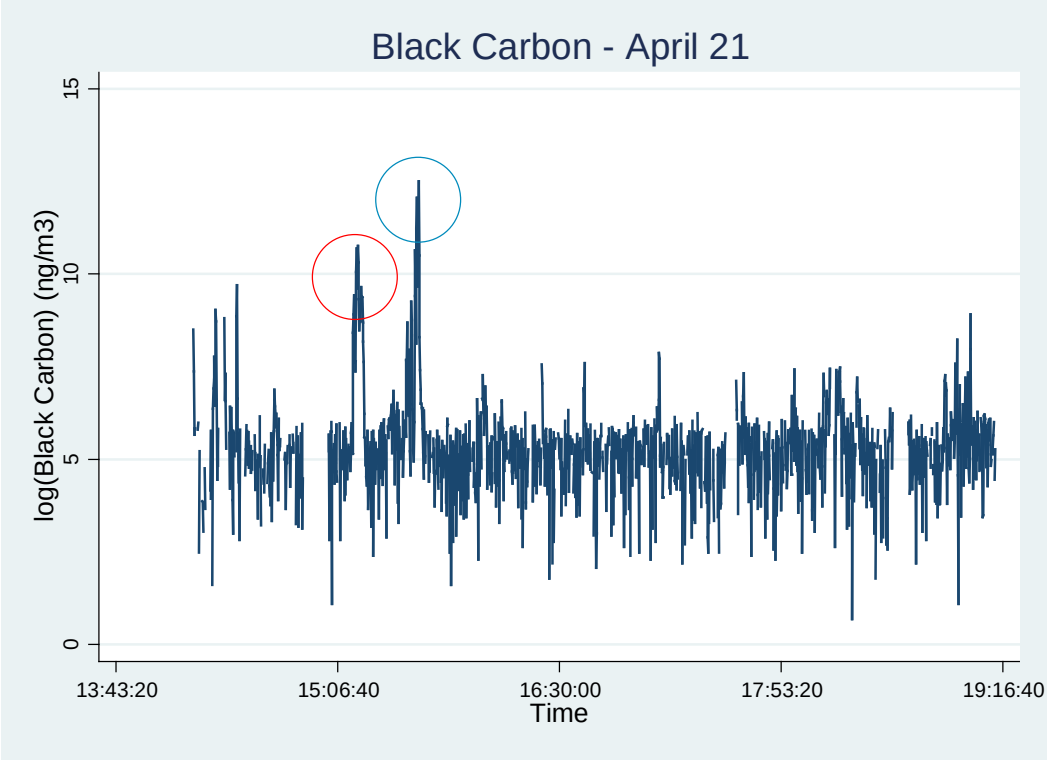

Near-Roadway Measurements

Spatially resolved measurements were obtained for the pollutants of interest across both the south and north gradient site locations. A summary of the entire gradient dataset can be seen below in Table 9.

Concentrations were comparable to those of the nearest EPA Air Quality System (AQS) monitoring site, for which data was obtained from that of the EPA AQS Data Mart for the Del Norte High School site (AQS ID 350010023; Latitude 35.13431, Longitude -106.5852). This location is within approximately 6 km of the south gradient site and approximately 7.3 km of the north gradient site and is located on the northern side of the I-40, northwest with regards to the gradient locations. It is additionally important to note that the Del Norte High School is located approximately 2 km east of Interstate 25, Pan American Freeway. Ozone levels at the AQS site averaged approximately 59 ppb over all sampling periods. Likewise, an average concentration of 6.4 ppb for NO_x and 0 ppb for NO were reported.

Table 9 - Summary of both North and South Gradient Site Data across All Days

				Percentiles		
Variable	**# Obs.**	**Mean**	**St. Dev.**	**25%**	**50%**	**75%**
NO (ppb)	2453	-15.6	11.2	-22.7	-16.3	-9.20
NO_x (ppb)	2451	5.79	12.0	-0.900	4.70	11.0
VOC (ppm)	1945	0.283	0.0460	0.257	0.282	0.309
CO_2 (ppm)	2501	372	5.57	369	372	374
O_3 (ppb)	2226	57.2	11.1	49.9	56.3	63.7
Particle Bound PAH (ng/m^3)	2501	130	105	54.2	104	175
Black Carbon (ng/m^3)	2215	374	546	166	288	7240
Delta Carbon (ng/m^3)	2215	-8.85	181	-114	-7.00	92.0
Particle Light Scattering(m^{-1})	1780	8.79E-6	5.61E-6	5.22E-6	7.31E-6	1.06E-5
P-Trak Ultrafine Counts ($particles/cm^3$)	2287	1380	876	932	1314	1590
GRIMM 0.25 - 1.0µm ($particles/cm^3$)	2385	24200	19300	13400	17600	26100
GRIMM 1.0 - 2.5µm ($particles/cm^3$)	2362	272	197	155	250	348
GRIMM 3.0 - 10µm ($particles/cm^3$)	2362	52.6	65.7	20.0	40.0	65.0
GRIMM Total Particle Counts (0.025 – 0.3µm) ($particles/cm^3$)	2385	6920	6750	4170	6130	9000
GRIMM Particle Mean Diameter (0.025 – 0.3µm) (nm)	2385	52.1	7150	27.0	36.0	48.0

Spatial Variation of Measured Pollutants

Nitrous Oxide Species

Nitric oxide is of particular interest seeing as it is the dominant component of primary NO_x emissions from most on-road sources. In addition, its role in NO_2 formation and ozone chemistry is well known. The notably high concentrations of NO near roadways compared to the lower regional background levels also provide NO with interesting source discrimination capabilities. This is of use in teasing out the aging phenomenon as other markers, such as NO_x, CO and CO_2, all have notably higher background levels (Thoma et al, 2008).

Despite this, the measured concentrations of the nitrous oxide species on the gradient roadways are somewhat difficult to interpret due to the overall baseline offset of the instrument, whereby predominantly negative measurements were obtained (Figure 12 and 13). This is believed to be due to an error in calibration as a result of sample scrubber contamination and in part as a consequence of interference from volatile organic compounds. Additionally, interference from ozone was noted for the 2B Technologies NO unit. The relative change in these pollutants, however, does provide some indication of the dispersion process. The high positive value for both NO_x and NO in the buffer zone nearest the interstate is indicative of the potential for source discrimination, whereby elevated levels of NO are attributable to the traffic on the interstate. Furthermore, the more elevated levels of NO_x on the northern side of the interstate when downwind are consistent with the influence of meteorology on the dispersion process. The EPA AQS site showed an average concentration of 6.4 ppb for NO_x over the gradient sampling periods and an average of 0 ppb for NO. Despite the high frequency of negative values within the dataset – especially for NO, the elevated medians within each buffer zone relative to that of the AQS site indicate that the elevated concentrations of nitrogen oxide species is most likely a result of traffic-related emissions.

Figure 12 – Median Nitrogen Oxides by Dispersion Pattern across All Sampling Days for North and South Gradient Sites

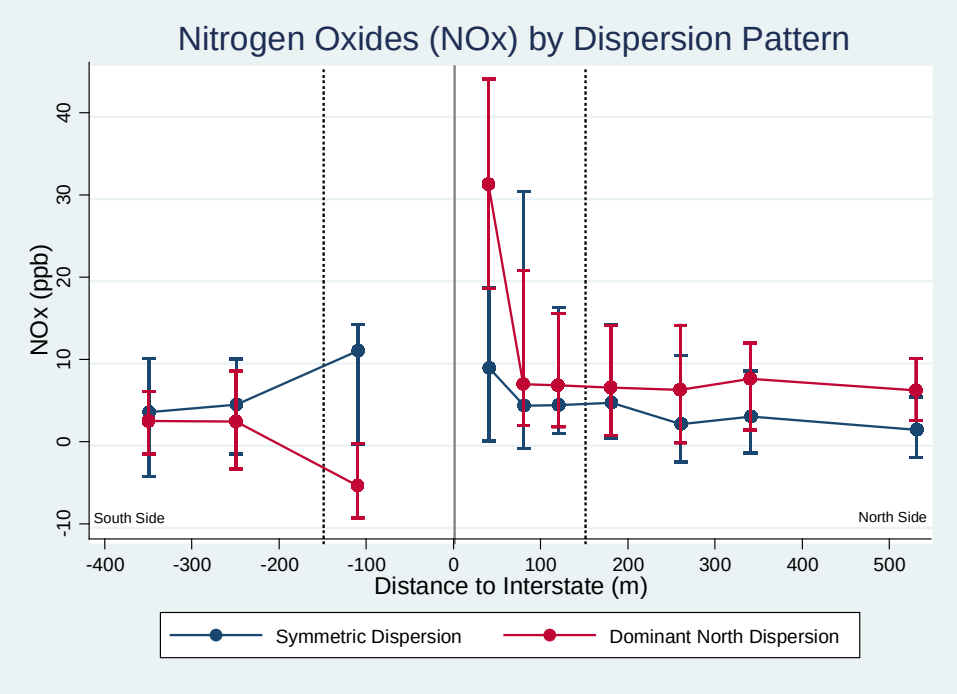

Figure 13 – Median Nitric Oxide by Dispersion Pattern across All Sampling Days for North and South Gradient Sites

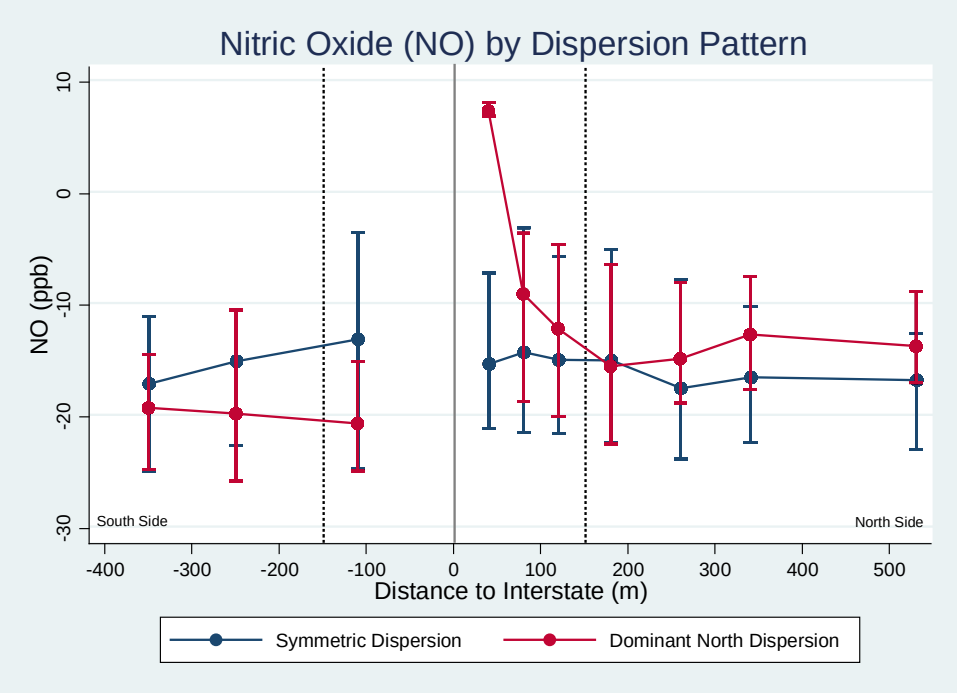

Ozone

Levels of ozone also show a distinctive trend with distance from roadway. Ozone undergoes consumption by NO from the interstate, primarily through the following reaction:

$$NO + O_3 \rightarrow NO_2 + O_2 \quad (1)$$

Our results (Figure 14) are indicative of this phenomenon, whereby we observe depletion of ozone in the near roadway region followed by an increase in ozone concentrations, approaching background levels within approximately 200 to 300 meters from the roadway. Furthermore, the overall elevated levels of ozone for the symmetric dispersion conditions are consistent with the higher overall pollutant levels that would occur through a more stagnant meteorology. The ozone concentration measured at the EPA AQS monitoring site nearest our gradient locations had an average concentration of 59 ppb over all sampling periods, as shown by the horizontal reference line in Figure 14.

Figure 14 – Median Ozone by Dispersion Pattern across All Sampling Days for North and South Gradient Sites

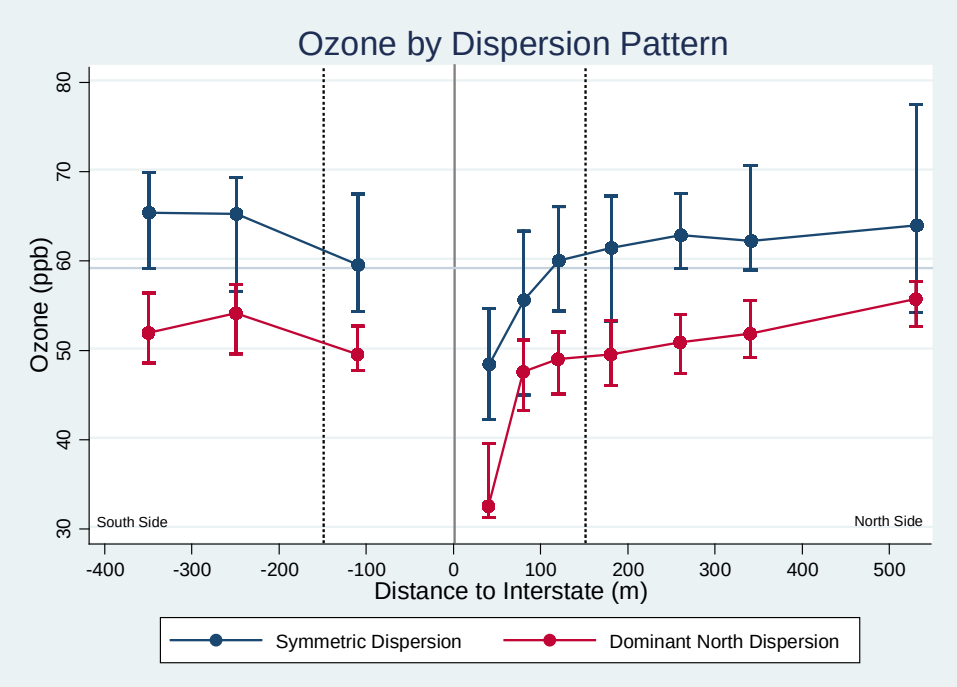

Carbon Dioxide

The concentration of CO_2 was found to be highest closest to the interstate and then observed to gradually fall off as a function of distance, primarily a result of dilution of the CO_2 emitted from vehicles on the roadway (Figure 15). The steepest drop occurs in the downwind near-roadway region, within the first approximate 80 m of the interstate. However, this represents only an approximate 2% change within the level of overall CO_2 concentrations. Massoli et al. (2012), observed an approximate 15-20% drop in the concentration of CO_2 between the 10 m and 200 m regions in the vicinity of a major roadway, in New York City. Factors likely attributing to the difference between our observations and those of Massoli et al. are the typically lower overall pollutant concentrations in Albuquerque compared to New York City as well as the substantially lower volume of traffic per road lane during our monitoring periods. Furthermore, we have no measurements of CO_2 concentrations on the interstate itself, and few measurements within 50 m of the interstate, therefore our measurements would not have captured the regions of highest CO_2 levels within the 50 m closest to the interstate. Durant et al., 2010, also showed a similar behavior of carbon dioxide near-highway, in Massachusetts, with a gradual decrease in the pollutant concentration, returning to background levels within the first 200 to 300 m downwind. Despite this, carbon dioxide is a relatively poor indicator of traffic-related emissions, in this study, due to the relatively high background levels of this pollutant. We also observe little to no difference in the carbon dioxide levels across both types of dispersion, other than within the first 40 m downwind of the roadway, although this is a very small percent measured change.

Figure 15 – Median Carbon Dioxide by Dispersion Pattern across All Sampling Days for North and South Gradient Sites

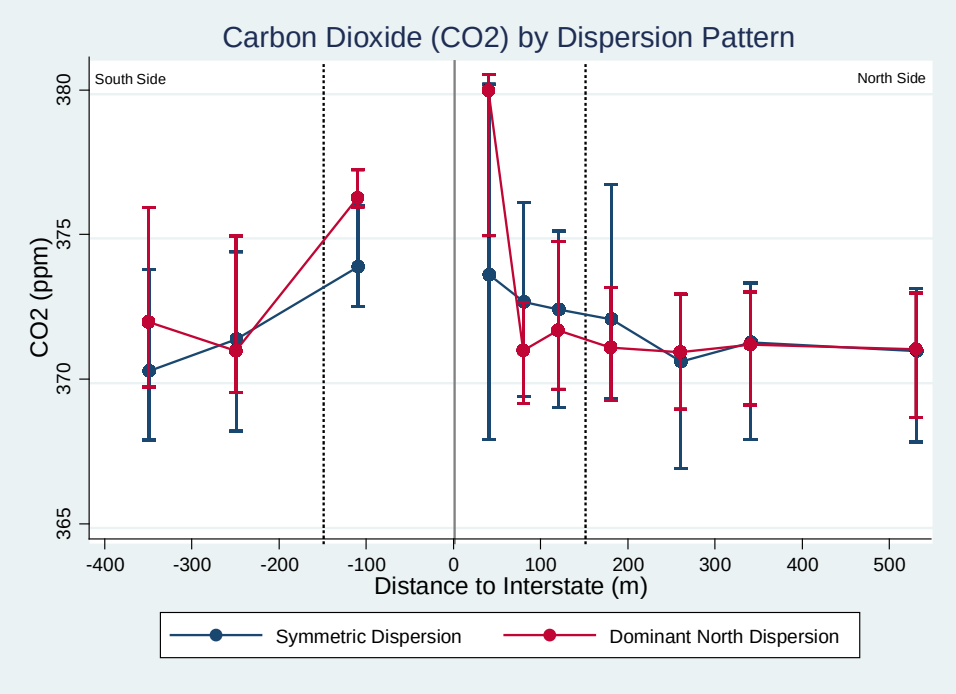

Particulate Matter

In general, spatial patterns differ for ultrafine particles compared to larger particle sizes. The fate of particles greater than approximately 1 µm in diameter is dominated by turbulent diffusion and gravitational settling processes. Brownian motion, on the other hand, plays a significant role in the fate of particles smaller than 0.1 µm (Zhou et al., 2007). Furthermore, coagulation has been reported to govern the overall observed trends of particles with distance from roadway, particularly for particles with diameters less than 0.02 µm (Zhu et al., 2002). The formation of larger particles through coagulation results in a continuous decrease in the total number concentration of particles with increased distance from source. This is further coupled by an increase in particle size, along with the mixing of traffic emissions with the larger modal diameter of the coarser background aerosol. This decrease in concentration occurs more rapidly for smaller particles, whereas the rate is more gradual for the larger particles (Zhou et al, 2007). Similarly, larger particle sizes ($PM_{2.5}$ and PM_{10}) have been shown to have weaker or nonexistent spatial gradients near roadways. Fine particulate matter is primarily a result of exhaust emissions, whereas larger particle sizes are primarily non-exhaust emissions sources, such as resulting from the wear and tear of vehicle parts or from re-suspension of roadway dust (Hagler et al., 2010).

Ultrafine particles, those particles characterized with diameters less than 0.1 µm, show relatively elevated levels close to the roadway. These particles have a relatively short life-time and their spatial variability, consequently, varies according to proximity to the emission source (Pant et al., 2013). As shown in Figure 16, the downwind region shows ultrafine particle counts approximately 1.7 times higher within the first approximate 40 meters of the interstate, than with the upwind region of the dominant north dispersion pattern. This is consistent with Hagler et al. (2010) who have reported ultrafine particles a factor of 1.8 times higher within 20 to 150 meters from the highway than with areas characterized as urban background during downwind conditions. Additionally, Hagler et al. (2010),

reported regional ultrafine particles nearly doubling during low-speed meandering winds relative to crosswind conditions. The near-road levels also remained higher than urban background levels by a factor of 1.2 during these conditions. Although this doubling of ultrafine particles was not observed by our results, the near road ultrafine particle number concentrations remained elevated near-roadway with respect to the relatively flat background levels. It should also be noted that the P-Trak is known to underpredict the total ultrafine particle concentrations as it only detects particles down to 20 nm (Zwack et al., 2011b). Furthermore, a size selective diffusion screen was used for our sampling, whereby only ultrafine particles greater than 0.05 µm in size were measured.

Figure 16 – Median P-Trak Ultrafine Particle Counts by Dispersion Pattern across All Sampling Days for North and South Gradient Sites

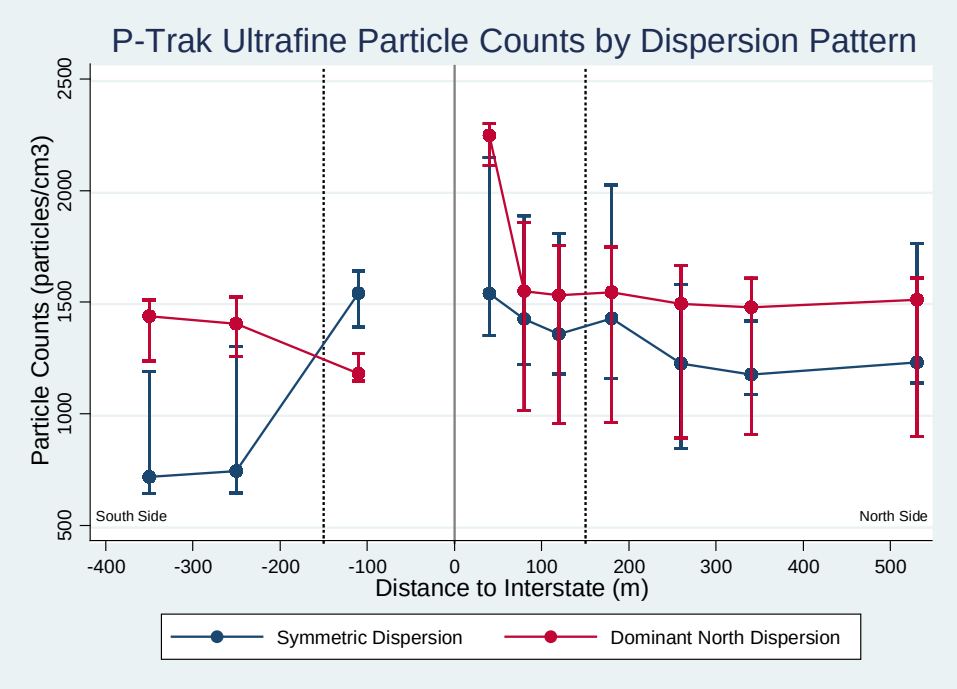

A similar trend is observed between that of the P-Trak ultrafine particle counts and those of the GRIMM Nanocheck total particle counts, particle sizes ranging from 0.025 – 0.3 µm (Figure 17). The downwind near-road ultrafine Nanocheck particle counts were approximately 6.7 times higher than

those of the P-Trak particle counts. This is consistent with what we would expect of the respective particle size ranges measured by these instruments, with the Nanocheck measuring particles of the smaller size range.

Figure 17 – Median GRIMM Nanocheck Total Particle Counts by Dispersion Pattern across All Sampling Days for North and South Gradient Sites

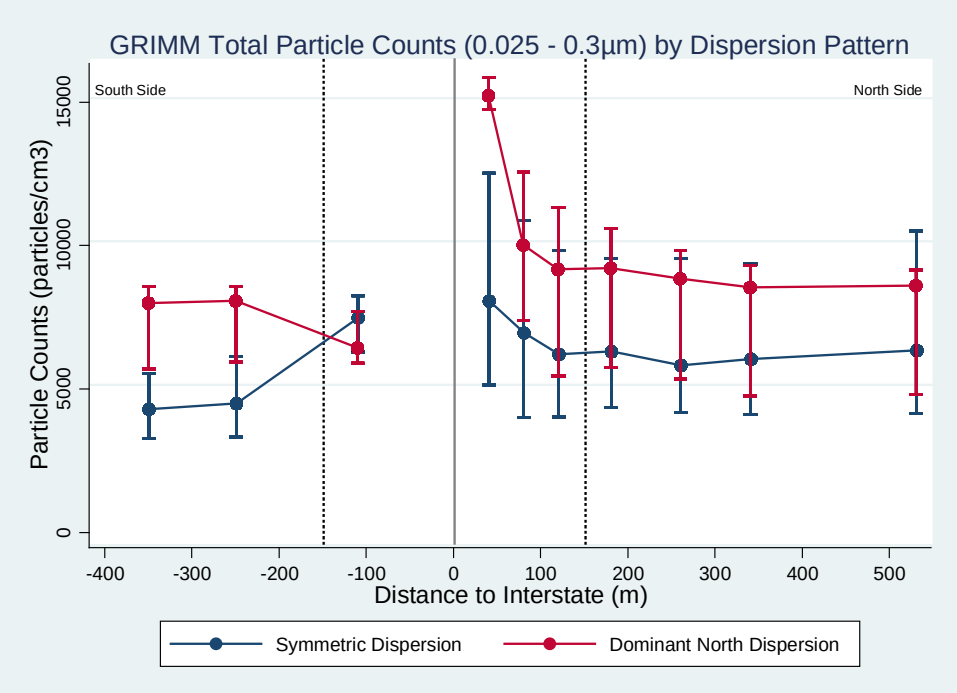

Mean particle diameter is also seen to vary quite largely within a single buffer zone (Figure 18). This is most likely attributable to daily variations in temperature, traffic counts, and additional meteorological impacts on the nucleation of particles. The overall smaller mean particle sizes for the dominant north side dispersion pattern are likely explained by the impact of wind on particle size. Increasing wind speeds can increase the abundance of smaller nucleation mode particles (less than 30 nm) and this can be even greater due to dilution and a lower condensation sink (Vignati et al., 1999). The literature, however, commonly cites an observed increase in particle size with distance from roadway, as a result of mixing of traffic emissions with a coarser background aerosol (Pant et al., 2013). Zhu et al. (2002), similarly, observed variations in the size distribution of ultrafine particles up to 300

meters in distance from a major freeway in Los Angeles. They noted three distinct particles modes (geometric mean diameters of 13, 27 and 65 nm) within the first 30 meters downwind of the freeway, and observed the mode for the smallest particle sizes shifting to larger geometric mean diameters with downwind distance from the freeway. Despite the literature, no strong gradient is notable of particle diameter with distance from interstate for our measurements. This is possibly due to our inability to capture these changes in particle size as we were unable to distinguish between these ultrafine particle modes. Furthermore, the various types of instruments used throughout these studies could substantiate this difference in results.

Figure 18 – Median GRIMM Nanocheck Mean Particle Diameter by Dispersion Pattern across All Sampling Days for North and South Gradient Sites

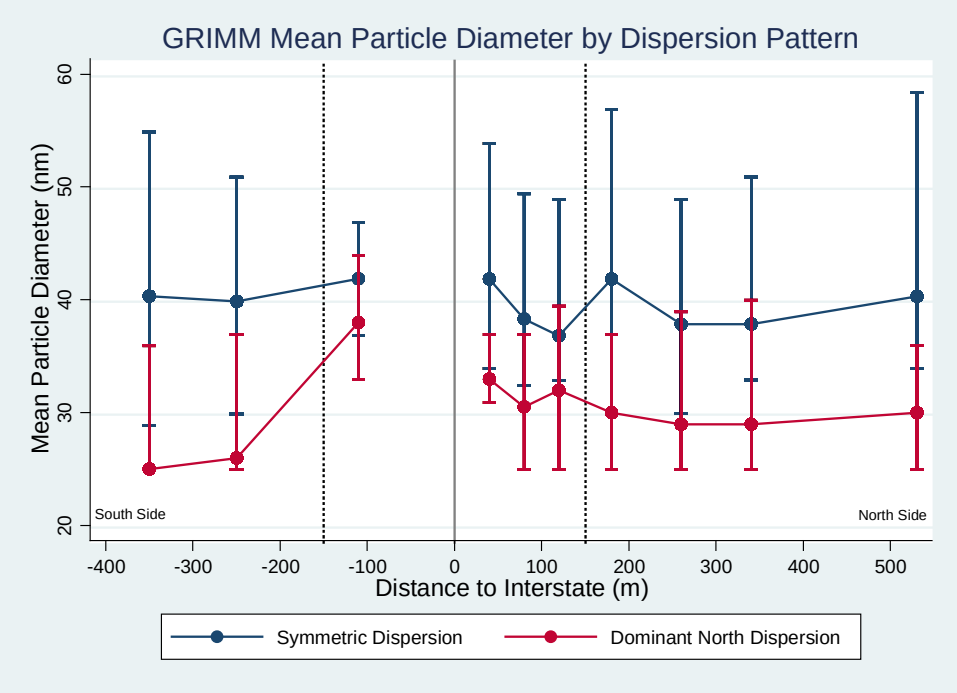

The particle number concentrations for particles greater than 50 nm (0.05 µm) are consistently reported throughout the literature to remain relatively constant with distance from highway (Durant et al., 2010, Zhu et al., 2006, Hu et al., 2009). Our results were somewhat consistent with this trend. For the north side, both particle number concentrations for the 1.0 – 2.5 µm (Figure 20) and 3.0 – 10 µm

(Figure 21) sized particles show a relatively constant count with increasing distance from I-40. Relative to symmetric dispersion conditions, the north side dominant dispersion pattern shows overall lower particle counts within the first 40 m of I-40 for the 1.0 – 2.5 μm size, as well as consistently lower particle counts for the larger 3.0 – 10 μm sized particles. This is potentially a result of the greater turbulence associated with this type of dispersion pattern, whereby there is the greater potential for coagulation and larger particle settling. Furthermore, it is important to note that we are, by definition, comparing different days for the two dispersion patterns. It is, therefore, possible that the background air pollution was higher on the more stagnant days, under the symmetric dispersion pattern, and subsequently, the higher levels may be a result of fluctuations in regional meteorology rather than due to the roadway itself.

The smallest GRIMM particles (0.25 – 1.0 μm), similarly, show overall lower particle counts for the dominant north side dispersion pattern than for the more symmetric dispersion (Figure 19). There is also approximately a 30% decrease in particle count with distance from roadway, returning to the flat background profile within the first 150 m of the interstate. These results are additionally in agreement with Zhu et al. (2002a), whereby they observed elevated particulate mass concentrations immediately downwind of the freeway with subsequent gradual decrease with increasing distance.

Figure 19 - Median GRIMM Particle Counts (0.25 – 1.0 µm) by Dispersion Pattern across All Sampling Days for North and South Gradient Sites

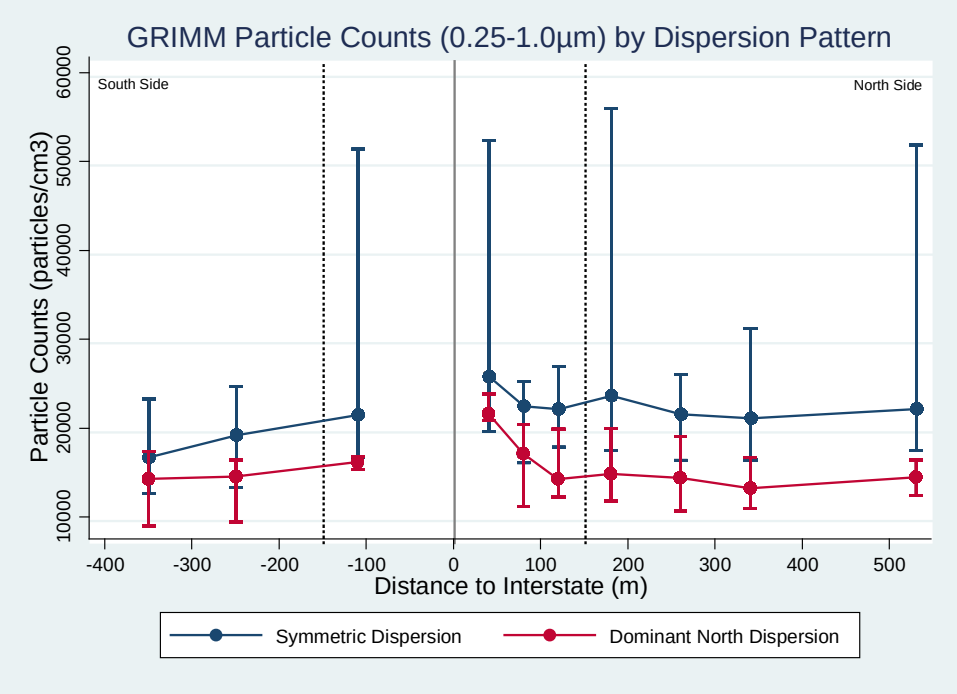

Figure 20 - Median GRIMM Particle Counts (1.0 – 2.5 µm) by Dispersion Pattern across All Sampling Days for North and South Gradient Sites

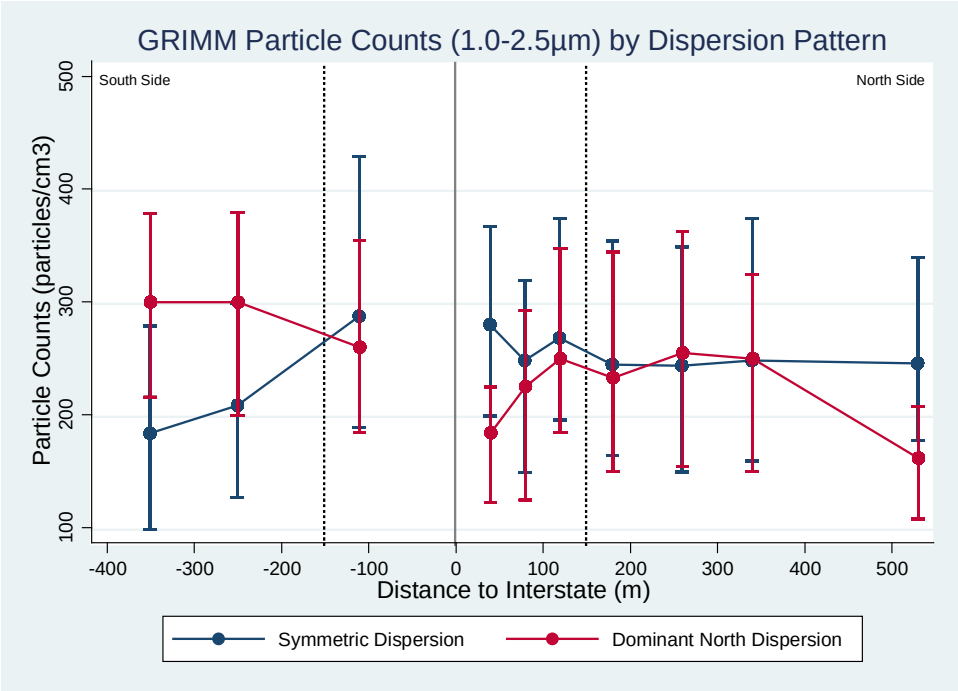

Figure 21 – Median GRIMM Particle Counts (3.0 - 10 µm) by Dispersion Pattern across All Sampling Days for North and South Gradient Sites

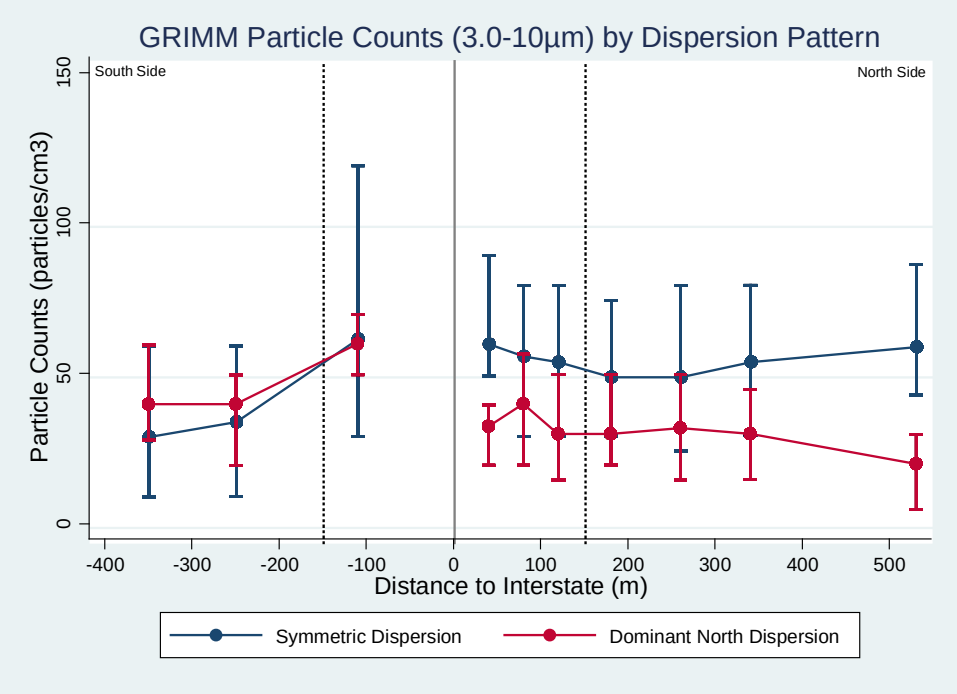

Particle Light Scattering

The values of extinction coefficients vary with particle size distribution, particle composition, and relative humidity (Chow et al., 2006). Furthermore, light scattering is a function of the wavelength of incident light, whereby particles with comparable diameters, fine particulate ($PM_{2.5}$) in this case, scatter light more efficiently, resulting in a higher extinction coefficient. (Chow et al., 2006). The extinction coefficients are, subsequently, somewhat comparable to the measured particles less than 2.5 µm by the GRIMM Aerosol Spectrometer. As motor vehicles are a well-known source of $PM_{2.5}$, we would expect elevated levels of $PM_{2.5}$ near the roadway (Pant et al., 2013). Hitchens et al., 2000, have reported a decrease of approximately 50% in $PM_{2.5}$ within 100 – 150 meters of the roadway. This trend is evidenced by the decrease in particle light scattering extinction coefficients within the near-road region seen in Figure 22. We additionally observe higher extinction coefficients for the symmetric dispersion than for the dominant north dispersion pattern, a similar trend to that of the GRIMM particle counts.

Figure 22- Median Particle Light Scattering Extinction Coefficient by Dispersion Pattern across All Sampling Days for North and South Gradient Sites

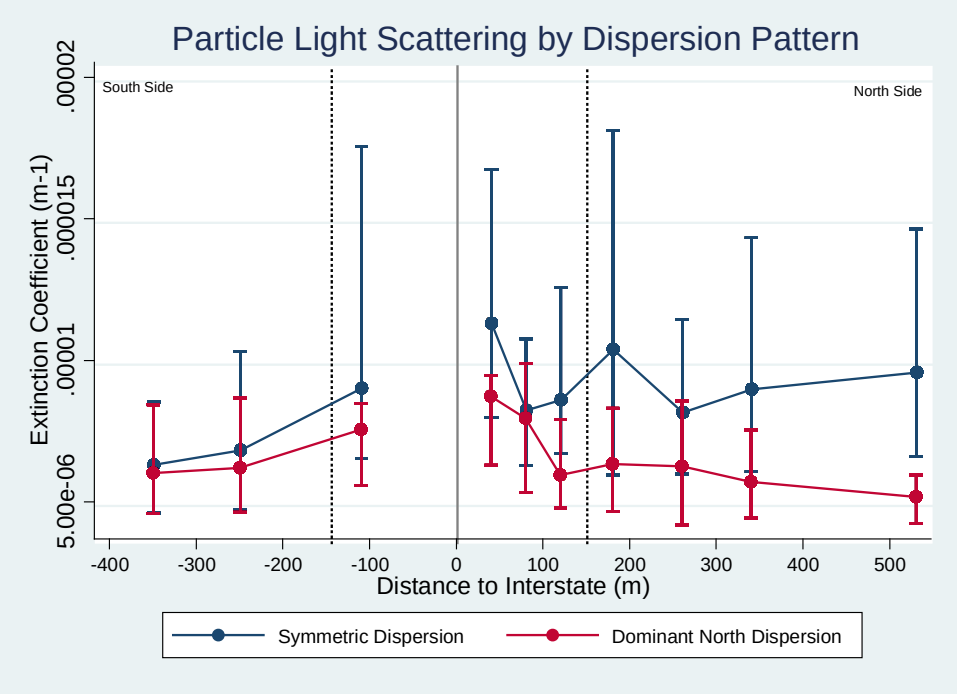

Black Carbon

The overall black carbon trends observed in Figure 23 are consistent with the expected dispersion processes attributable to an on roadway emissions source. The dominant north dispersion clearly shows the elevated levels of black carbon downwind of the interstate relative to the upwind location, as well as the notable decrease in concentration with downwind distance of the roadway of the literature (Hagler et al., 2010). The symmetric dispersion also shows overall lower concentrations on the north gradient location than that of the dominant north dispersion, and somewhat similar background levels on either side of the interstate. A study conducted in Raleigh, North Carolina, by Baldauf et al. (2008a) observed a similar trend with elevated levels noted at a downwind stationary location within 20 meters of the major roadway. The median black carbon measurement at this site was 1014 ng/m^3 and the median concentration measured at their 200 meter location was 824 ng/m^3. The overall lower concentrations observed in Albuquerque are likely attributable to a variety of factors, such

as differences in vehicle volume and fleet composition, as well as different existing background concentrations and the potential influence of the noise barriers. The similarity between our near road measurements within the downwind buffer zone at 40 meters to their median value at 20 meters, however, further substantiates that the elevated pollutant concentrations are a result of traffic-related activity.

Figure 23 – Median Black Carbon by Dispersion Pattern across All Sampling Days for North and South Gradient Sites

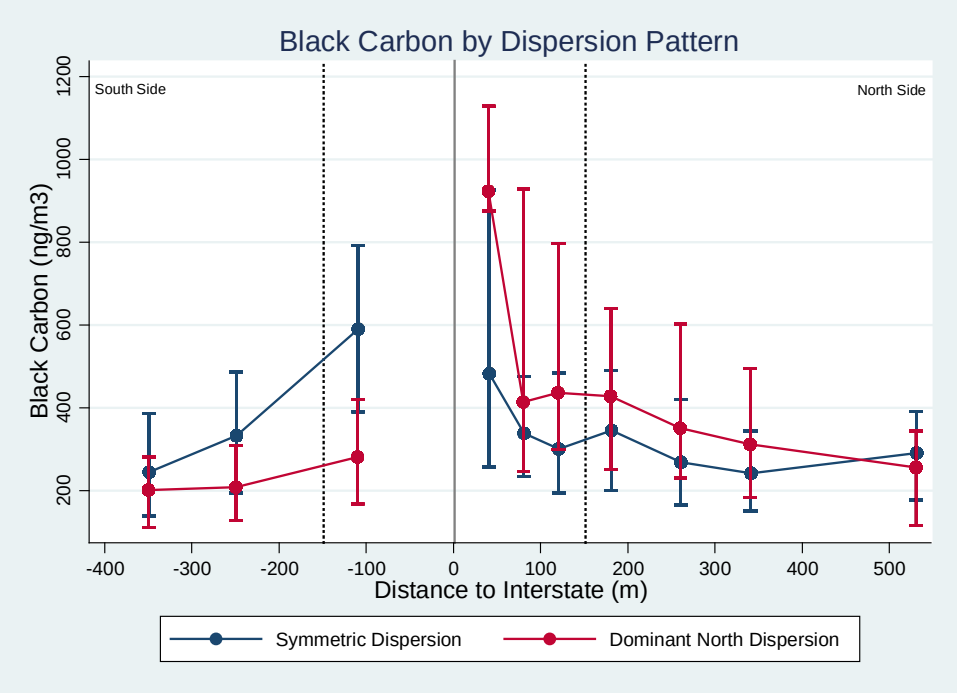

Delta Carbon

Delta carbon has previously been shown to be a tracer of wood combustion and has been used in source apportionment, whereby it plays an important role in separating traffic emissions from those of wood emissions (Wang et al., 2012). Delta carbon was calculated by taking the difference between the UVPM and black carbon measurements. The north dominant dispersion shows slightly higher UVPM relative to black carbon concentrations, whereas the opposite is true for the more symmetric dispersion pattern (Figure 24). These negative delta carbon values are believed to be a result of improper flow rate calibration of the ultraviolet channel. However, both gradients show large variations in delta carbon concentrations within a buffer zone and no trend in delta carbon with distance from roadway is observed. This observation is unsurprising in that delta carbon is typically an indicator for wood combustion and is not an important component of roadway emissions.

Figure 24 – Delta Carbon by Dispersion Pattern across All Sampling Days for North and South Gradient Sites

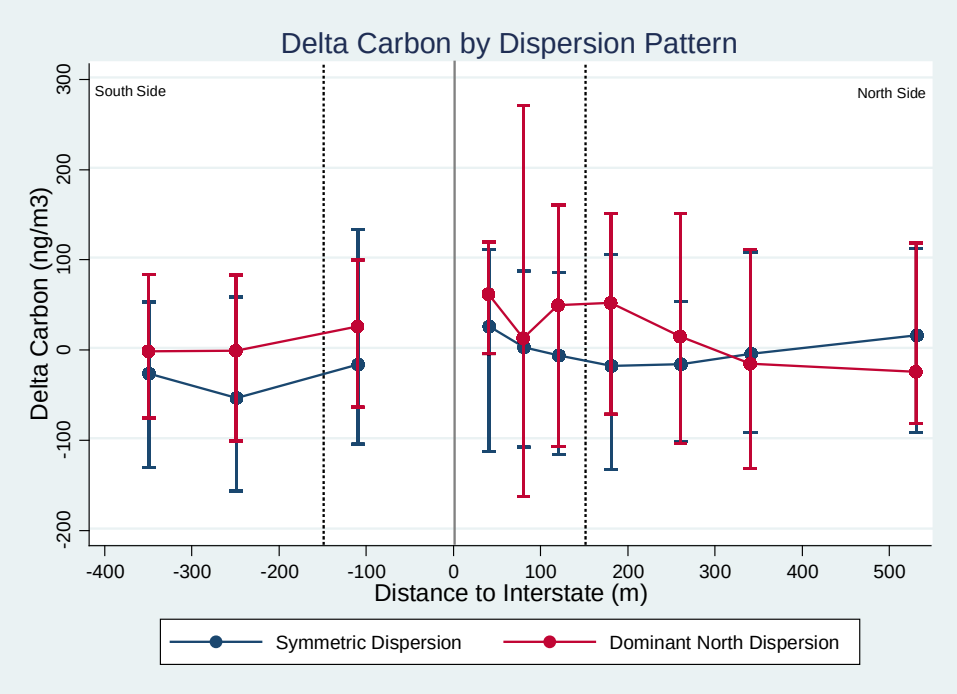

Particle-Bound Polycyclic Aromatic Hydrocarbons

Polycyclic aromatic hydrocarbons are formed from incomplete combustion of carbon-containing fuels and can originate from industrial emissions, solid waste incineration and vehicular emissions. PAHs cover a wide range of volatilities, and those compounds with low vapor pressure condense and absorb immediately onto particles after they are released from combustion. The dust that is deposited on either side of the road frequently contains high levels of PAHs generated from vehicular activities (Marr et al., 2006). For this reason, we expect elevated PAH levels near the roadway, with concentrations changing due to both dilution and gas-particle partitioning as we increase with distance from roadway.

We observed higher concentrations of PAHs in the buffer zone nearest the roadway on the north gradient site for the symmetric dispersion, followed by the steep fall-off behavior (Figure 25). This is consistent with previous reports in the literature, whereby the heavier PAH species are elevated close to the roadway, but decline to upwind levels by 65 m from the roadway (Clements et al., 2009). Higher downwind than upwind concentrations of the lighter PAH species have also been observed in the literature, indicative that traffic-related emissions are the primary source of PAHs in the vicinity of a major roadway (Hu et al., 2009; Clements et al., 2009). The dominant north dispersion profile downwind of the interstate is not consistent with the literature in that observed PAH levels were modestly reduced close to the roadway and increased to their maximum levels at a distance of approximately 120 m. This behavior is potentially explained by the gas-particle partitioning of the PAH compounds, whereby the semi-volatile nature of the PAHs enables them to repartition between the gaseous and particulate forms (Marr et al., 2006). We appear to potentially be observing PAHs in the initial gas phase within the near-road downwind region, followed by the subsequent PAH coating of particles. Alternatively, given that the changes we observe in median PAH concentrations are small relative to the range of measurements within each buffer zone, our observations may also be consistent with an insignificant contribution from the roadway to particle-bound PAH concentrations under the dominant north dispersion pattern.

Figure 25 – Polycyclic Aromatic Hydrocarbons by Dispersion Pattern across All Sampling Days for North and South Gradient Sites

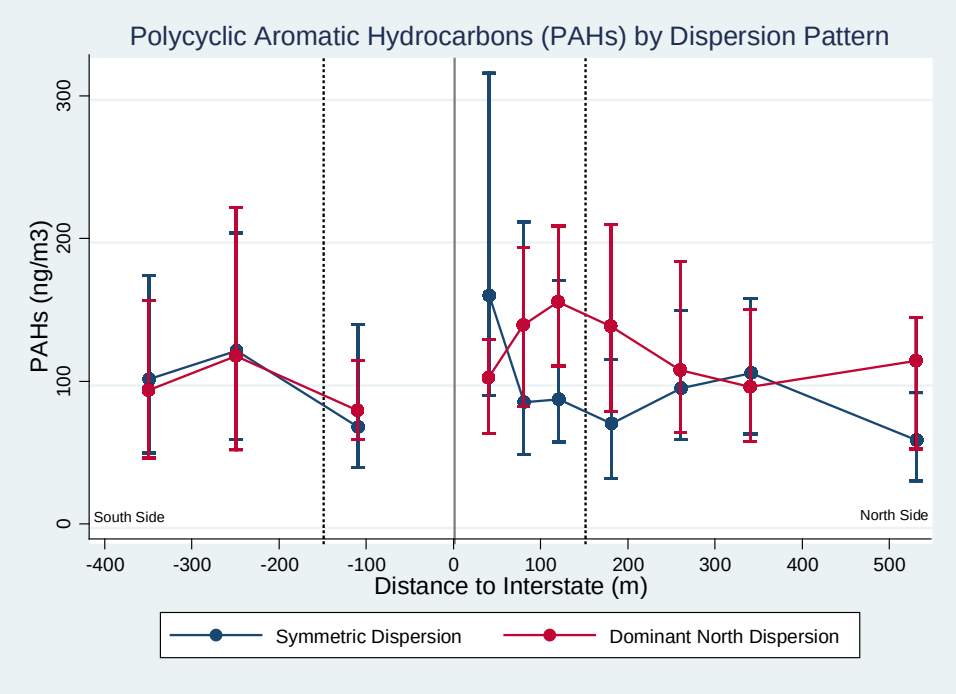

Volatile Organic Compounds

Olsen et al. (2009) and Wang et al. (2008) have reported that VOC species generally show a slowly decreasing trend with horizontal distance from roadway. This pattern is observed downwind of I-40, whereby a fall off is noted within the first approximate 100 m of the roadway (Figure 26). Due to the relatively large overlapping distributions within each buffer zone for the two dispersion types, however, there is little notable evidence of a significant contribution from the roadway to VOCs. The photoionization detector that we use provides a single integrated measure of total VOC concentration. However, it does not capture changes that occur in the composition of the VOC mixture that might be occurring as reactive compounds (e.g. alkenes) undergo chemical reaction to form oxidized VOCs.

Figure 26 – Median Volatile Organic Compounds by Dispersion Pattern across All Sampling Days for North and South Gradient Sites

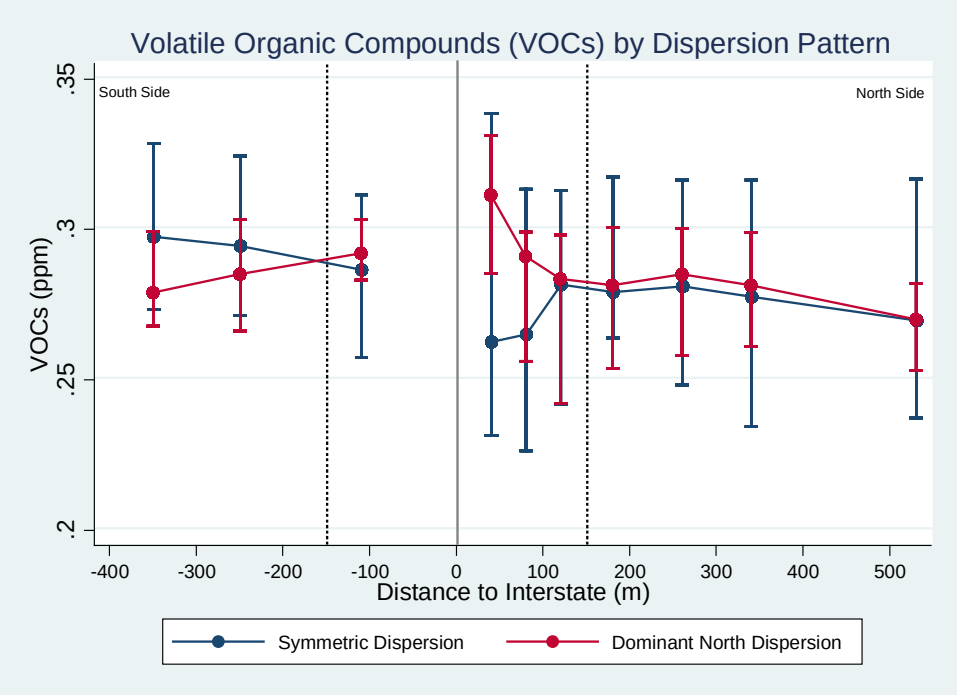

Conclusion

The multi-pollutant and highly time-resolved measurements of the mobile monitoring campaign allowed for the evaluation of the variation of the complex air pollution mixture in the vicinity of a major roadway. Overall, there was an indication of elevated vehicle-emitted pollutants within the first approximate 100 meters of the roadway. Our results were additionally indicative of the decline of several pollutants with distance from roadway, consistent with that of the literature, whereby pollutant levels return to background concentrations within several hundred meters of the interstate. Furthermore, when dispersion modeling software predicted a downwind gradient site, notable differences were observed between that of the downwind pollutant measurements versus those of the more well-mixed symmetric dispersion pattern. This is consistent with the impact of meteorological factors on near-roadway pollutant gradients.

Further analysis of the data could involve correcting for background pollutant levels, identifying event peaks within the dataset through video analysis, and an additional multivariate statistical approach coupled with the use of dispersion modeling software to predict pollutant concentrations across the gradient sites. The use of AERMOD to predict the concentrations of one of the 'non-reactive' pollutant species by placing receptors at the specific geographic coordinates of the measurements collected throughout the sampling campaign would be an obvious next step. The simple nature of the 'non-reactive' species would allow for the most appropriate assessment as to the bi-Gaussian model's predictive capabilities for the Albuquerque gradient locations and its further applicability to quantitative analysis of the experimental data. Considerations as to the most appropriate source characterization (line area versus volume source) and the ability to account for the potential influence of the noise barriers on the dispersion process should be further assessed prior to this type of model application.

Overall, this preliminary analysis of Albuquerque provides us with a better understanding of how to characterize the respective pollutant gradients and further enables us to develop an analysis method which may be applicable to future studies in other cities.

References

Baldauf, R., Thoma, E., Hays, M., Shoes, R., Kinsey, J., Gullet, B., Kimbrough, S., Isakov, V., Long, T., Khylstov, A., Weinstein, J., Chen, F.L, Seila, R., Olson, D., Gilmour, I., Cho, S.H., Watkins, N., Rowley, P., Bang, J., *Traffic and meteorological impacts on near-road air quality: summary of methods and trends from the Raleigh near-road study,* 2008a. J. Air & Waste Manage. Assoc., 58:865-878

Baldauf, R., Thoma, E., Khystov, A., Isakov, V., Bowker,G., Long, T., Snow, R., *Impacts of noise barriers on near-road air quality*, 2008b. Atmos. Environ., 42:7502-7507

Beer, J.M., Jacques, M.T., Farmayan, W., Taylor, B.R., *Fuel-nitrogen conversion in staged combustion of a high nitrogen petroleum fuel*, 1981. Eighteenth Symposium on Combustion, 18(1):101-110

Chow, J.C., Watson, J.G., Park, K., Lowenthal, D.L., Robinson, N.F., Magliano, K.A., *Comparison of particle light scattering and fine particulate matter mass in central California*, 2006. J. Air & Waste Manage. Assoc., 56:398-410

Cimorelli, A.J., Perry, S.G., Venkatram, A., Weil, J.C., Paine, R.J., Wilson, R.B., Lee, R.F., Peters, W.D., Brode, R.W., *AERMOD: A dispersion model for industrial source applications. Part 1: General model formulation and boundary layer characterization*, 2005. J. Appl. Metero., 44:682-693

Clements, A.L., Yuling, J. Denbleyker, A., McDonald-Buller, E., Fraser, M.P., Allen, D.T., et al., *Air pollutant concentrations near three Texas roadways, part II: Chemical characterization and transformation of pollutants*, 2009. Atmos. Environ., 43:4523-4534

Durant, J.L., Ash, C.A., Wood, E.C., Herndon, S.C., Jayne, J.T., Knighton, W.B., Canagaratna, M.R., Trull, J.B., Brugge, D., Zamore, W., Kolb, C.E., *Short-term variation in near-highway air pollutant gradients on a winter morning*, 2010. Atmos. Chem. Phys., 10:8341-8352

Dockery, D.W., Peter, H.S., *Cardiovascular risks from fine particulate air pollution*, 2007. N. Eng. J. Med. 356(5): 511-513

Hagler, G.S.W., Thoma, E.D., Baldauf, R.W., *High resolution mobile monitoring of carbon monoxide and ultrafine particle cocentrations in a near-road environment*, 2010. J. Air & Waste Manage. Assoc., 60:328-336

Hagler, G.S.W., Baldauf, R.W., Thoma, E.D., Long, T.R., Snow, R.F., Kinsey, J.S., Oudejans, L., Gullett, B.K., *Ultrafine particles near a major roadway in Raleigh, North Carolina: Downwind attenuation and correlation with traffic-related pollutants,* 2009, Atmos. Environ., 43:1229-1234.

HEI Panel, *Traffic-related air pollution: a critical review of the literature on emissions, exposure, and health effects*, Health Effects Institute, 2010

Hitchens, J., Marawska, L., Wol, R., Gilbert, D., *Concentrations of submicrometre particles from vehicle emissions near a major roadway*, 2000. Atmos. Environ., 34:51-59

Hu, S., Fruin, S., Kozawa, K., Mara, S., Paulson, S.E., Winer, A.M., *A wide are of air pollutant impact downwind of a freeway during pre-sunrise hours*, 2009. Atmos. Environ., 43:2541-2549

Finn, D., Clawson, K.L., Carter, R.G., Rich, J.D., Eckman, R.M., Perry, S.G., Isakov, V., Heist, D.K., *Tracer studies to characterize the effects of roadside noise barriers on near-road pollutant dispersion under varying atmospheric stability conditions,* 2010. Atmos. Environ., 44:204-214

Marr, L.C., Dzepina, K., Jimenez, J.L., Reisen, F., Bethel, H.L., Arey, J., Gaffney, J.S., Marley, N.A., Molina, L.T., Molina, M.J., *Sources and transformations of particle-bout polycyclic aromatic hydrocarbons in Mexico City*, 2006. Atmos. Chem. Phys., 6:1733-1745

Massoli, P., Fortner, E.C., Canagaratna, M.R., Williams, L.R., Zhang, Q., Sun, Y., Schwab, J.J., Trimbom, A., Onsach, T.B., Demerjian, K.L., Kolb, C.E., Worsnop, D.R., Jayne, J.T., *Pollution gradients and chemical characterization of particulate matter from vehicular traffic near major roadways: results from the 2009 Queens College air quality study in NYC*, 2012. Aerosol Science and Technology, 46(11):1201-1218

MOVES User Guide 2009, United States Environmental Protection Agency, EAP-420-B-09-008, April, 2009

Olson, D.A., Hammond, D.M., Seila, R.L., Burke, J.M., Norris, G.A., *Spatial gradients and source apportionment of volatile organic compounds near roadways,* 2009. Atmos. Envrion., 43:5647-5653

Pant, P., Harrison, R.M., *Estimation of the contribution of road traffic emissions to particulate matter concentrations from field measurements: a review*, 2013. Atmos. Environ., 77:78-97

Peltier, R.E., Cromar, K.R., Ma, Y., Fan, Z., Lippmann, H*., Spaital and seasonal distribution of aerosol chemical components in New York City: (2) road dust and other tracers of traffic-generated air pollution*, 2011. Jour. Of Exp. Sci. and Environ. Epidem., 21; 484-494

Peters, A., von Klot, S., Heier, M., Trentinaglia, I., Hormann, A., Wichmann, H.E., Lowel, H., *Exposure to traffic and the onset of myocardial infarction*, 2004. N. Eng. J. Med., 351(17): 1721-1730

Pirjola, L., Passonen, P., Pfeiffer, D., Hussein, T., Hameri, K., Koskentalo, T., Virtanen, A., Ronkko, T., Keskinen, J., Pakkanen, T.A., Hillamo, R.E., *Dispersion of particles and trace gases nearby city highway: mobile laboratory measurements in Finland*, 2005. Atmos. Environ. 40: 867-879

Thoma, E.D., Shores, R.C., Isakov, V., Baldauf, R.W., *Characterization of near-road pollutant gradients using path-integrated optical remote sensing,* 2008. J. Air & Waste Manage. Assoc., 58:7, 879-890

Schewe, G.J., Smith, P.J., *Sensitivity of AERMOD in modeling fugitive dust emission source*. Trinity Consultants, October, 2009. Paper No. 31.

U.S. Department of Transportation, Federal Highway Administration. "S*ummary of Noise Barriers Constructed by December 31, 2010".* 9 June 2013. http://fhwainter.fhwa.dot.gov/environment/noise/noise_barriers/inventory/summary/sstates711.cfm

Vignati, E., Berkowicz, R., Palmgren, F., Lyck, E., Hummehshoj, P., *Transformation of size distributions of emitted particles in streets,* 1999. Science of the Total Environment, 1(3):37-49.

Wang, Y., Hopke, P.K., Rattigan, O.V., Chalupa, D.C., Utell, M.J., *Multiple-year black carbon measurements and source apportionment using delta-C in Rochester, New York*, 2012. J. Air Waste Manage. Assoc., 62(8):880-7

Wang, P., Zhao, W., *Assessment of ambient volatile organic compounds (VOCs) near major roads in urban Nanjing, China,* 2008. Atmospheric Research, 89:289-297

Weijers, E.P., Khlystov, A.Y., Kos, G.P.A, Erisman, J.W., *Variability of particulate matter concentrations along roads and motorways determined by a moving measurement unit,* 2004. Atmos. Environ., 38:2993-3002

Zhou, Y., Levy, J.I., *Factors influencing the spatial extent of mobile source air pollution impacts: a meta-analysis*, 2007. BMC Public Health, 7:89

Zhu, Y., Kuhn, T., Mayo, P., Hinds, W.C., *Comparison of daytime and nighttime concentration profiles of size distributions of ultrafine particles near a major highway*, 2006. Environmental Science & Technology, 40:2531-2536

Zhu, Y.F., Hinds, W.C., Kim, S., Sioutas, C., *Concentration and size distribution of ultrafine particles near a major highway,* 2002. J. Air Waste Manag. Assoc., 52:1032-1042

Zwack, L.M., Paciorek, C.J., Spengler, J.D., Levy, J.I., *Modeling spatial patters of traffic-related air pollutants in complex urban terrain*, 2011a. Environmental Health Perspectives, 119(6):852-859

Zwack, L.M., Pacioreck, C.J., Spengler, J.D., Levy, J.I., *Characterizing local traffic contributions to particulate air pollution in street canyons using mobile monitoring techniques*, 2011b. Atmos. Environ., 45:2507-2514

Appendix A1 - Time-Series Plots of the Entire Mobile Monitoring Campaign for Each Sampling Day

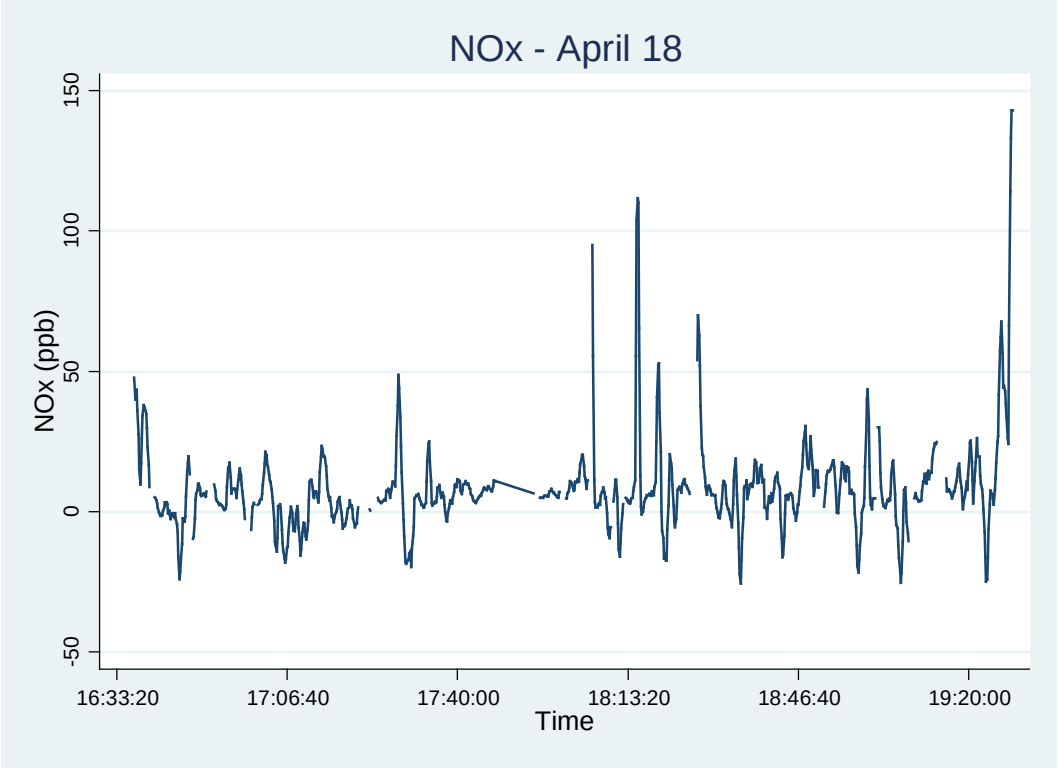

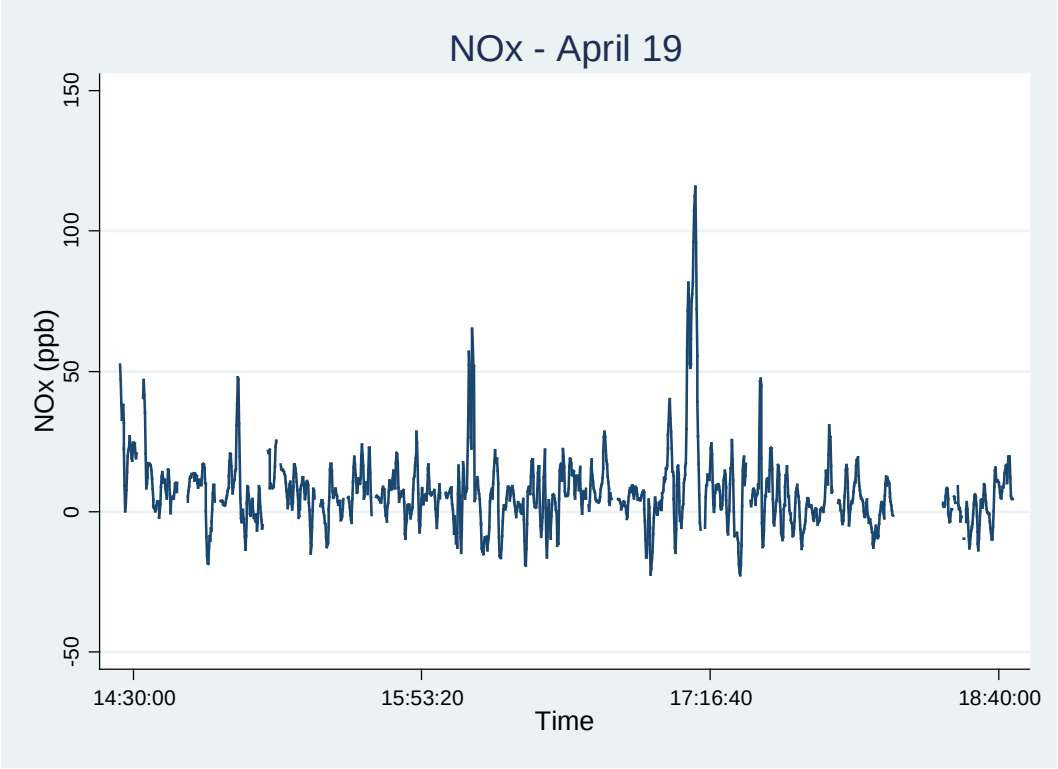

Appendix A1 - Time-Series Plots of the Entire Mobile Monitoring Campaign for Each Sampling Day

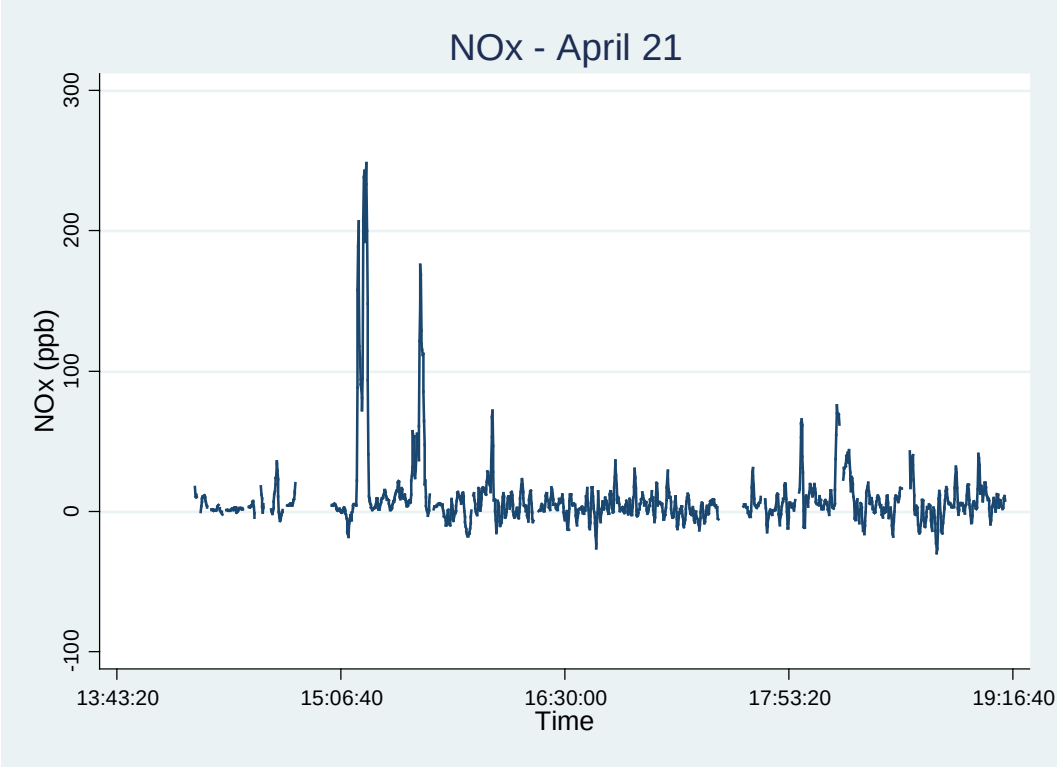

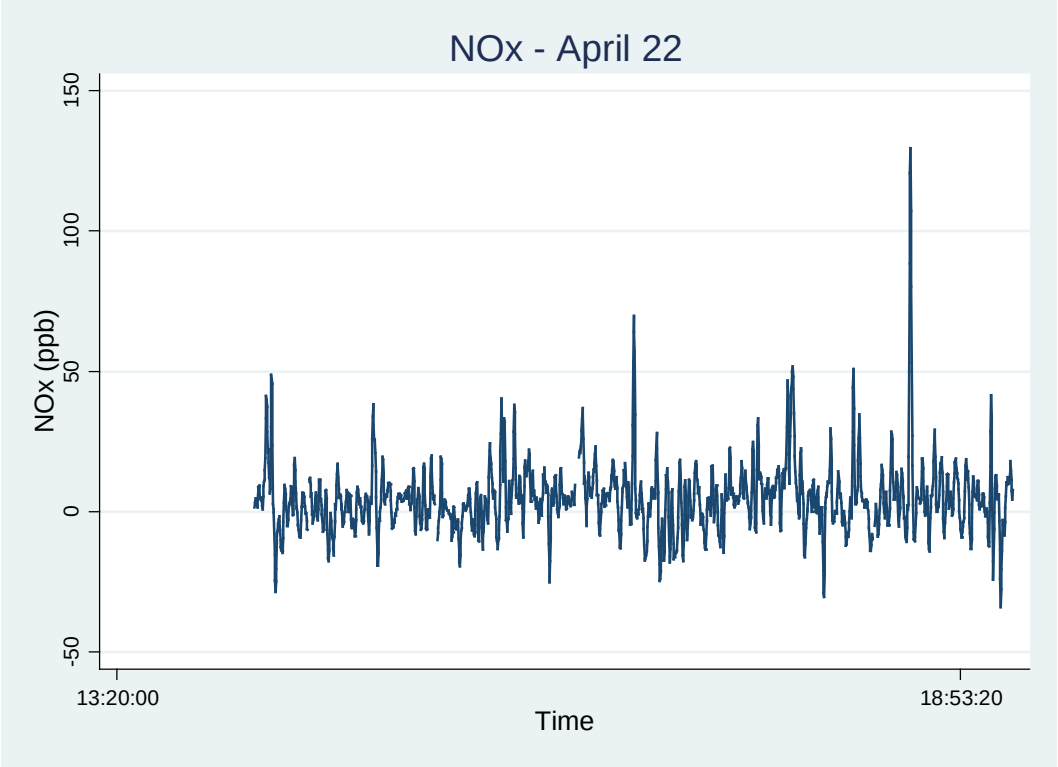

Appendix A1 - Time-Series Plots of the Entire Mobile Monitoring Campaign for Each Sampling Day

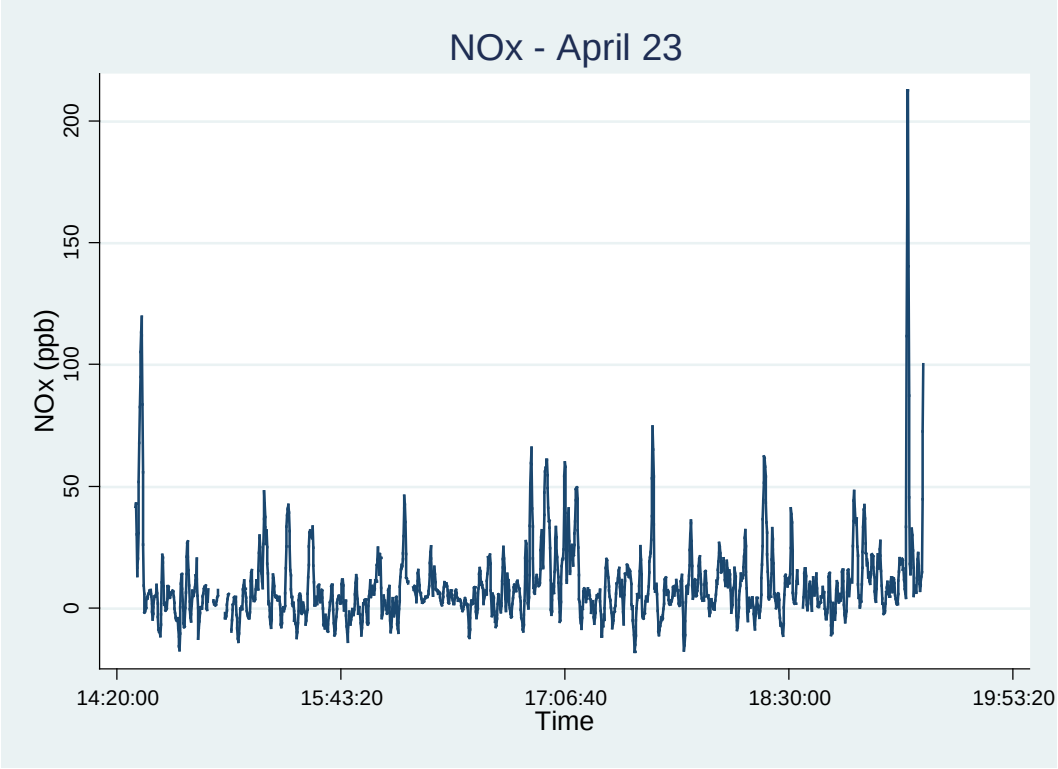

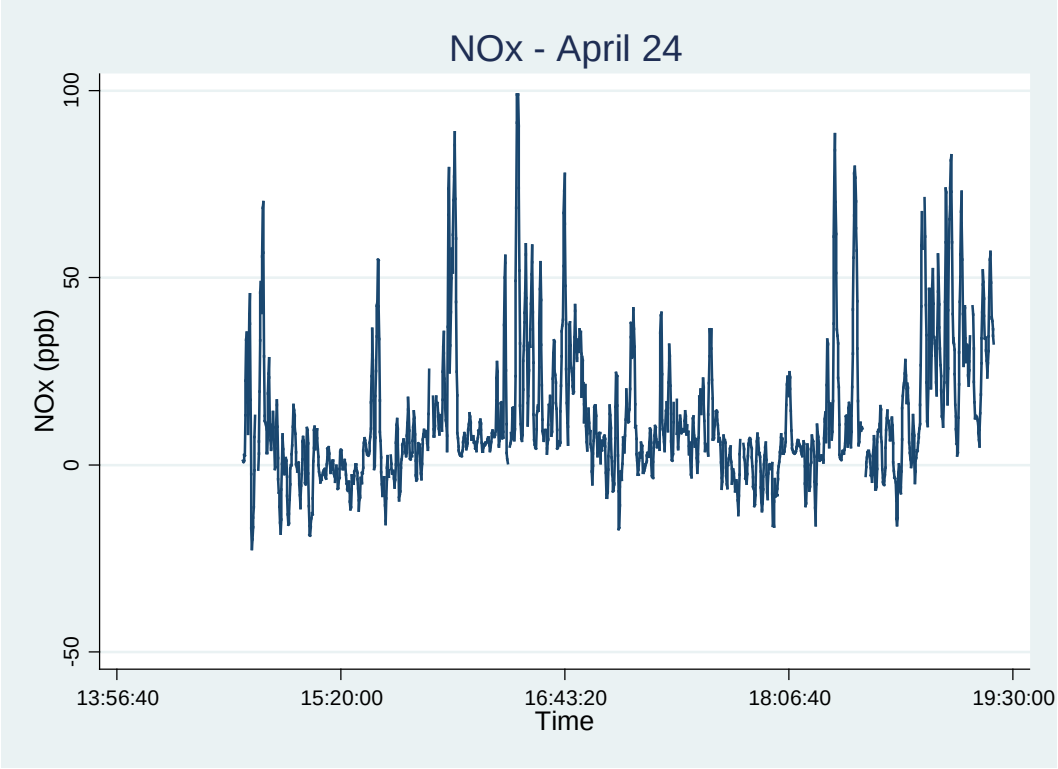

Appendix A1 - Time-Series Plots of the Entire Mobile Monitoring Campaign for Each Sampling Day

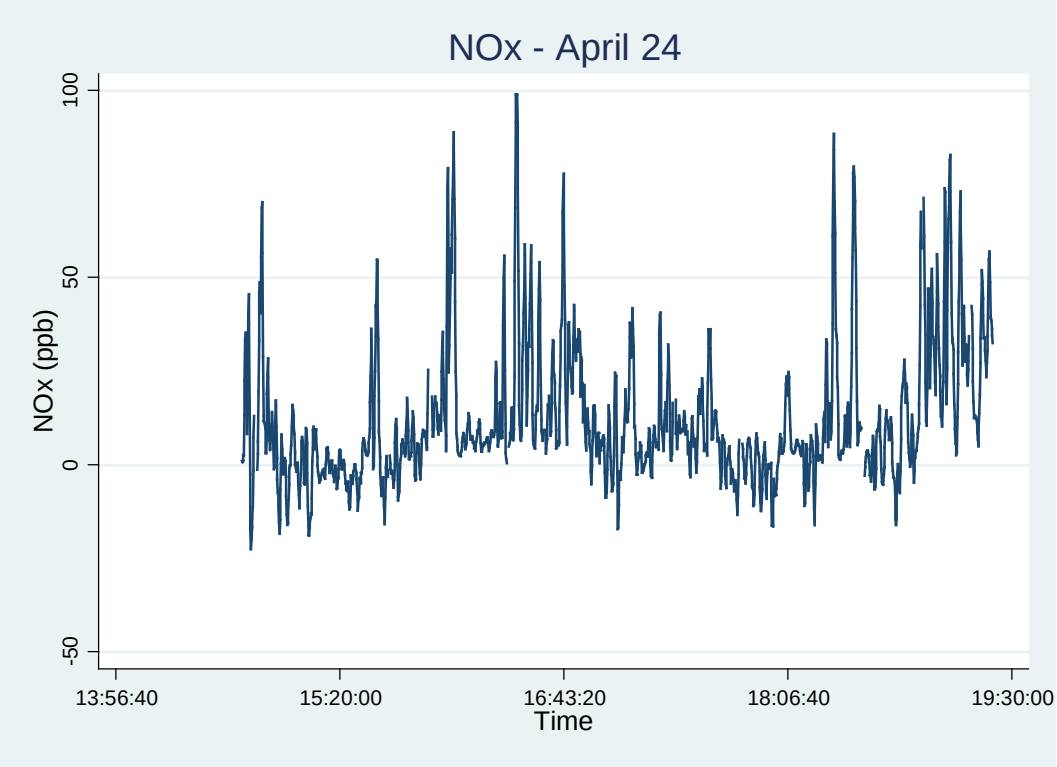

Appendix A2 - Time-Series Plots of the Entire Mobile Monitoring Campaign for Each Sampling Day

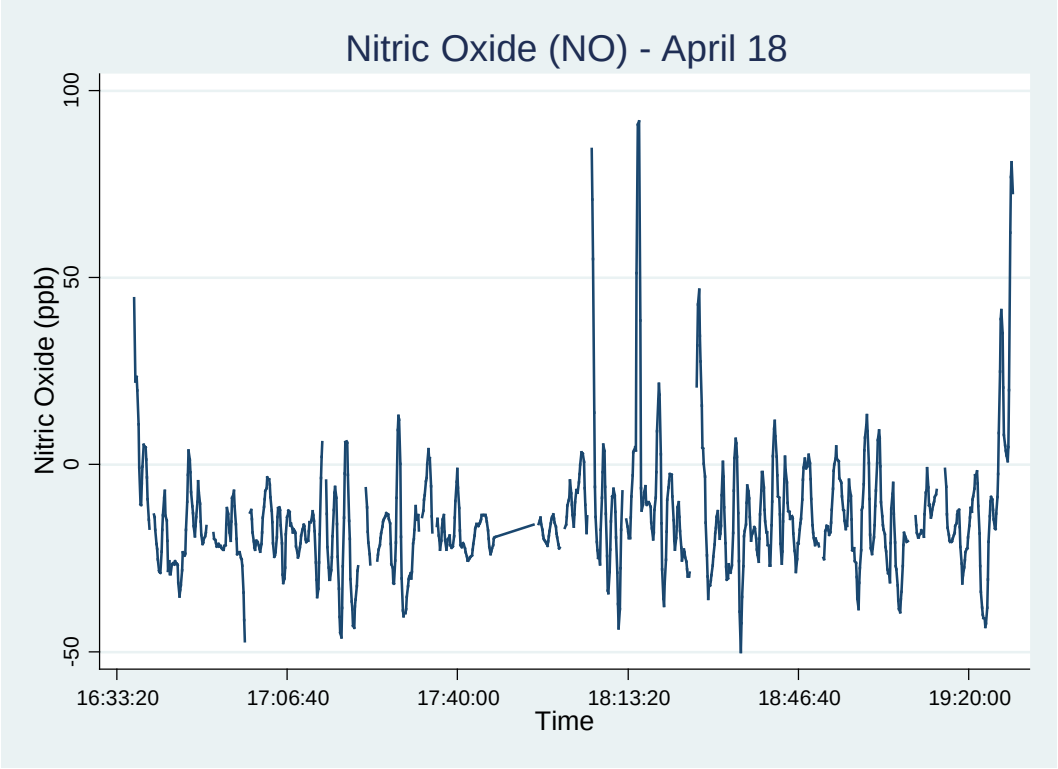

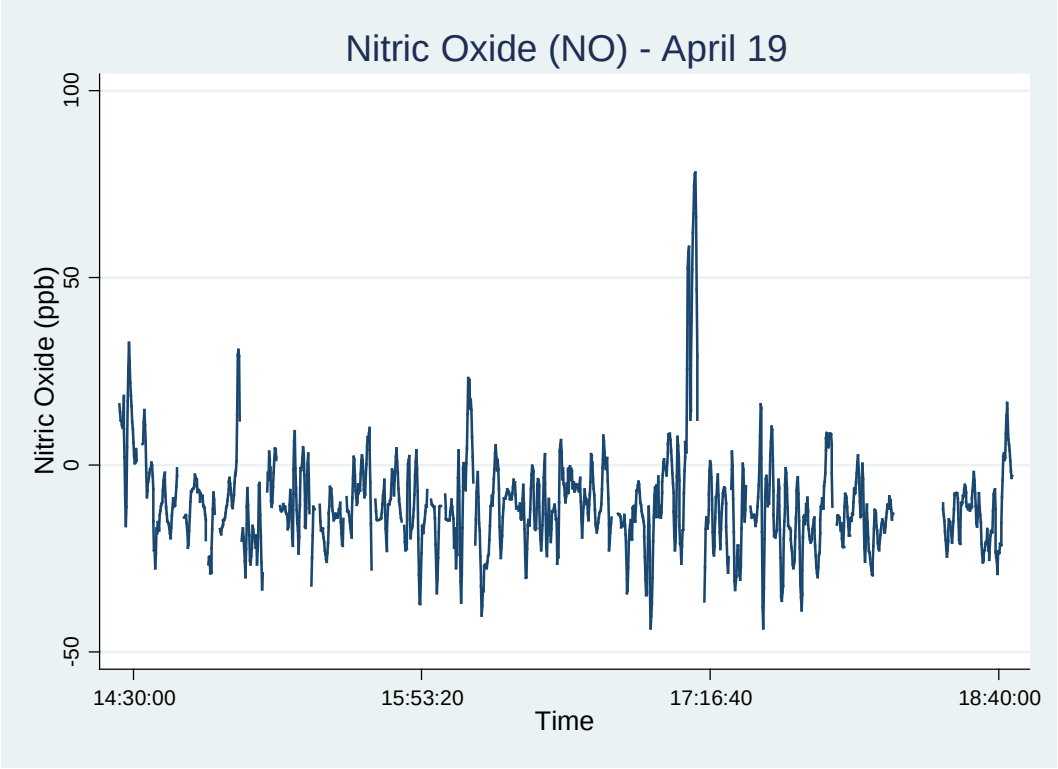

Appendix A2 - Time-Series Plots of the Entire Mobile Monitoring Campaign for Each Sampling Day

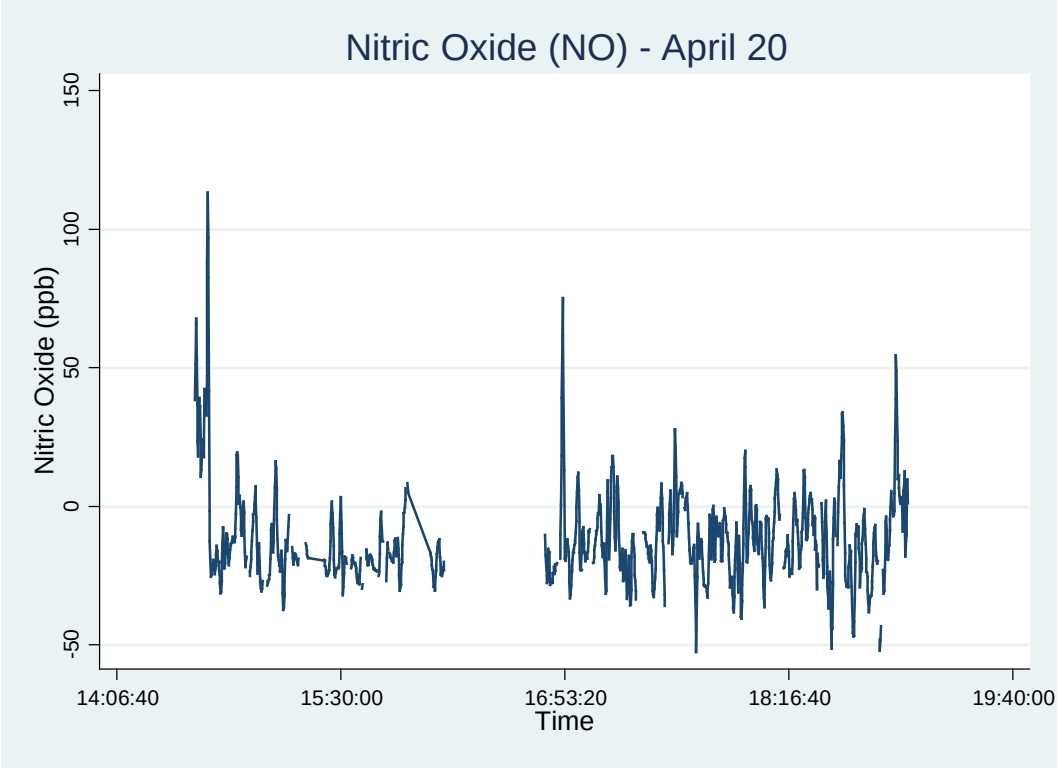

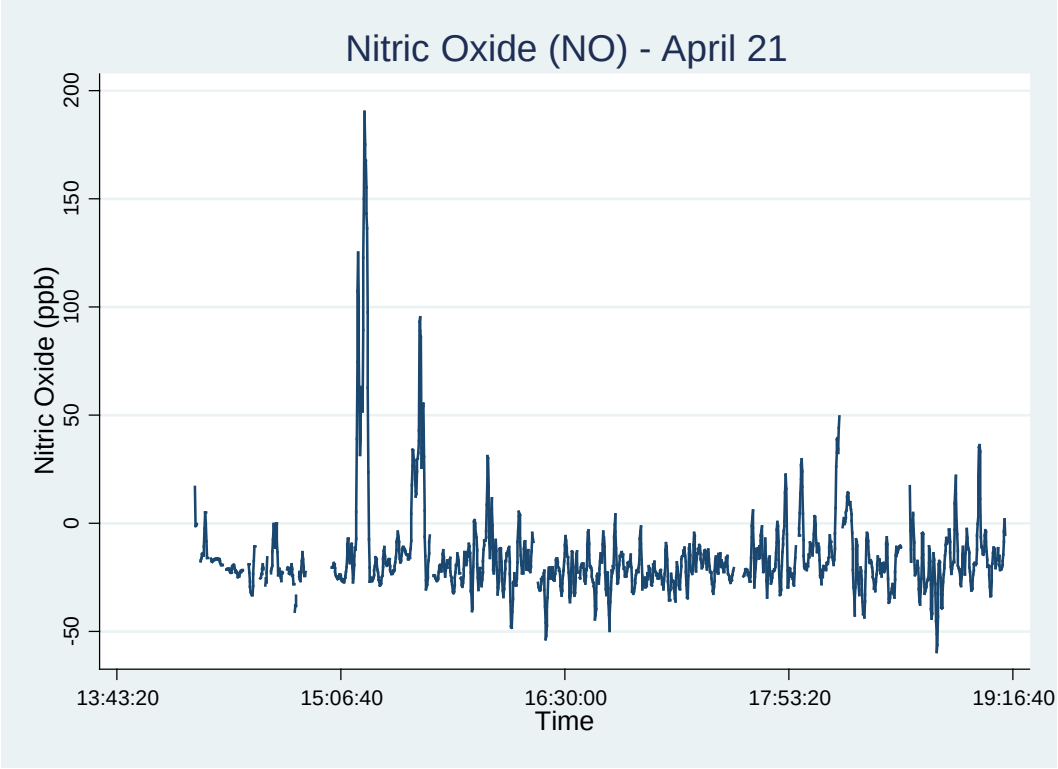

Appendix A2 - Time-Series Plots of the Entire Mobile Monitoring Campaign for Each Sampling Day

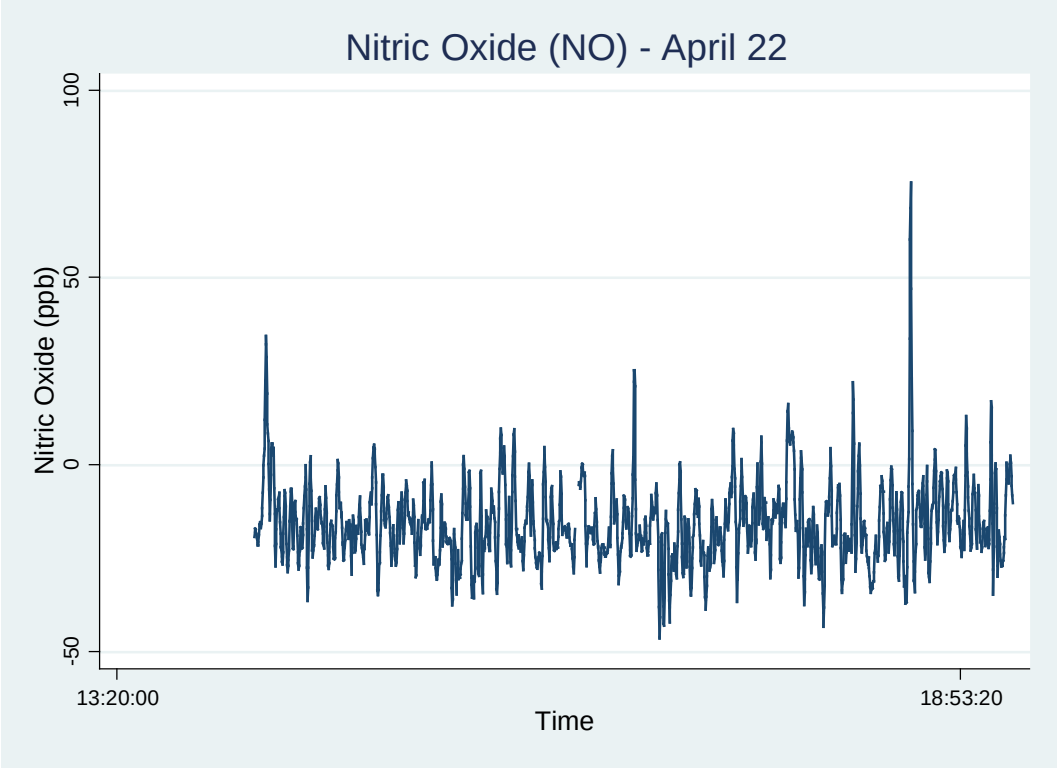

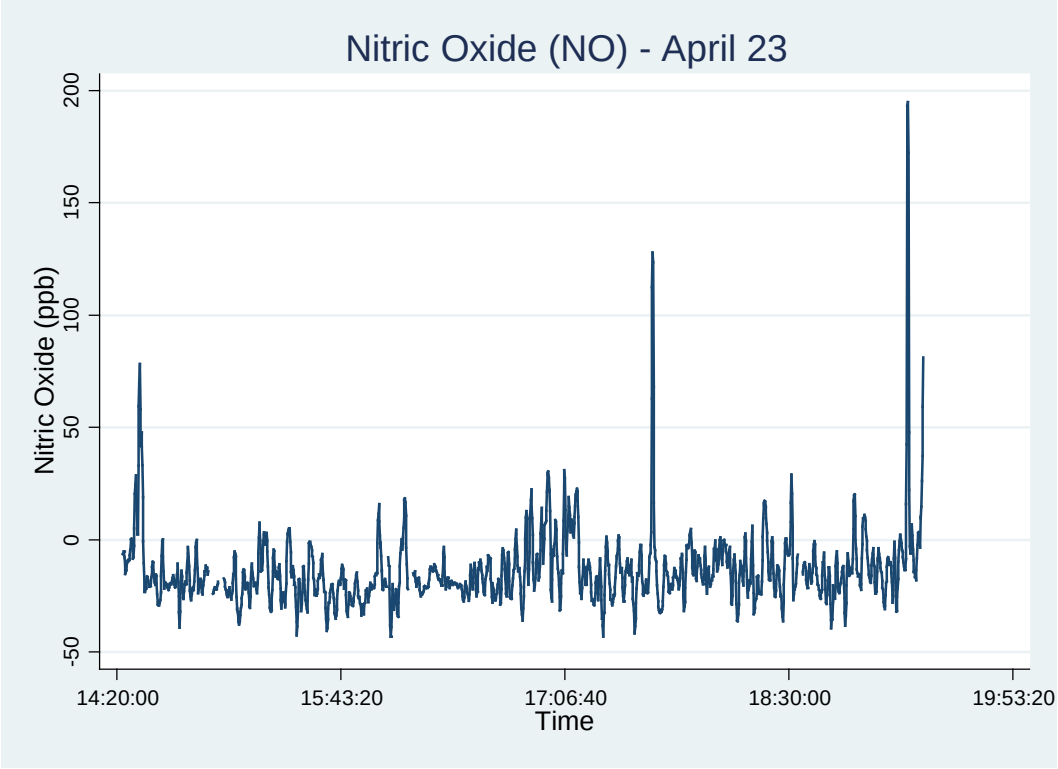

Appendix A2 - Time-Series Plots of the Entire Mobile Monitoring Campaign for Each Sampling Day

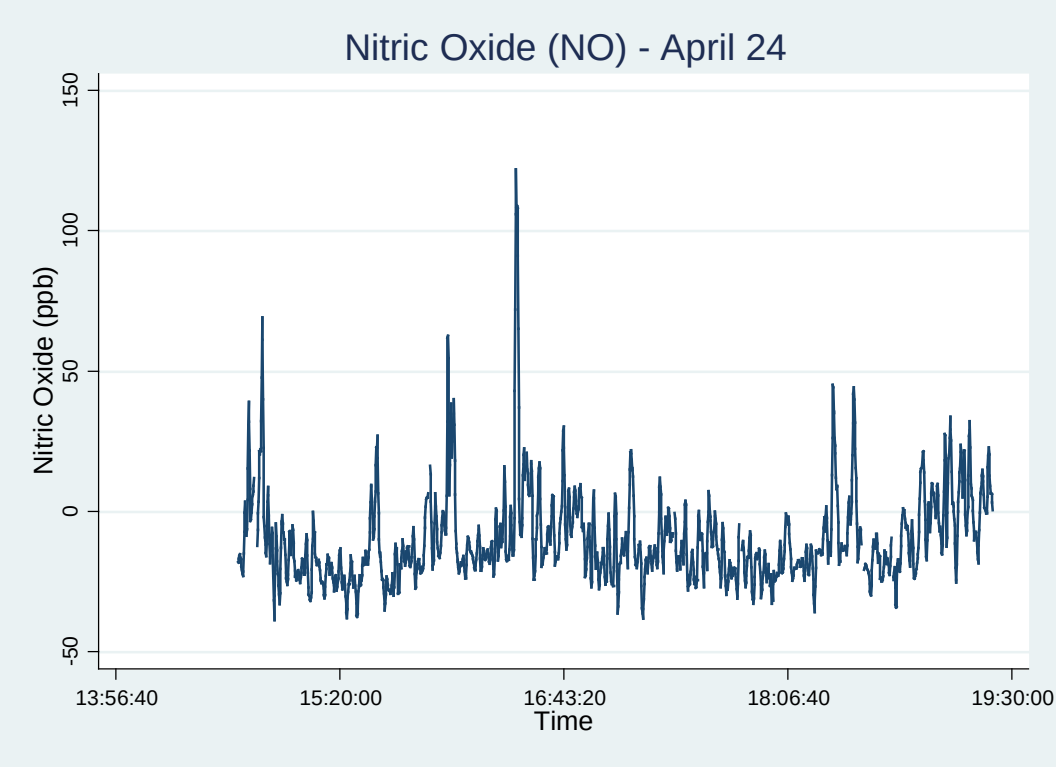

Appendix A3 - Time-Series Plots of the Entire Mobile Monitoring Campaign for Each Sampling Day

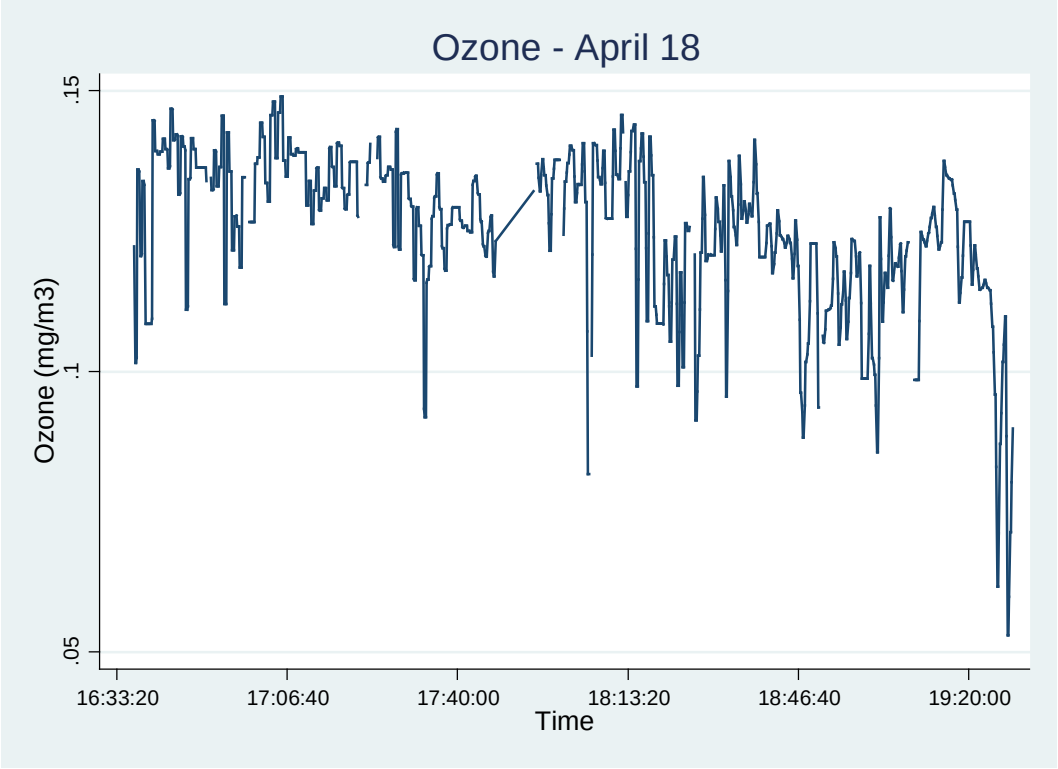

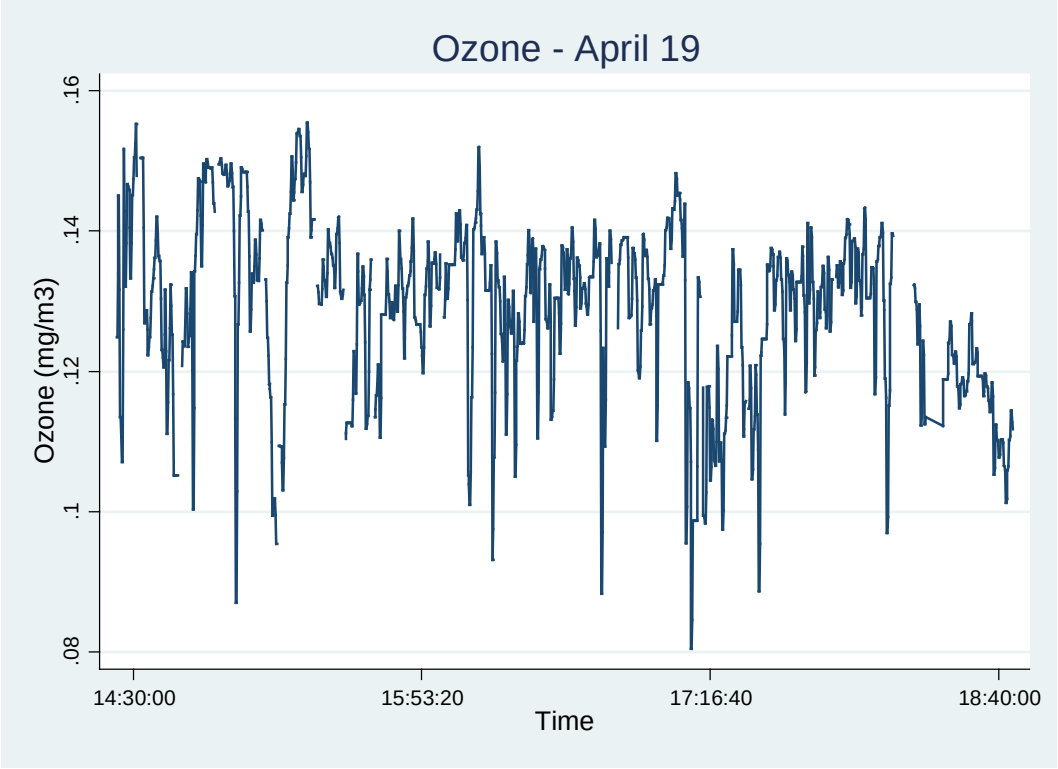

Appendix A3 - Time-Series Plots of the Entire Mobile Monitoring Campaign for Each Sampling Day

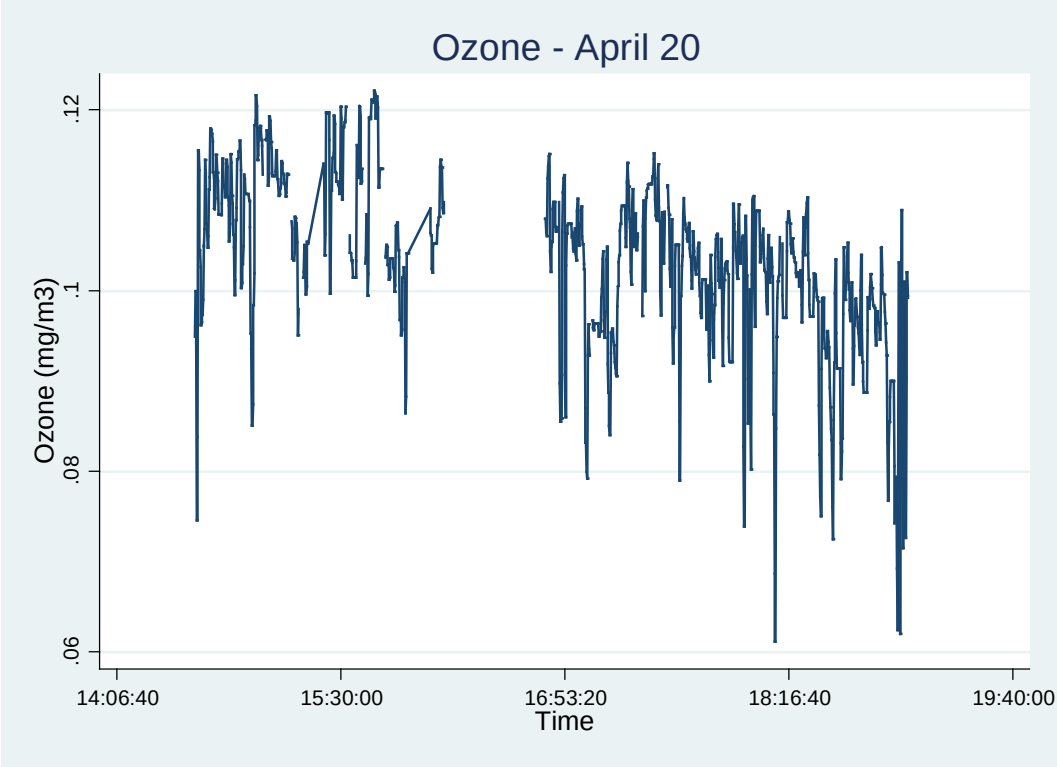

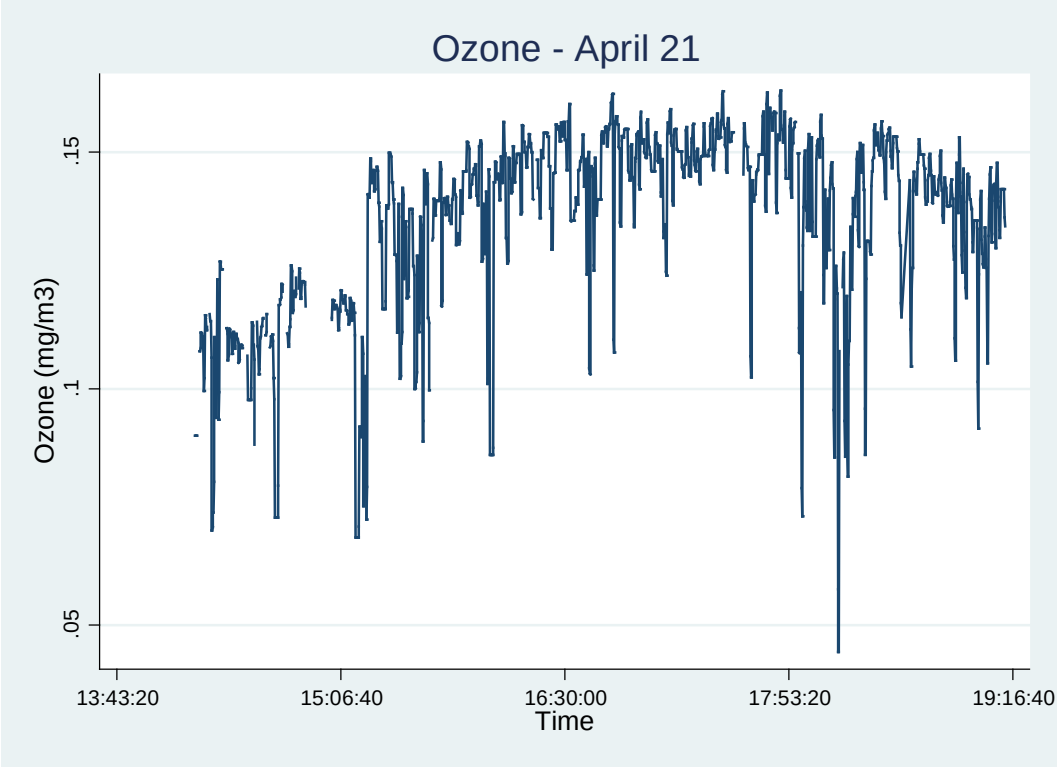

Appendix A3 - Time-Series Plots of the Entire Mobile Monitoring Campaign for Each Sampling Day

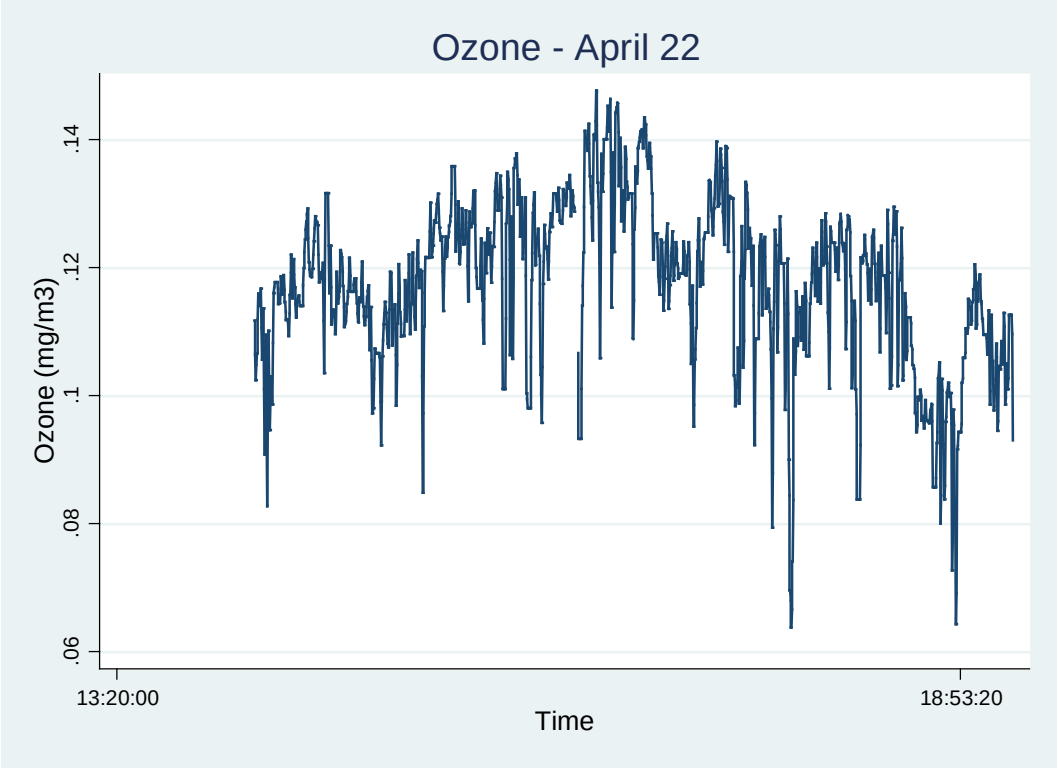

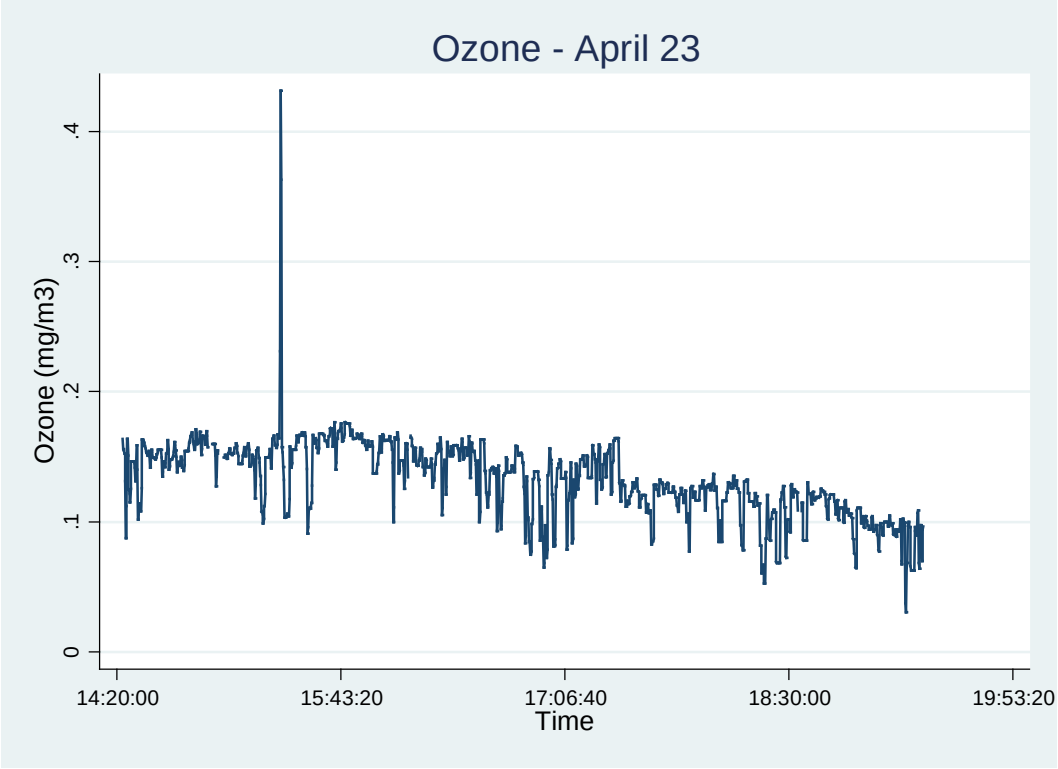

Appendix A3 - Time-Series Plots of the Entire Mobile Monitoring Campaign for Each Sampling Day

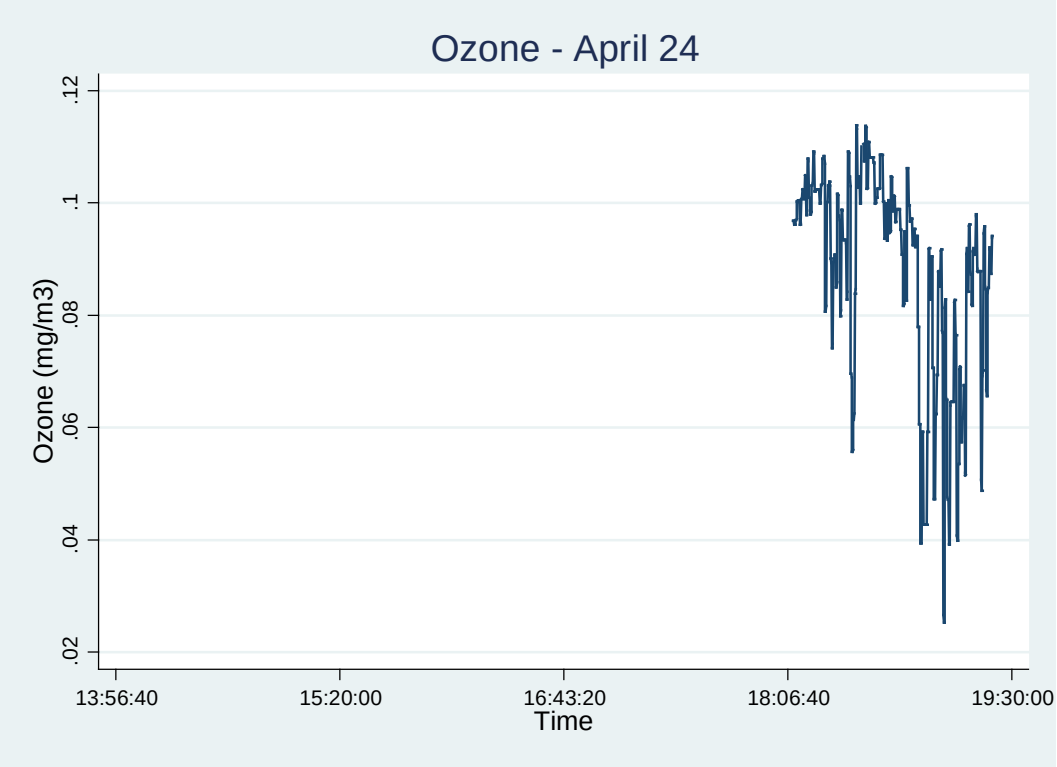

Appendix A4 - Time-Series Plots of the Entire Mobile Monitoring Campaign for Each Sampling Day

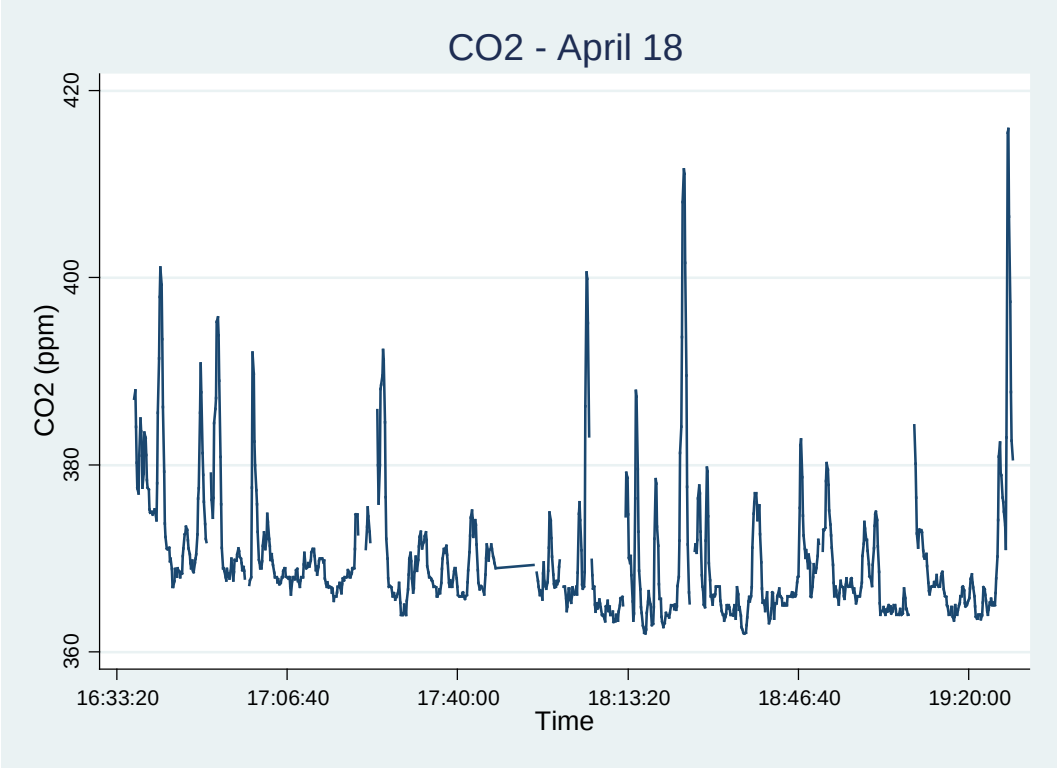

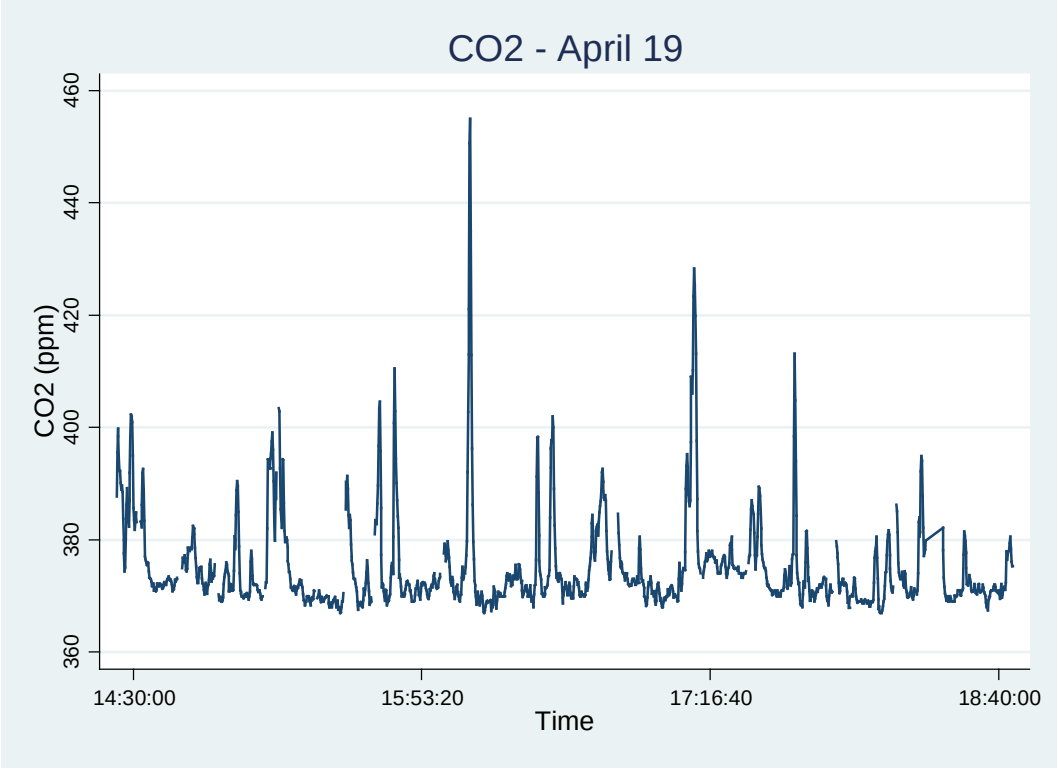

Appendix A4 - Time-Series Plots of the Entire Mobile Monitoring Campaign for Each Sampling Day

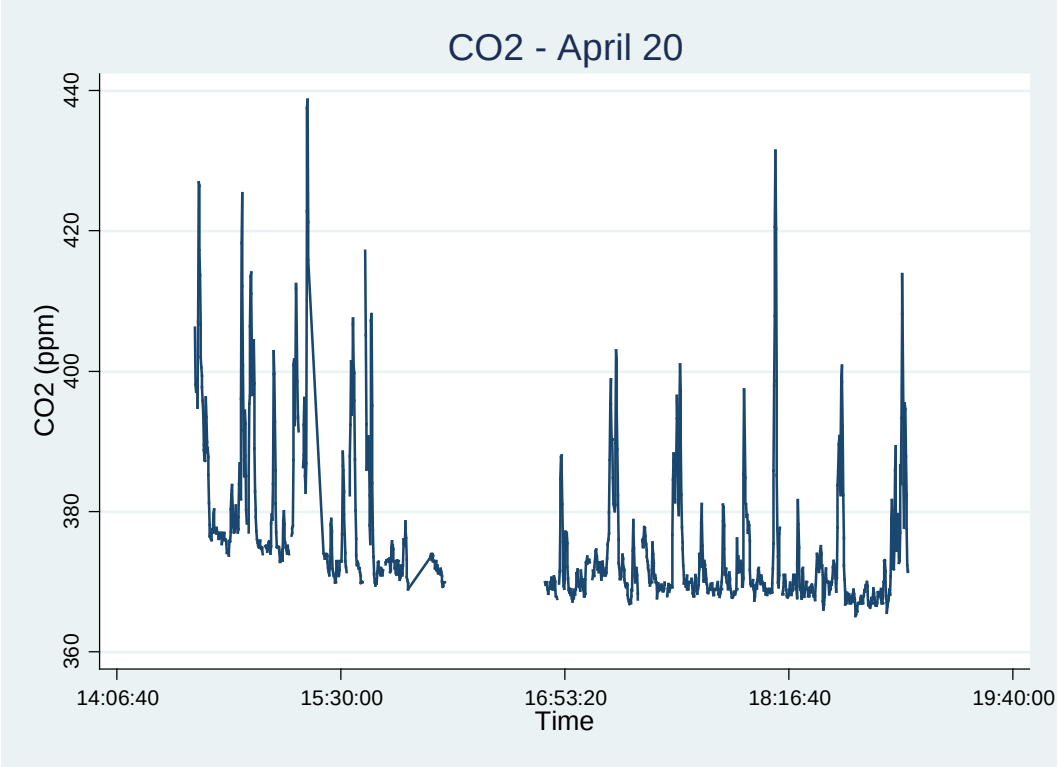

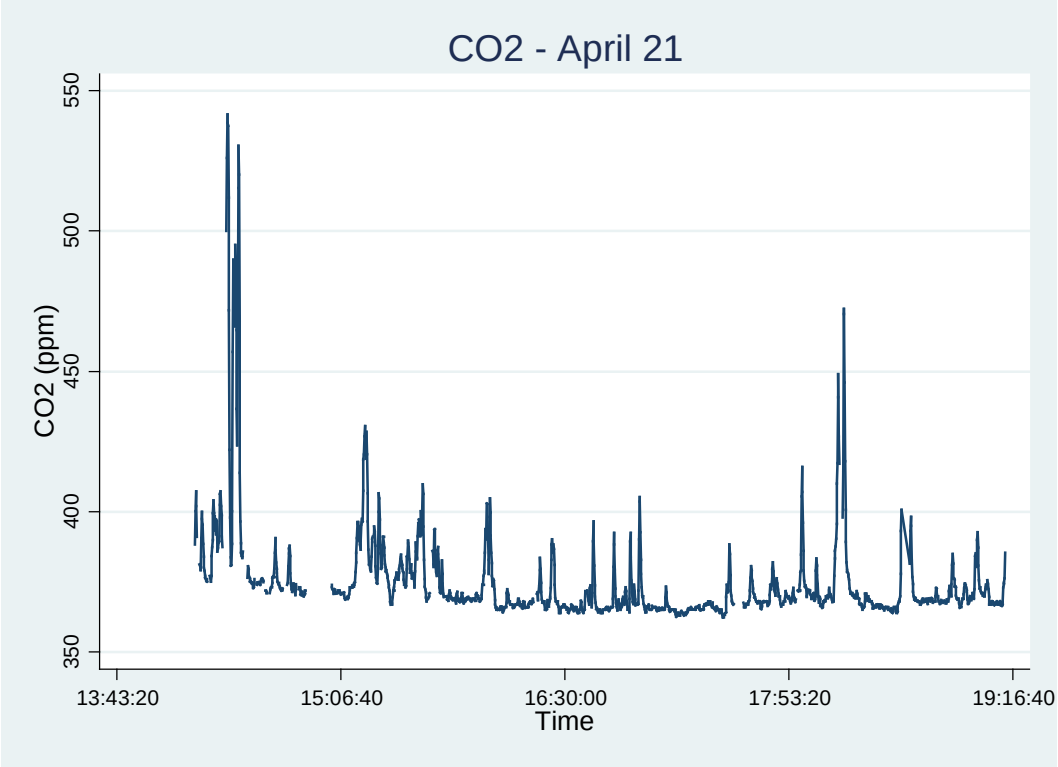

Appendix A4 - Time-Series Plots of the Entire Mobile Monitoring Campaign for Each Sampling Day

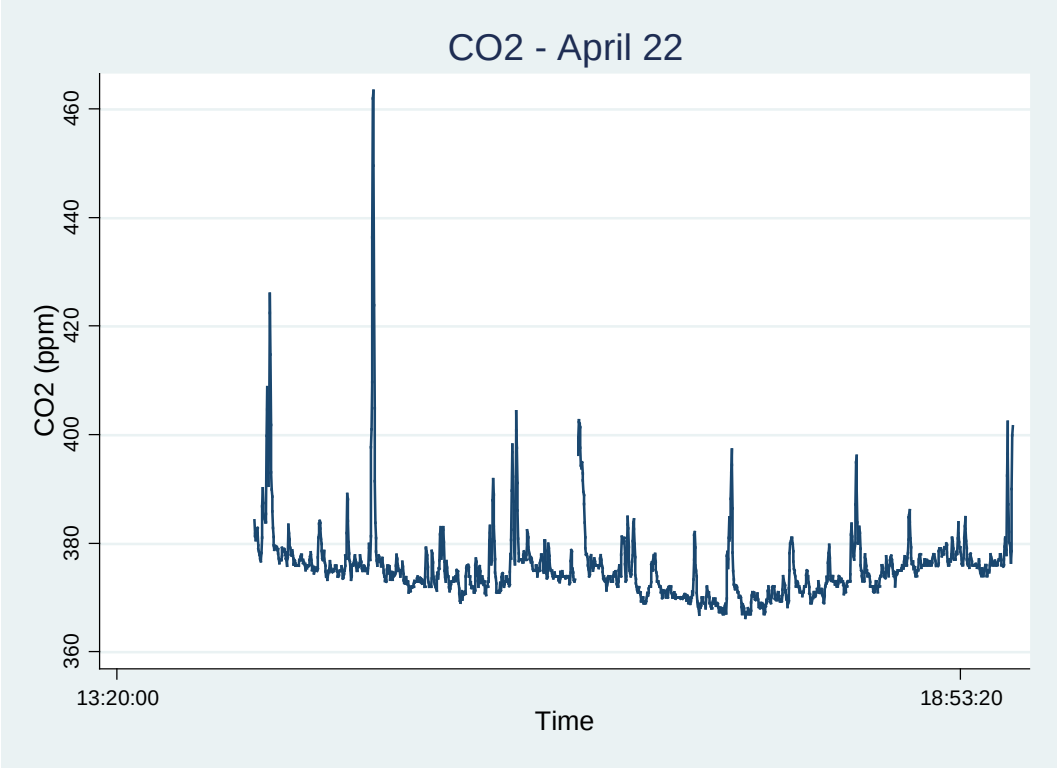

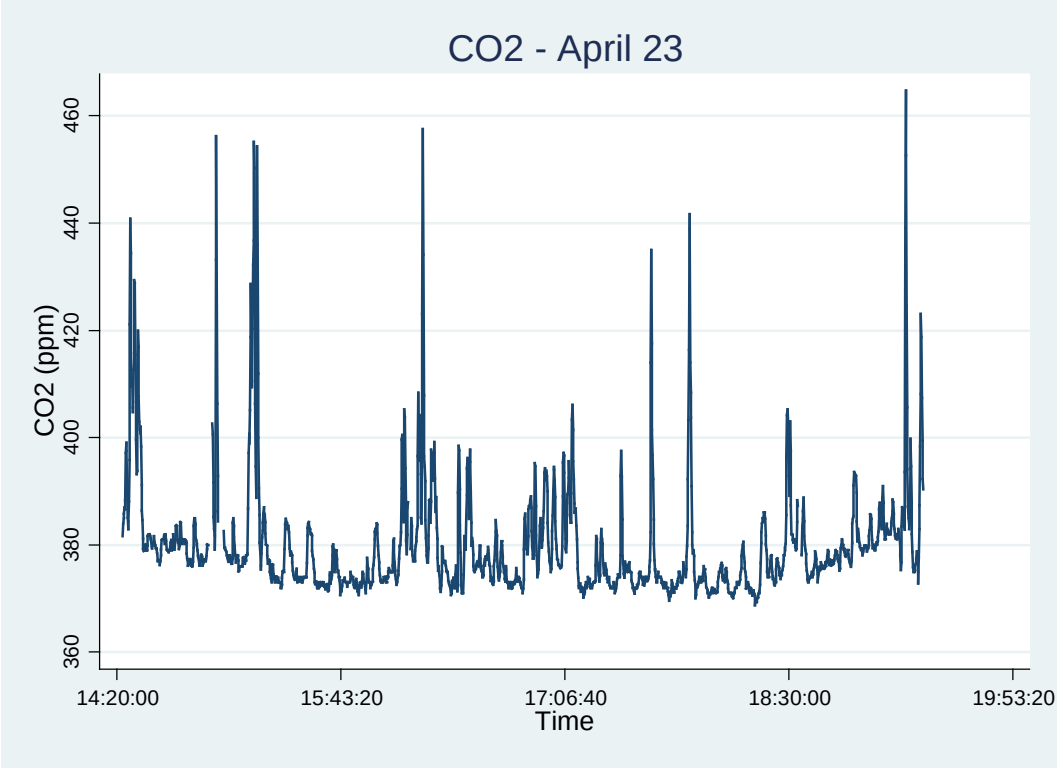

Appendix A4 - Time-Series Plots of the Entire Mobile Monitoring Campaign for Each Sampling Day

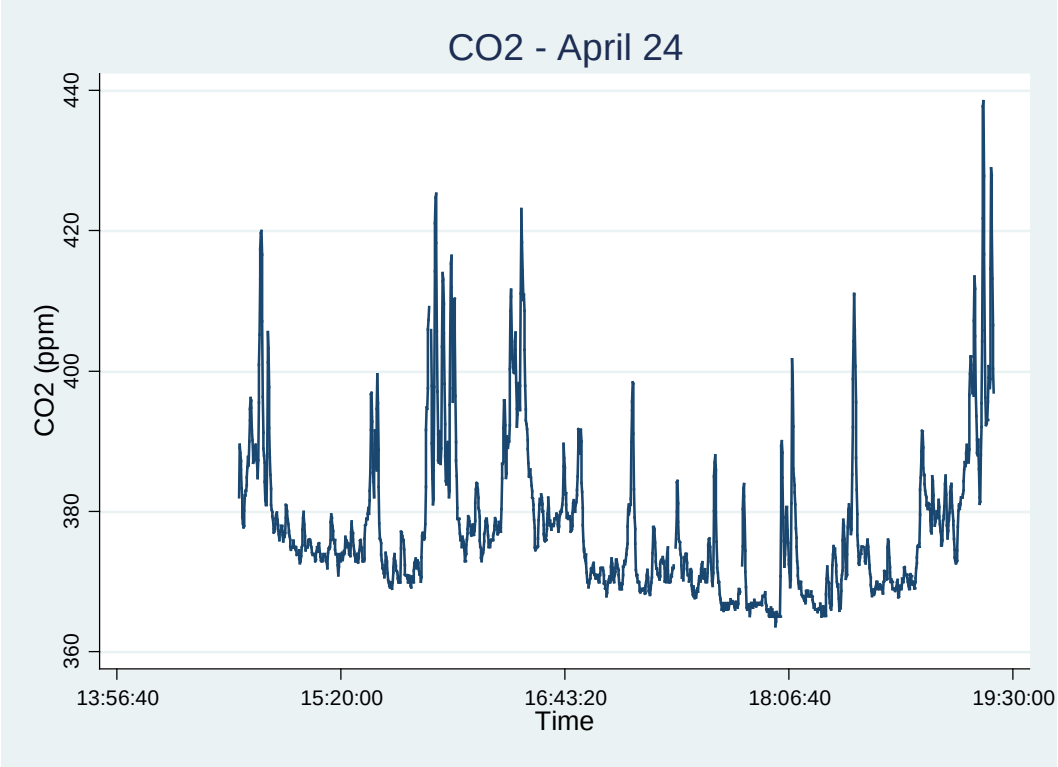

Appendix A5- Time-Series Plots of the Entire Mobile Monitoring Campaign for Each Sampling Day

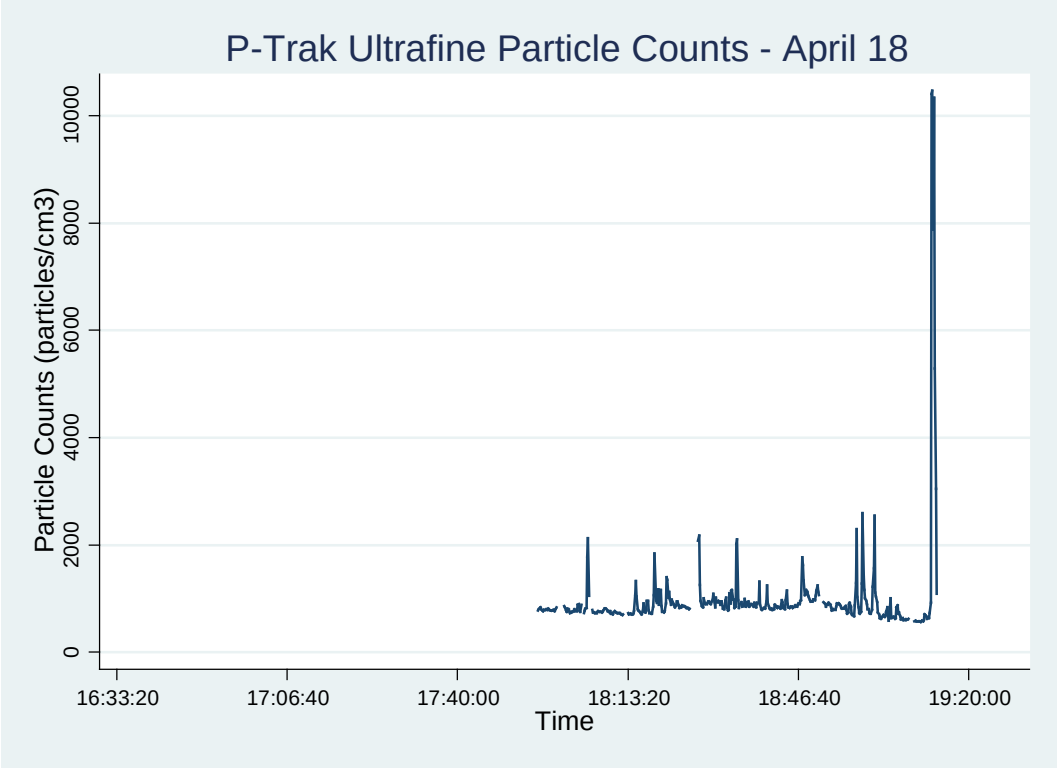

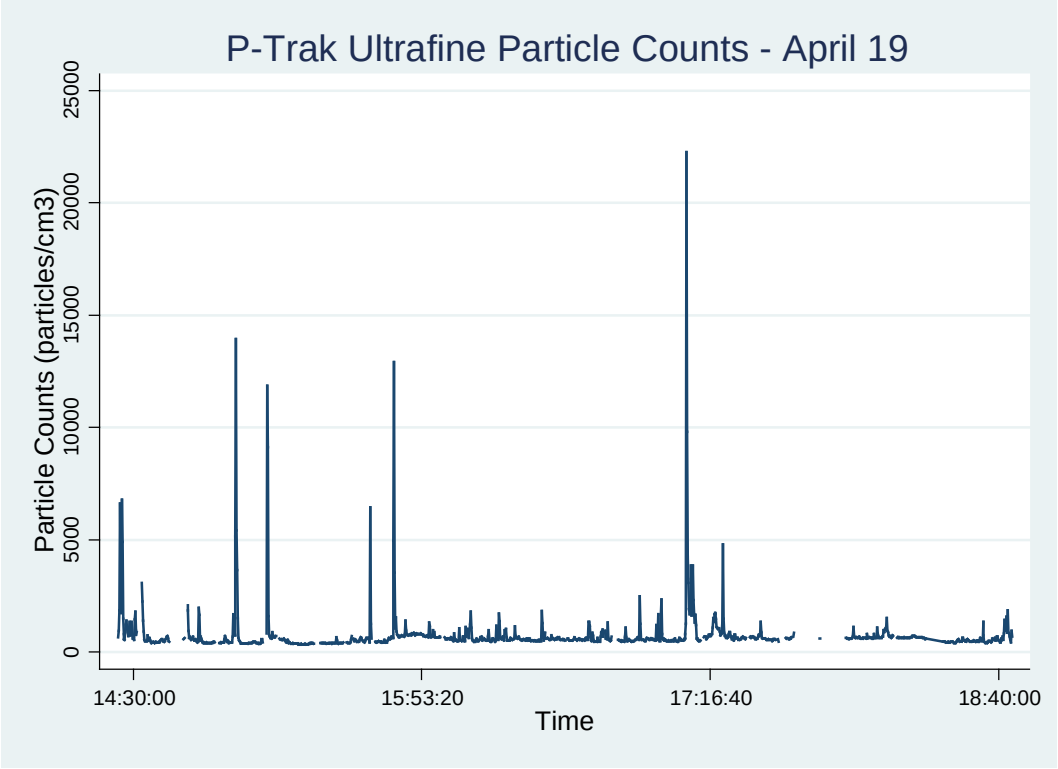

Appendix A5- Time-Series Plots of the Entire Mobile Monitoring Campaign for Each Sampling Day

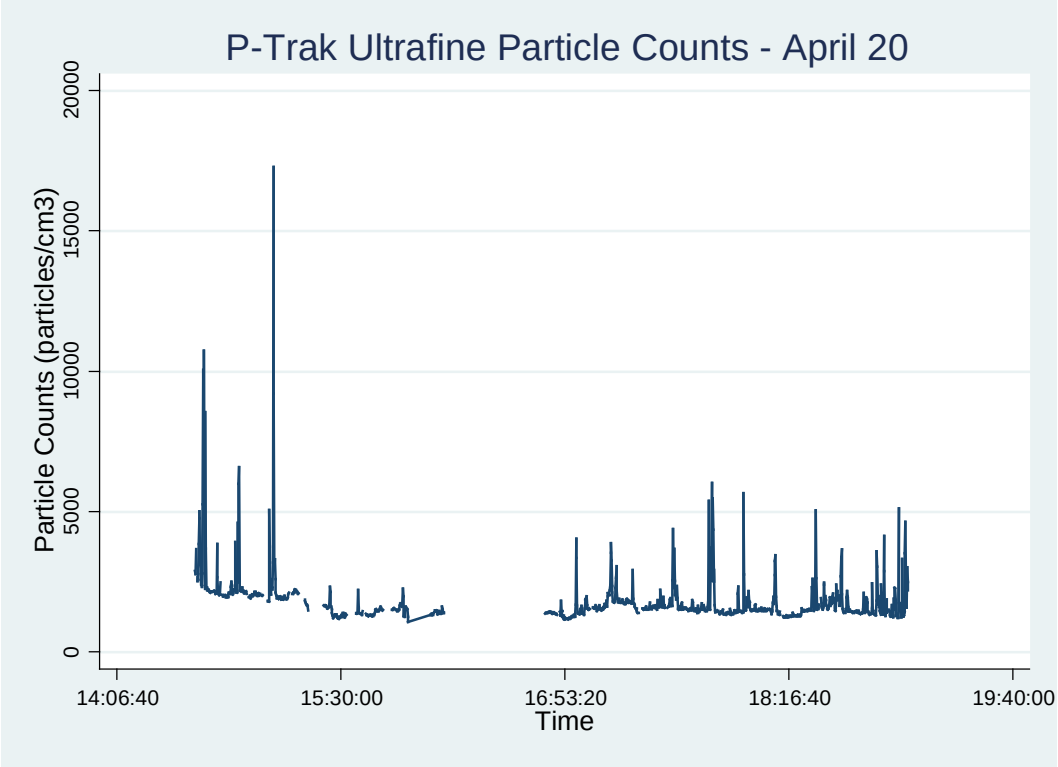

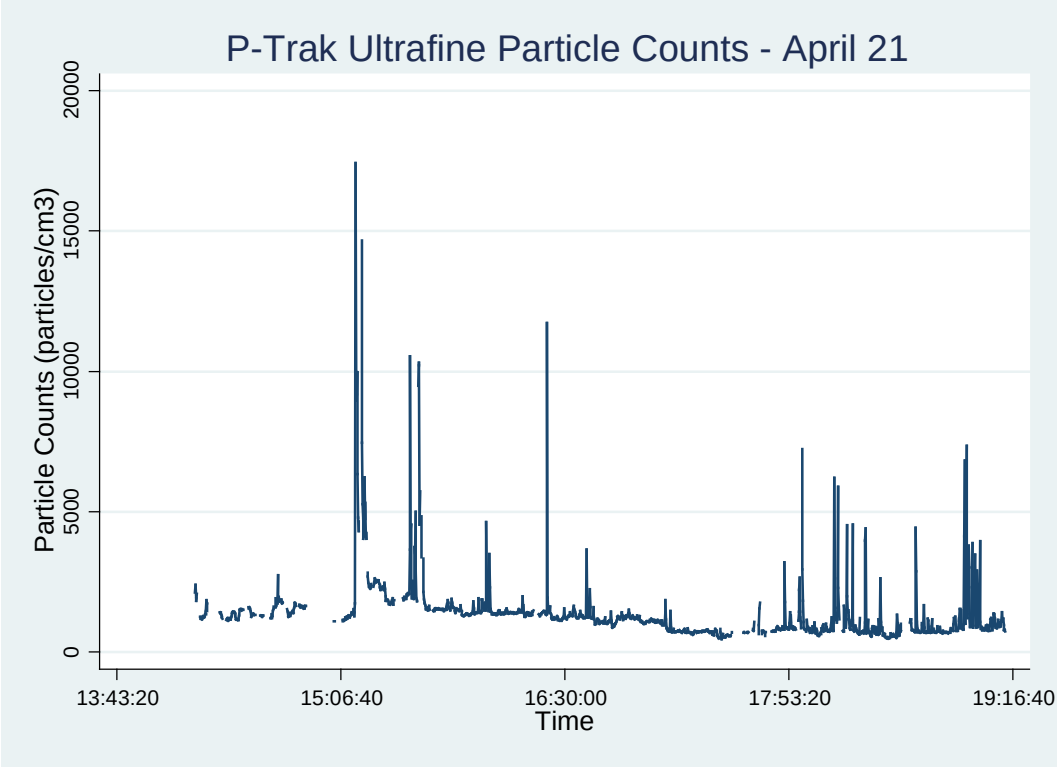

Appendix A5- Time-Series Plots of the Entire Mobile Monitoring Campaign for Each Sampling Day

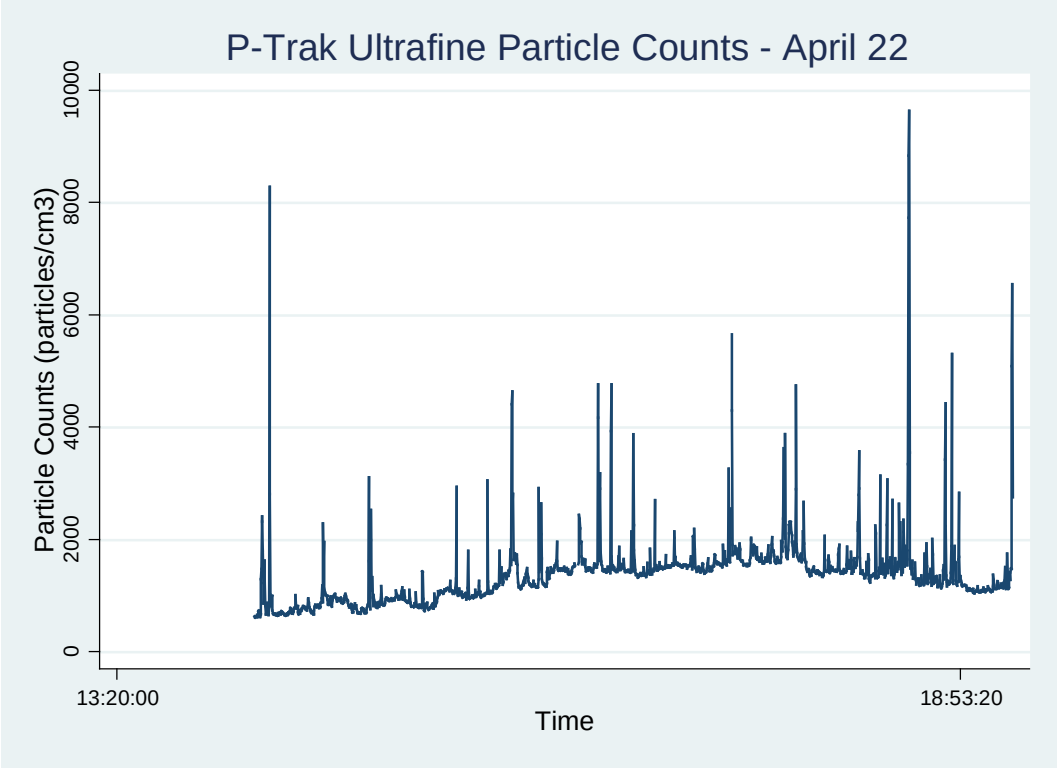

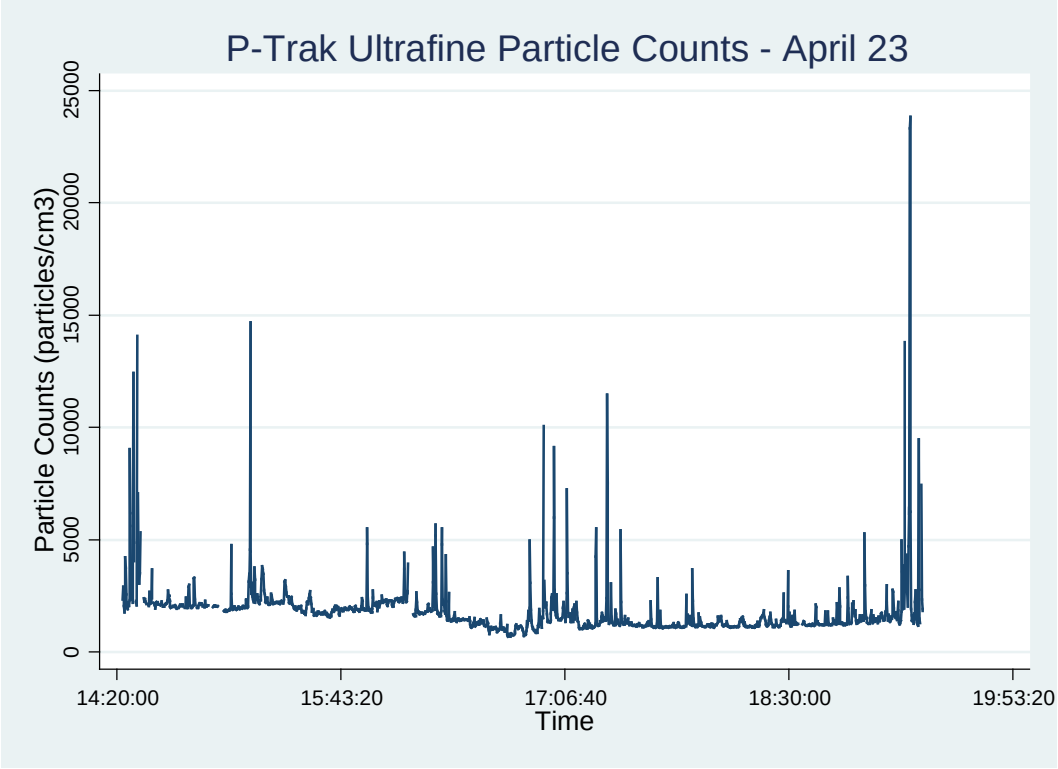

Appendix A5- Time-Series Plots of the Entire Mobile Monitoring Campaign for Each Sampling Day

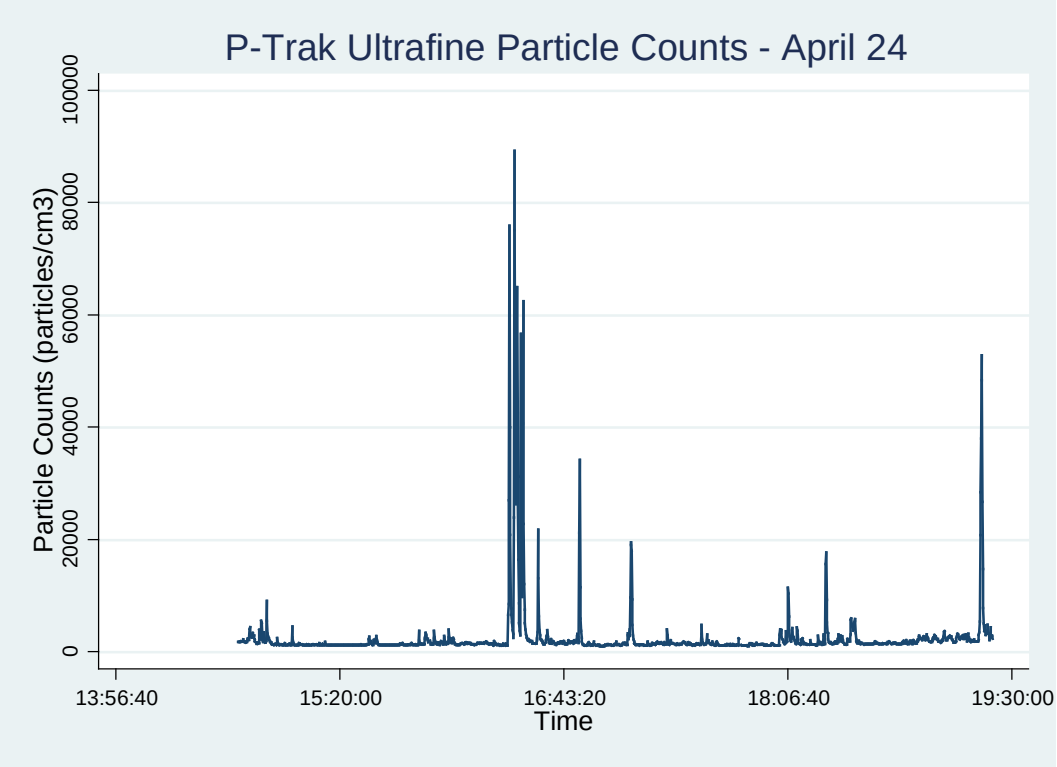

Appendix A6- Time-Series Plots of the Entire Mobile Monitoring Campaign for Each Sampling Day

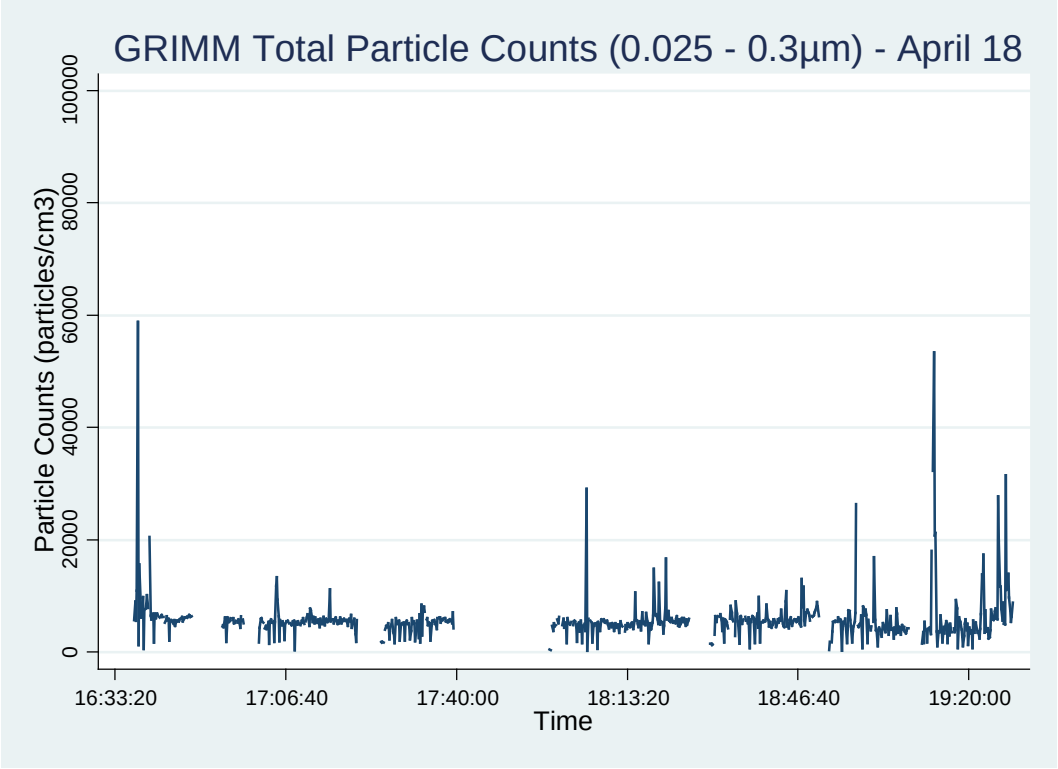

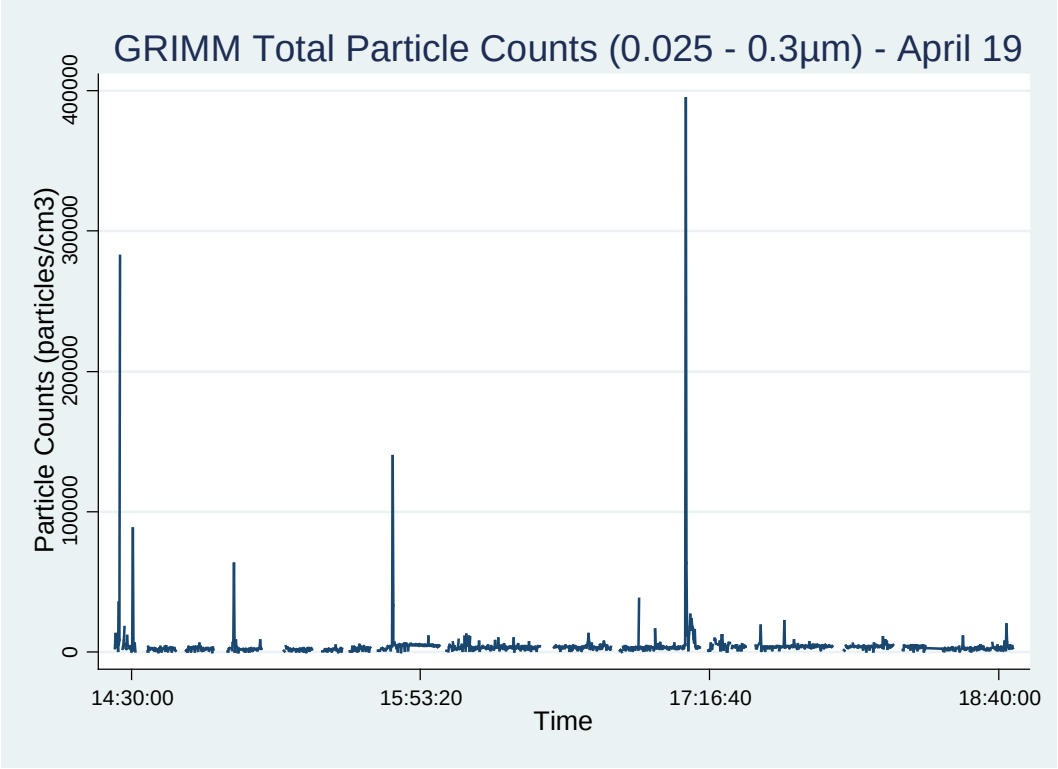

Appendix A6- Time-Series Plots of the Entire Mobile Monitoring Campaign for Each Sampling Day

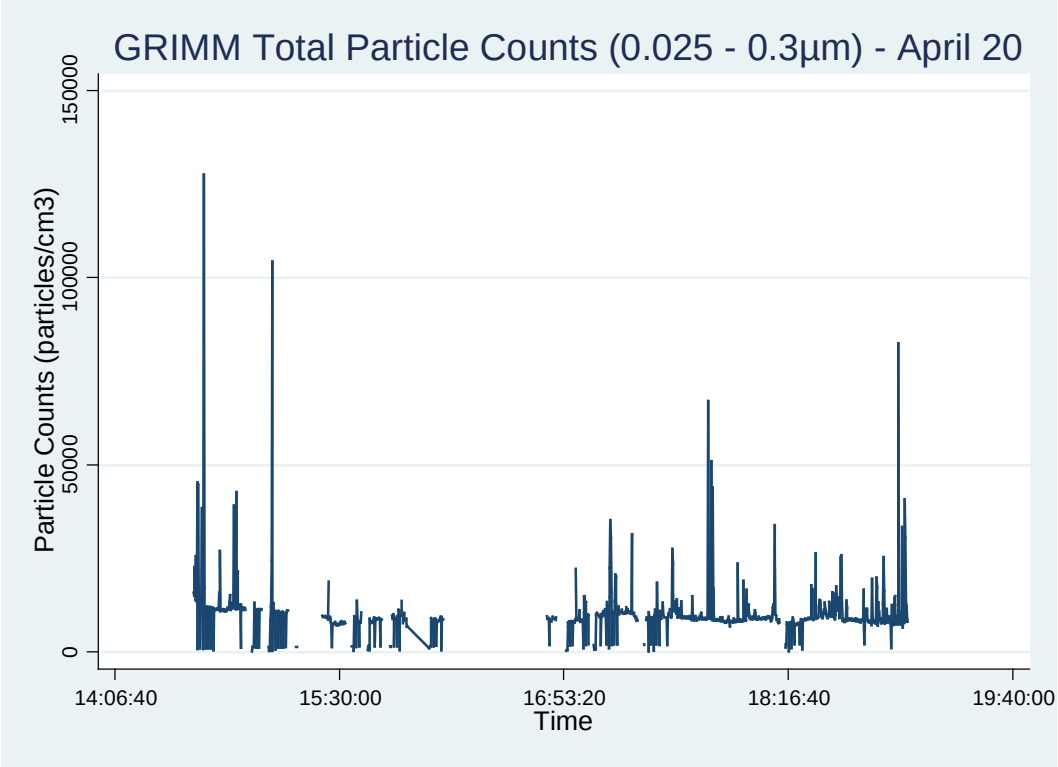

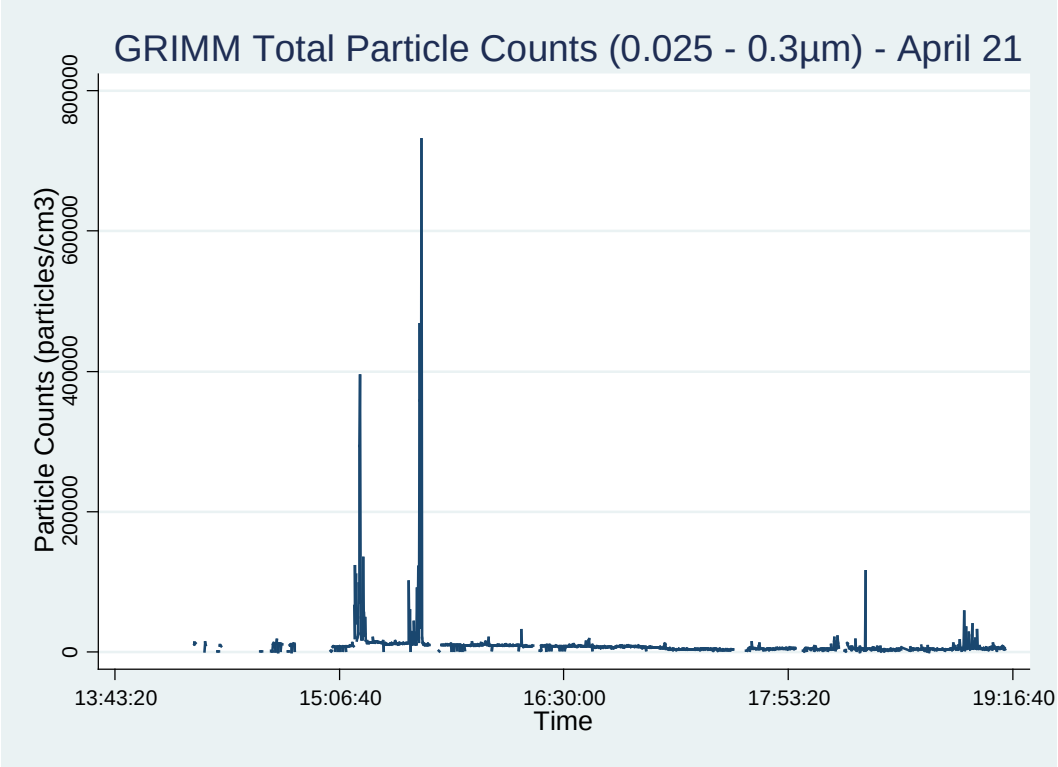

Appendix A6- Time-Series Plots of the Entire Mobile Monitoring Campaign for Each Sampling Day

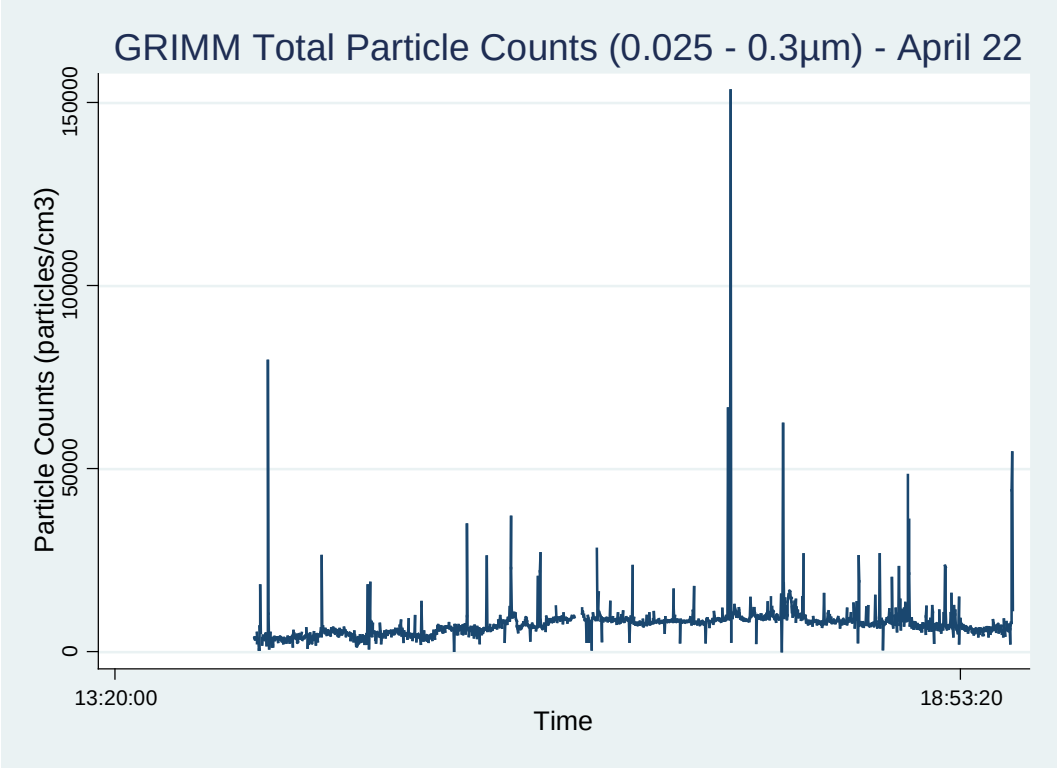

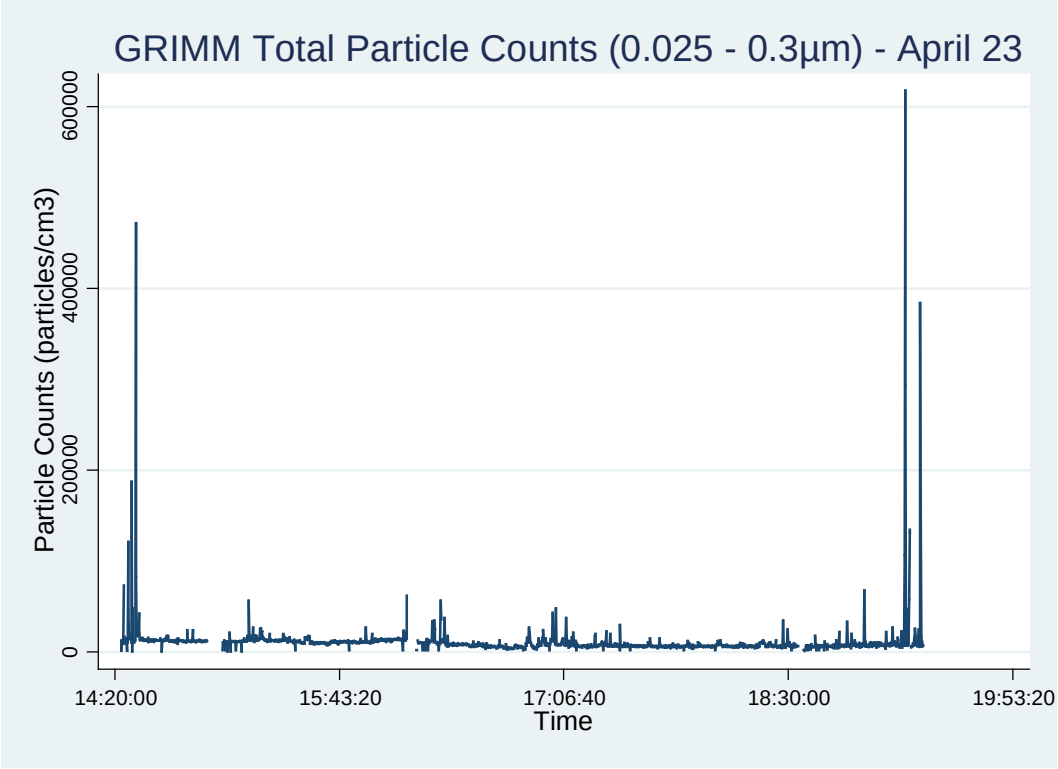

Appendix A6- Time-Series Plots of the Entire Mobile Monitoring Campaign for Each Sampling Day

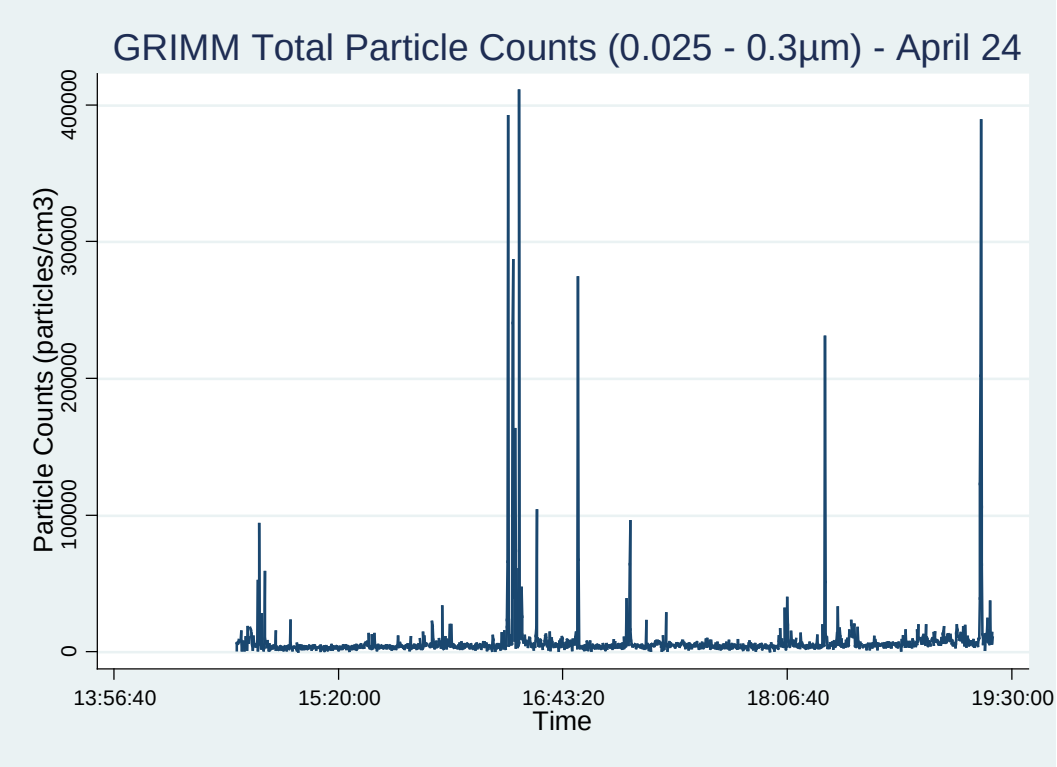

Appendix A7- Time-Series Plots of the Entire Mobile Monitoring Campaign for Each Sampling Day

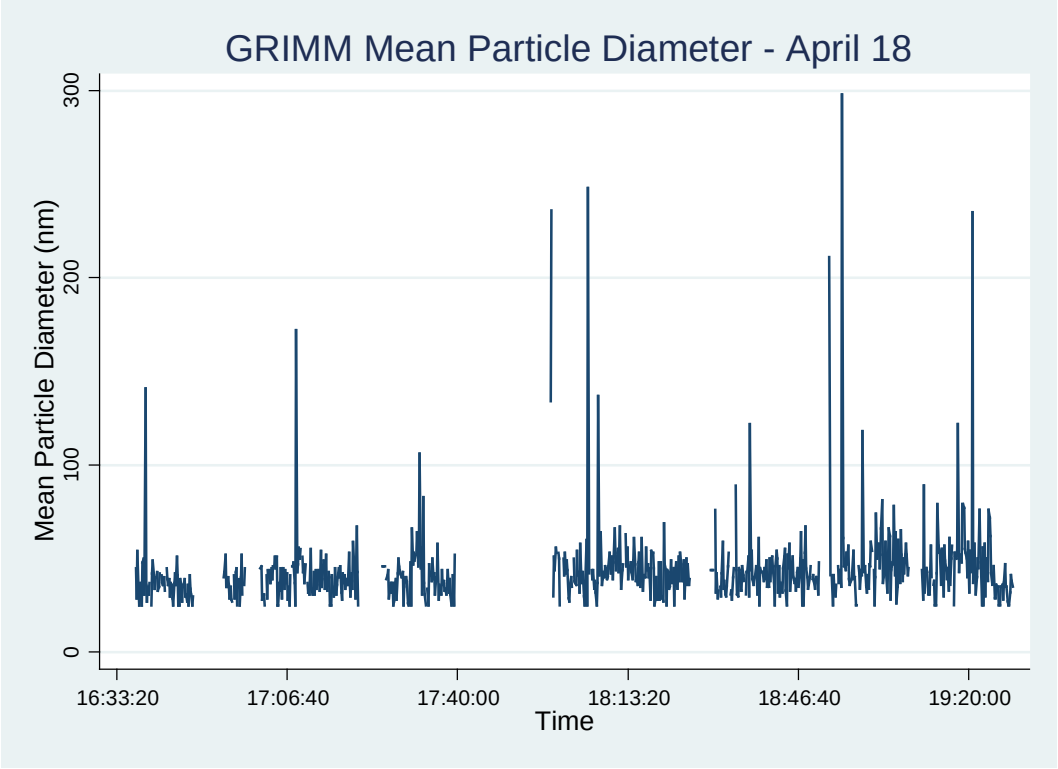

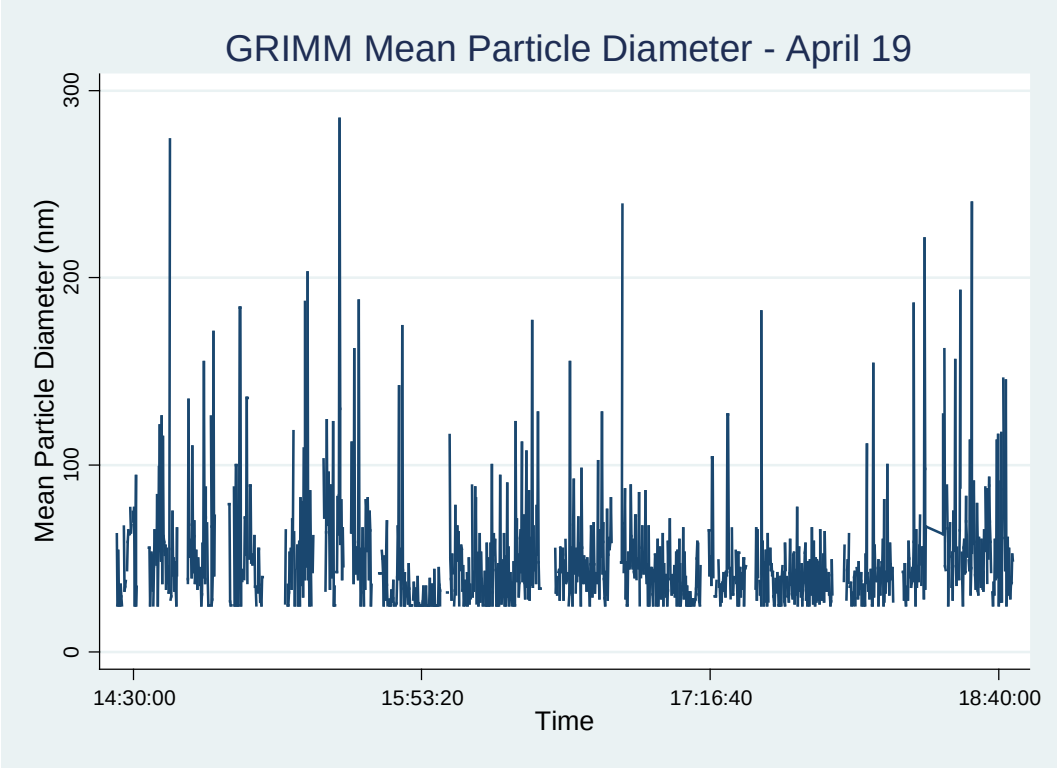

Appendix A7- Time-Series Plots of the Entire Mobile Monitoring Campaign for Each Sampling Day

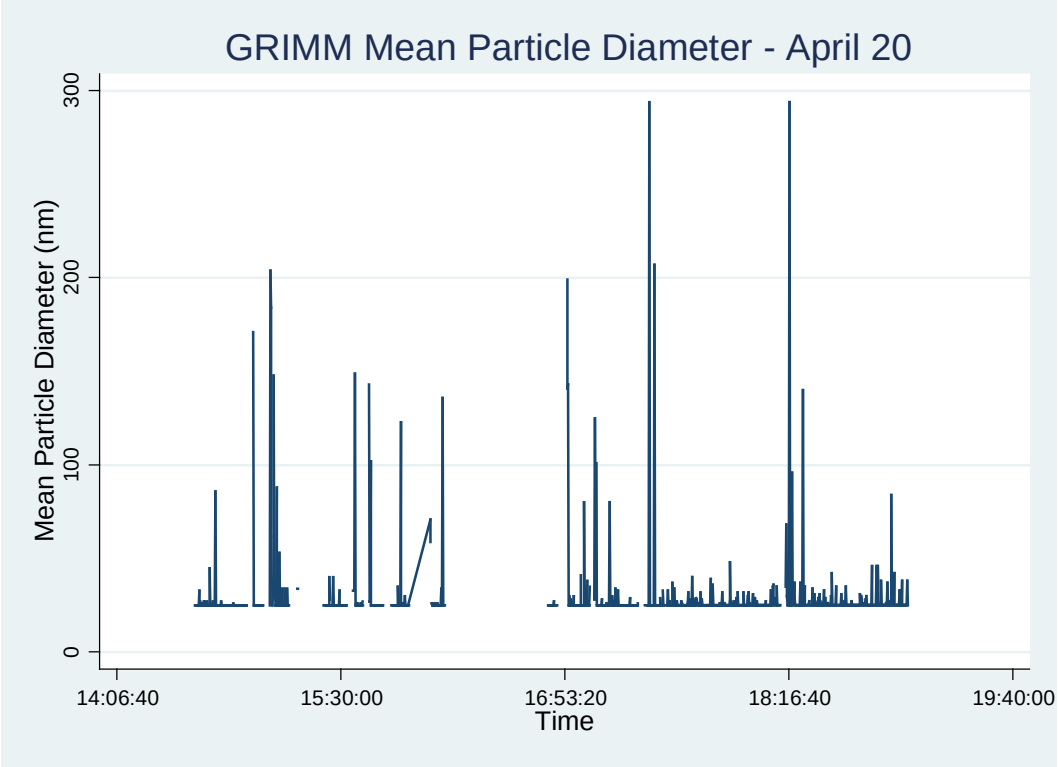

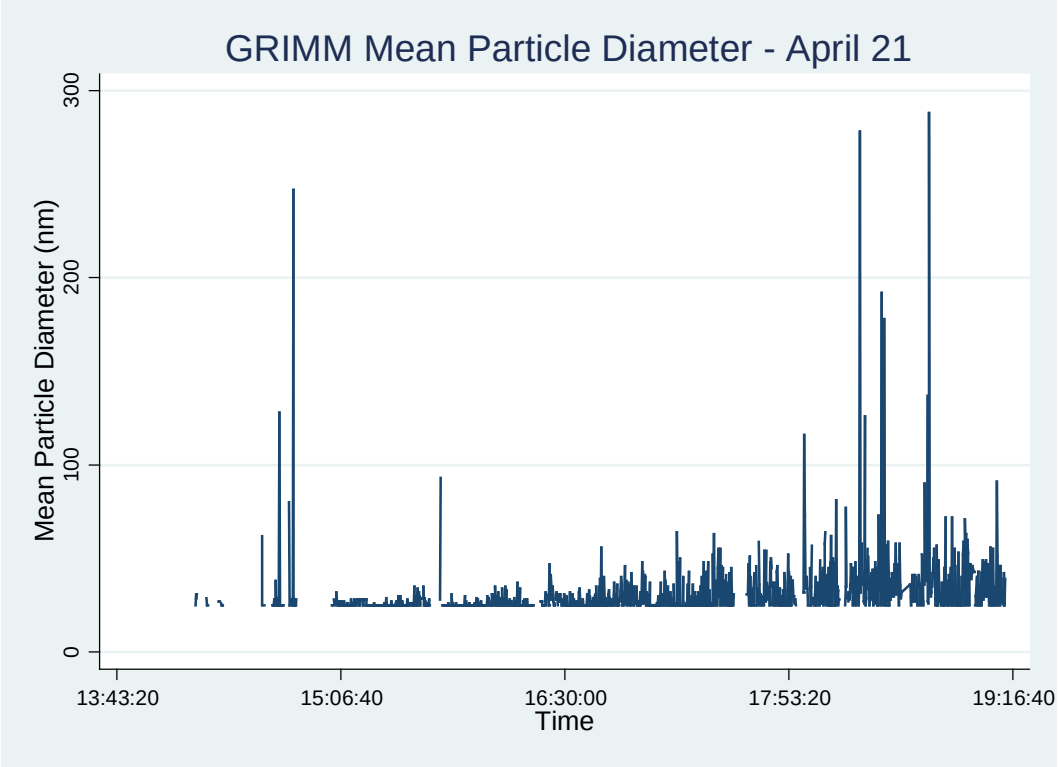

Appendix A7- Time-Series Plots of the Entire Mobile Monitoring Campaign for Each Sampling Day

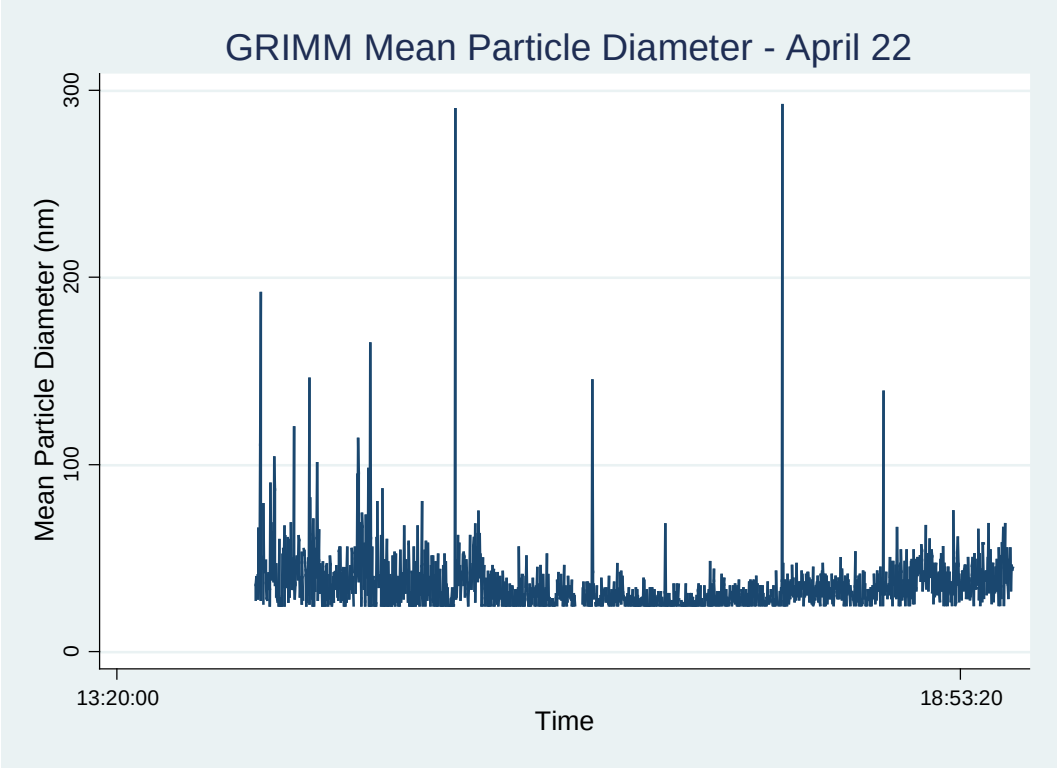

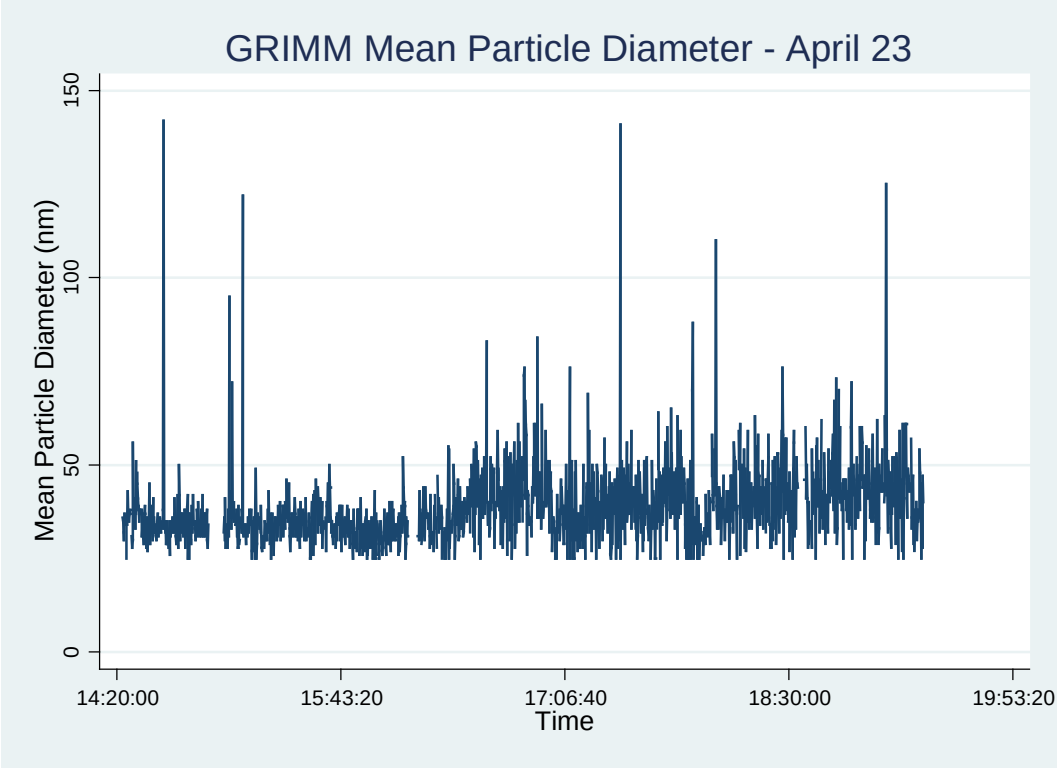

Appendix A7- Time-Series Plots of the Entire Mobile Monitoring Campaign for Each Sampling Day

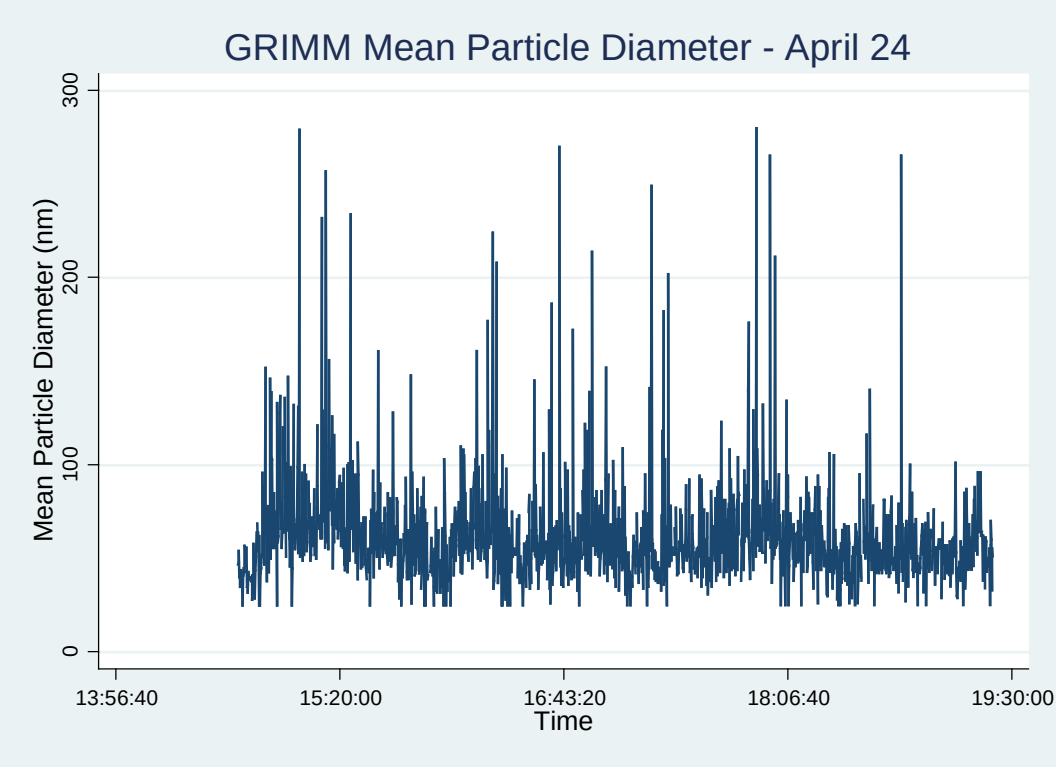

Appendix A8 - Time-Series Plots of the Entire Mobile Monitoring Campaign for Each Sampling Day

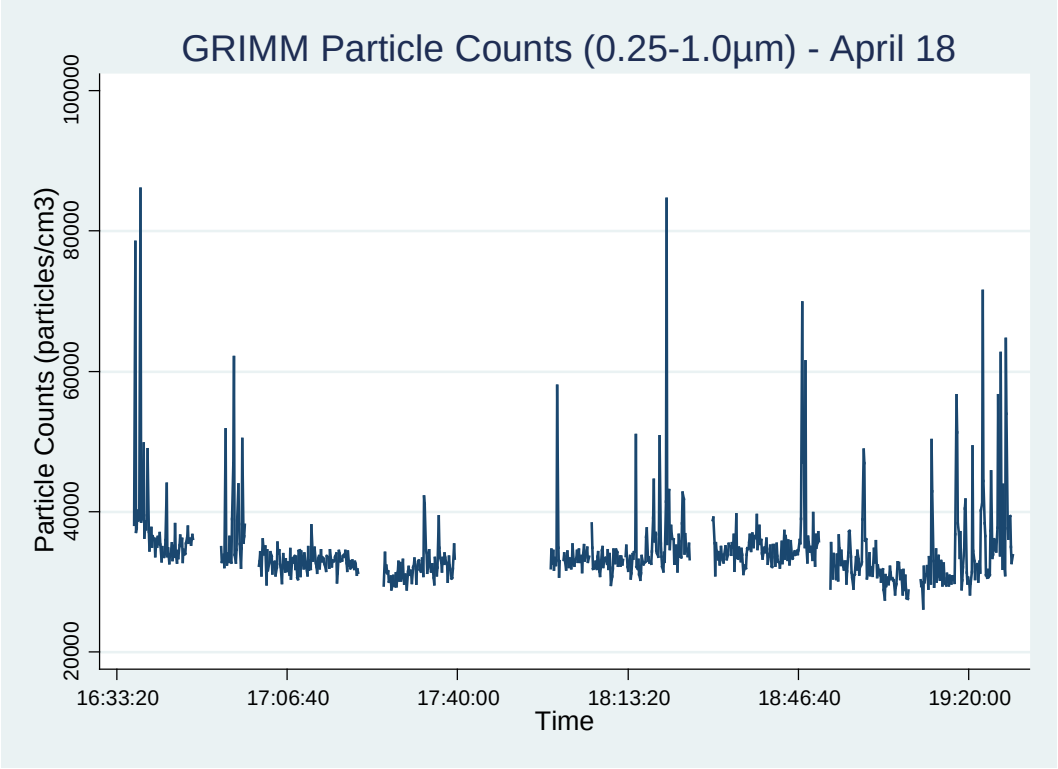

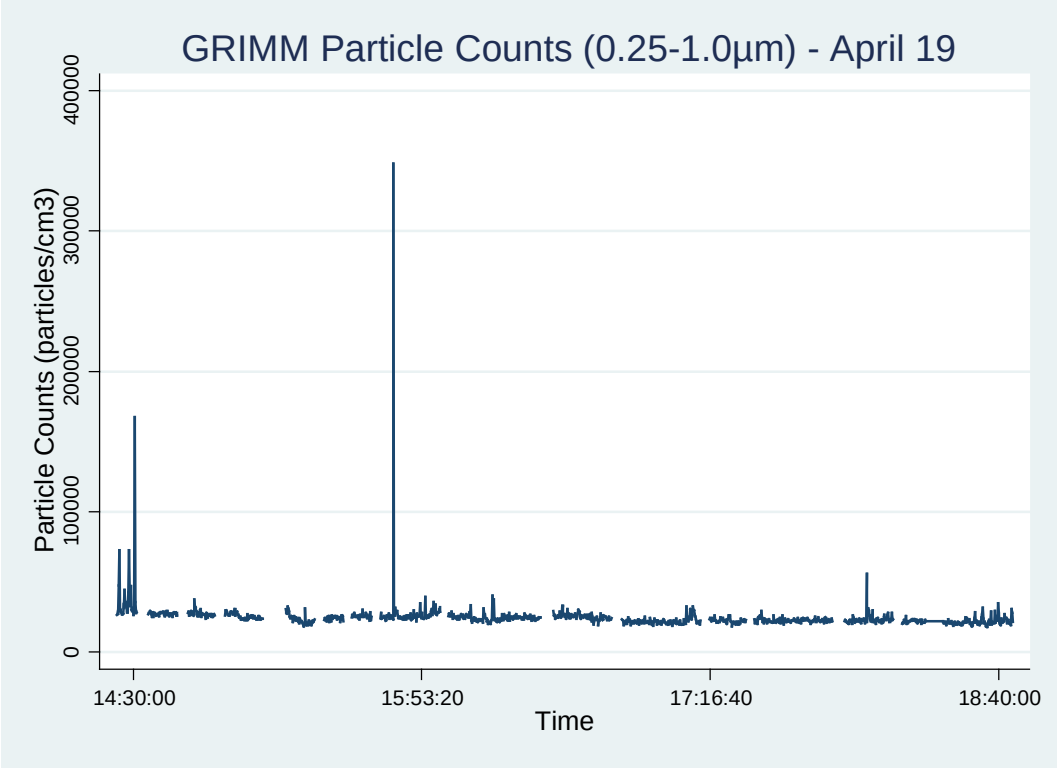

Appendix A8 - Time-Series Plots of the Entire Mobile Monitoring Campaign for Each Sampling Day

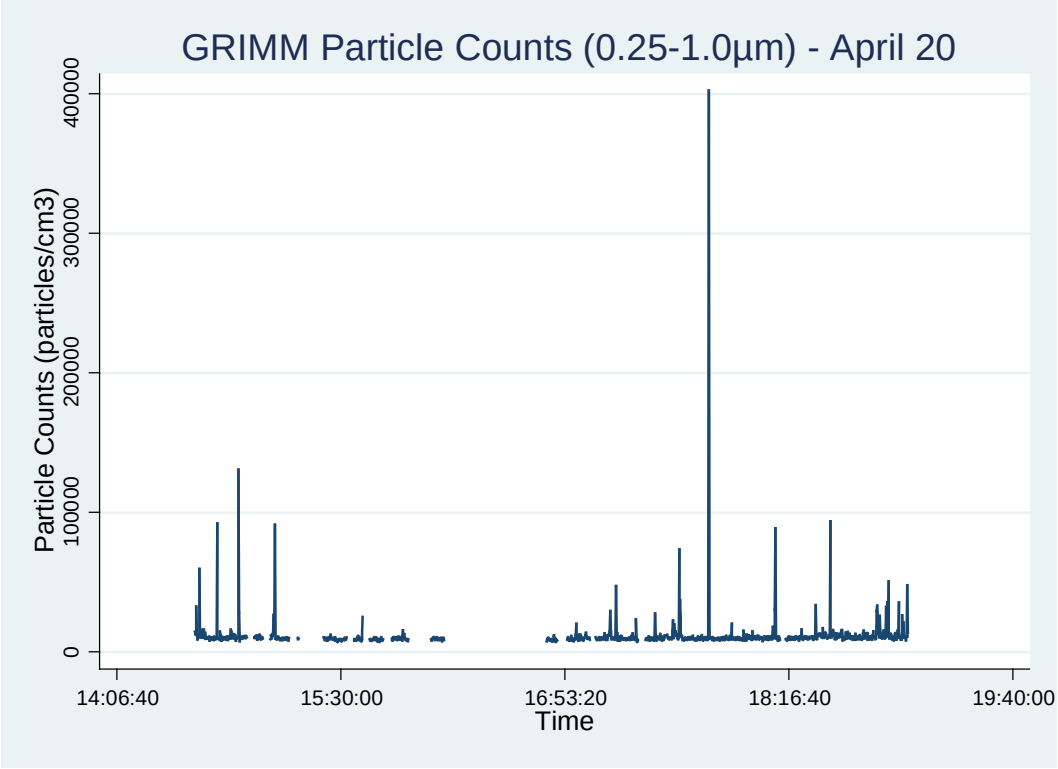

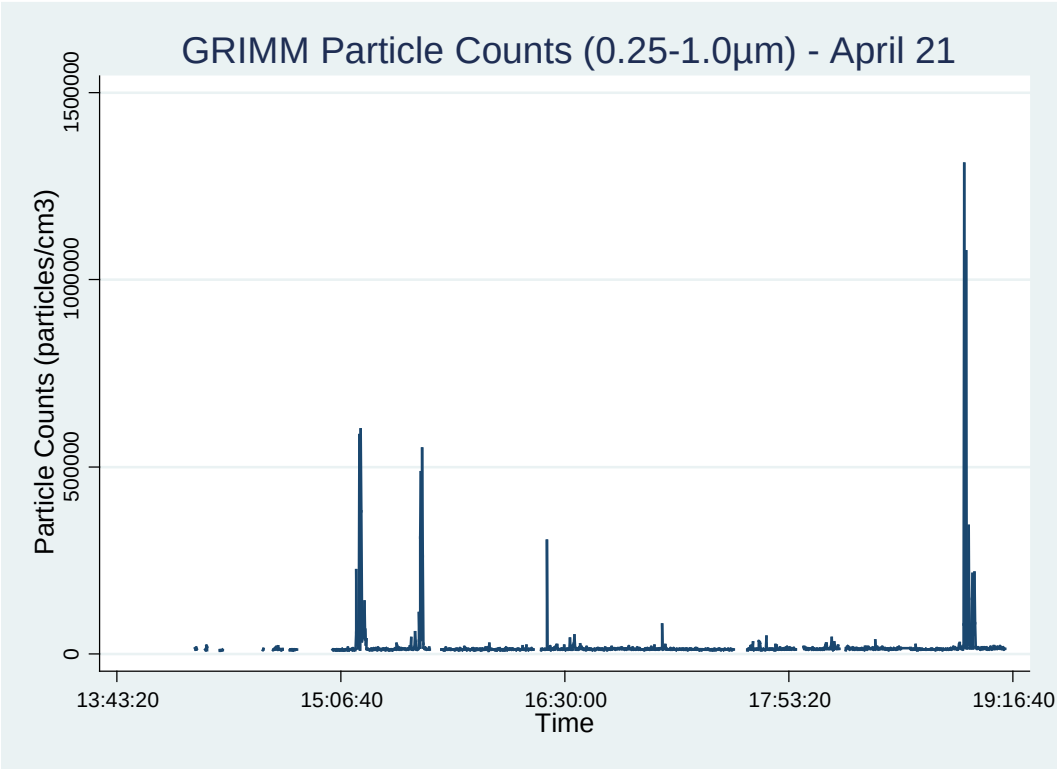

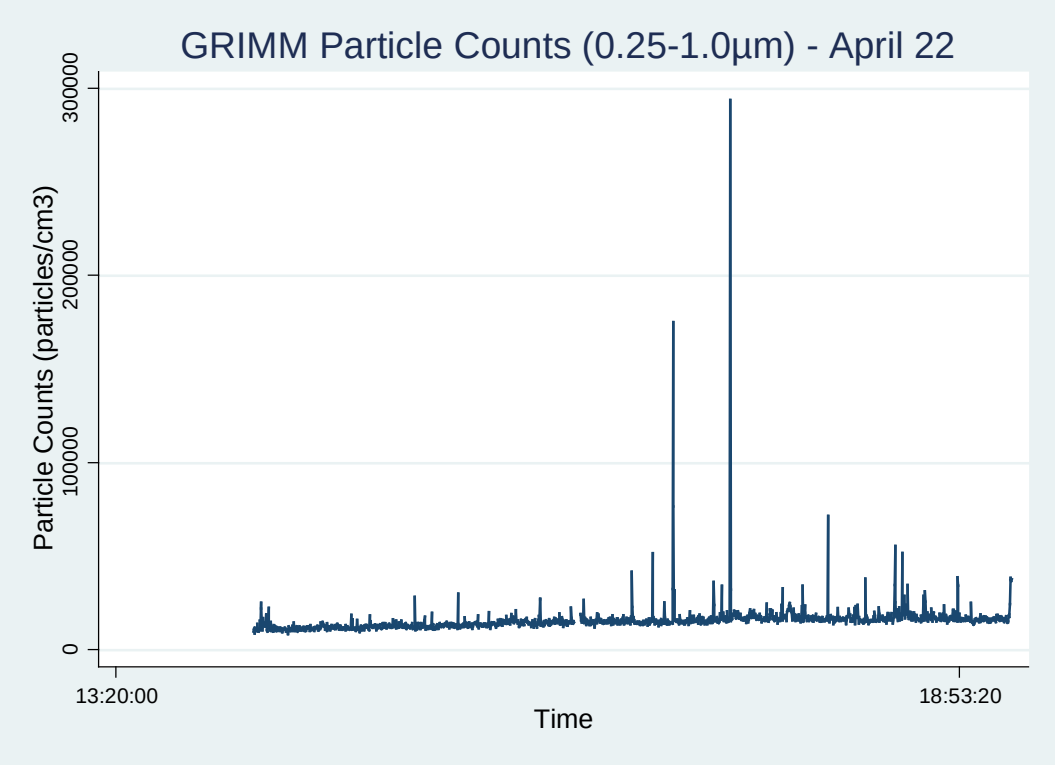
GRIMM Particle Counts (0.25-1.0µm) - April 22
Particle Counts (particles/cm3)
0
100000
200000
300000
13:20:00
18:53:20
Time

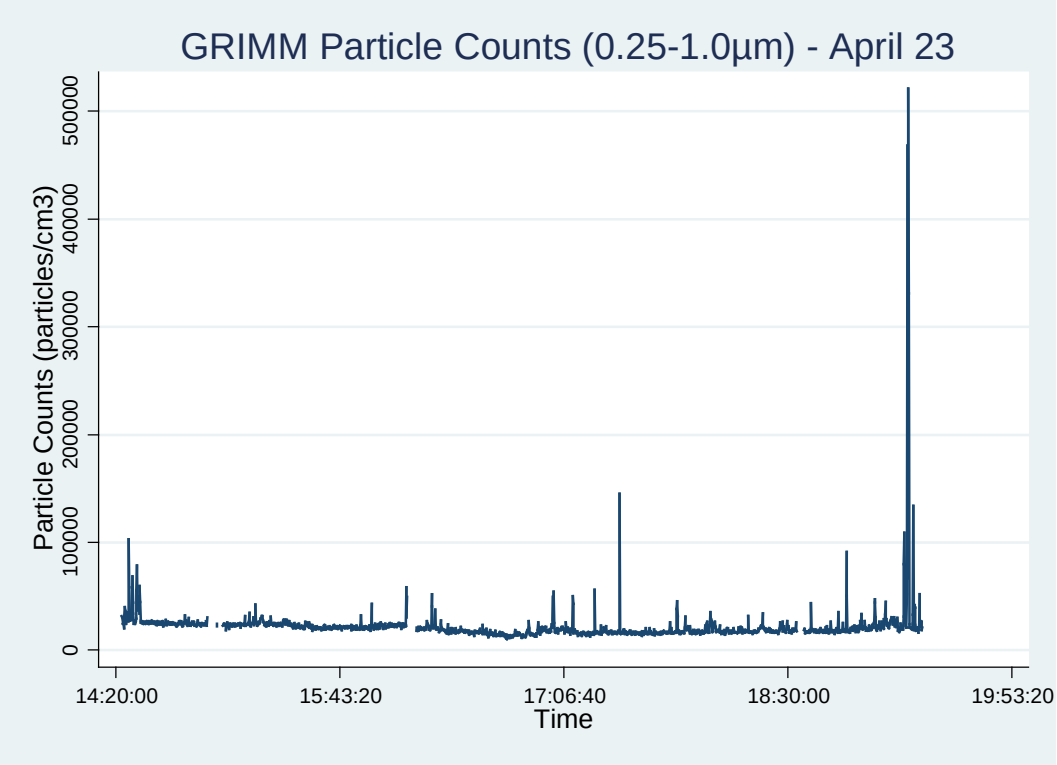
GRIMM Particle Counts (0.25-1.0µm) - April 23
Particle Counts (particles/cm3)
0
100000
200000
300000
400000
500000
14:20:00
15:43:20
17:06:40
18:30:00
19:53:20
Time

Appendix A8 - Time-Series Plots of the Entire Mobile Monitoring Campaign for Each Sampling Day

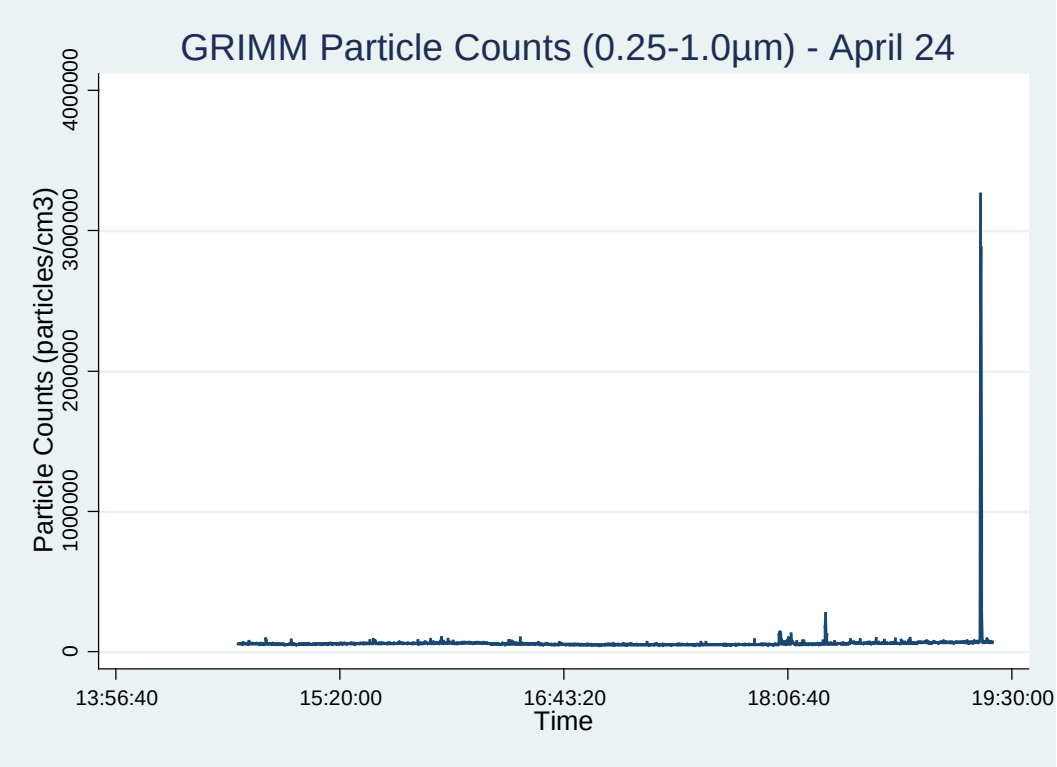

Appendix A9 - Time-Series Plots of the Entire Mobile Monitoring Campaign for Each Sampling Day

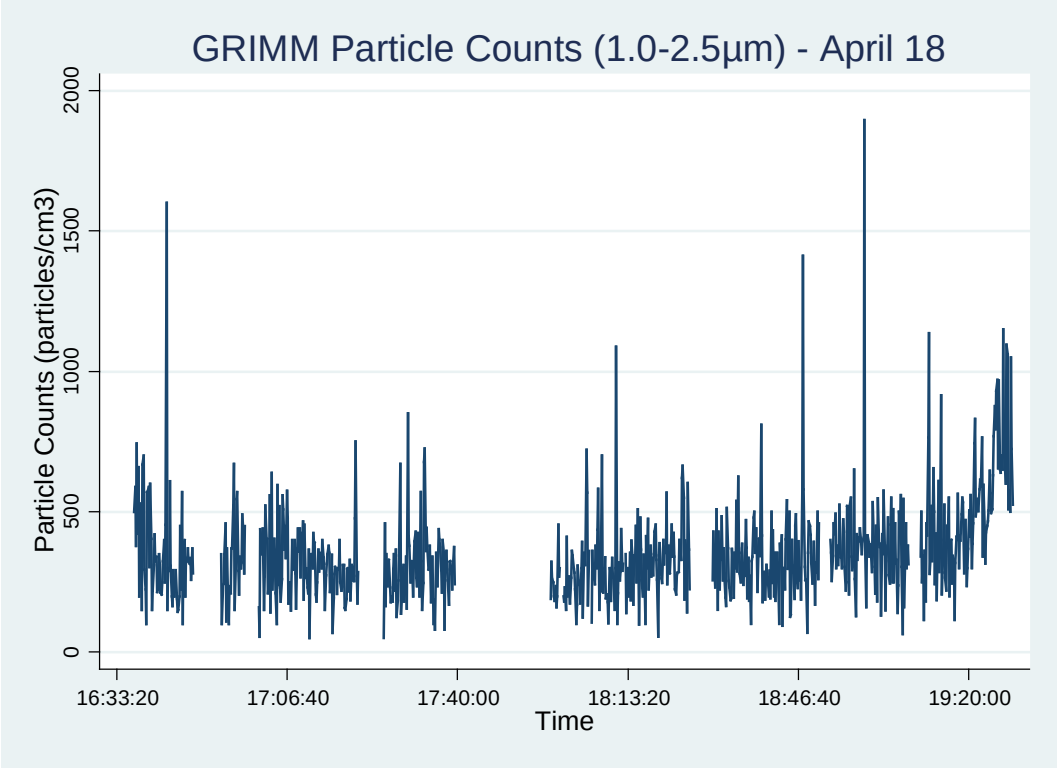

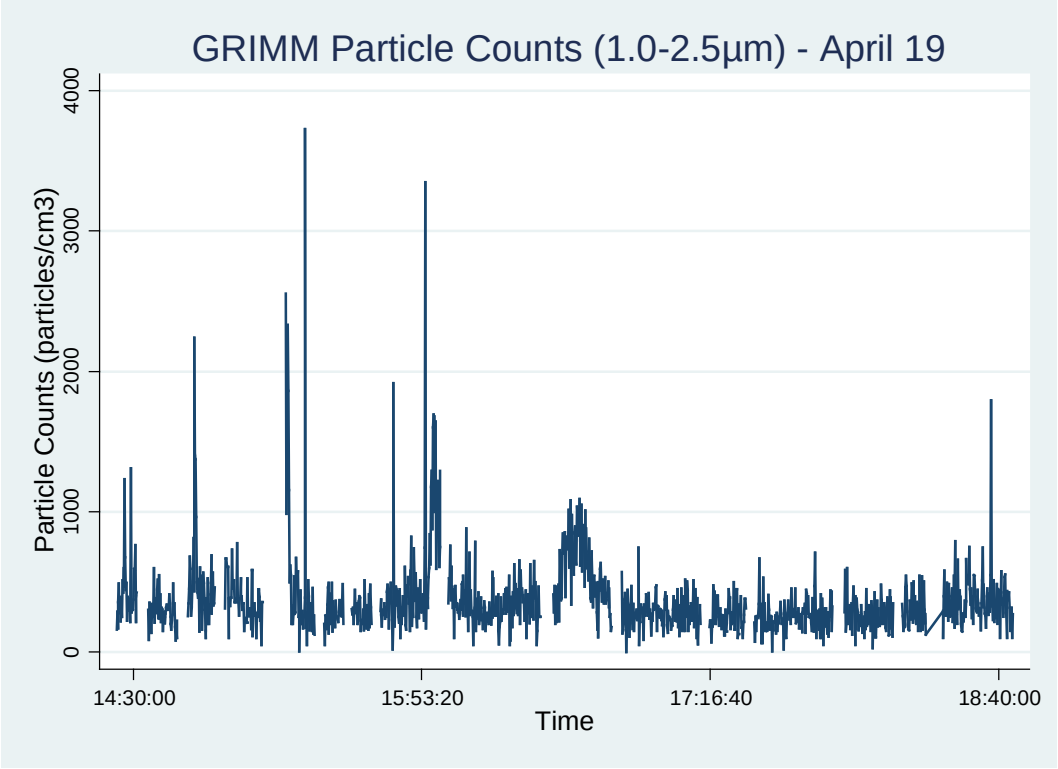

Appendix A9 - Time-Series Plots of the Entire Mobile Monitoring Campaign for Each Sampling Day

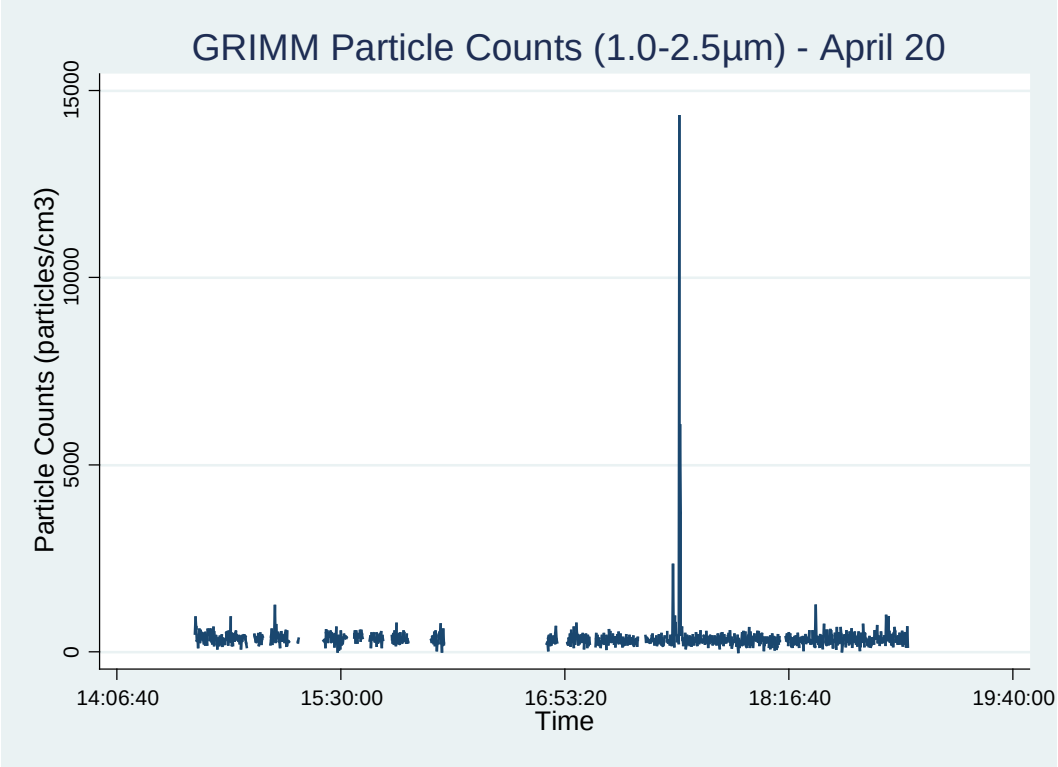

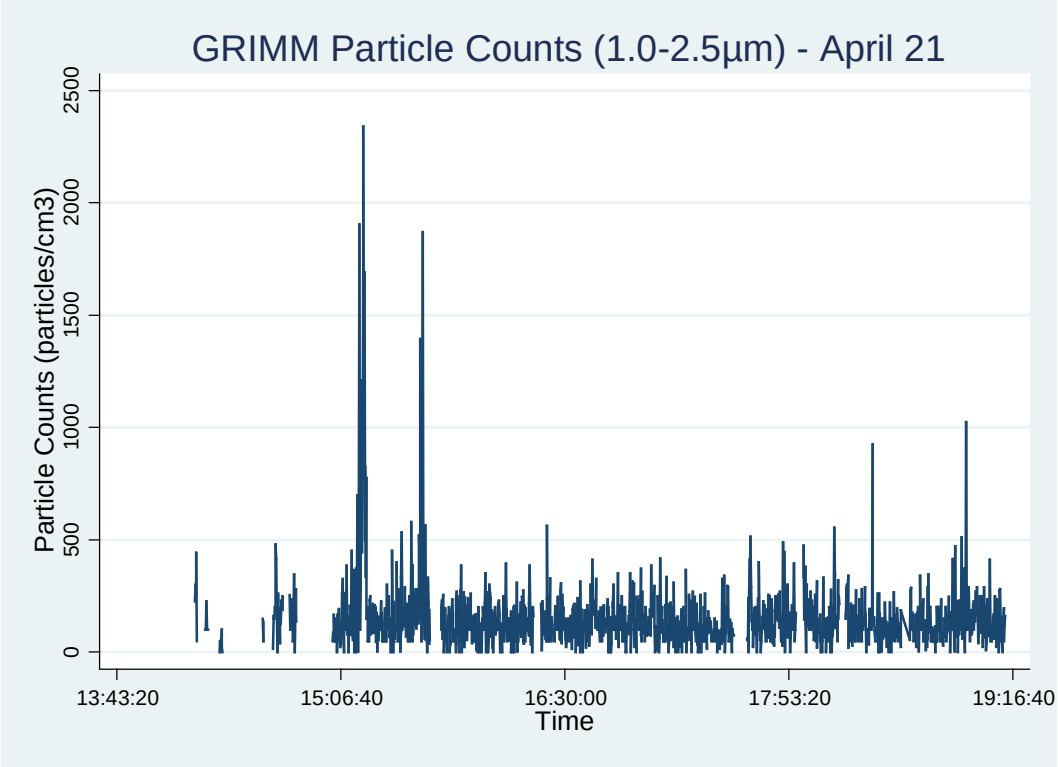

Appendix A9 - Time-Series Plots of the Entire Mobile Monitoring Campaign for Each Sampling Day

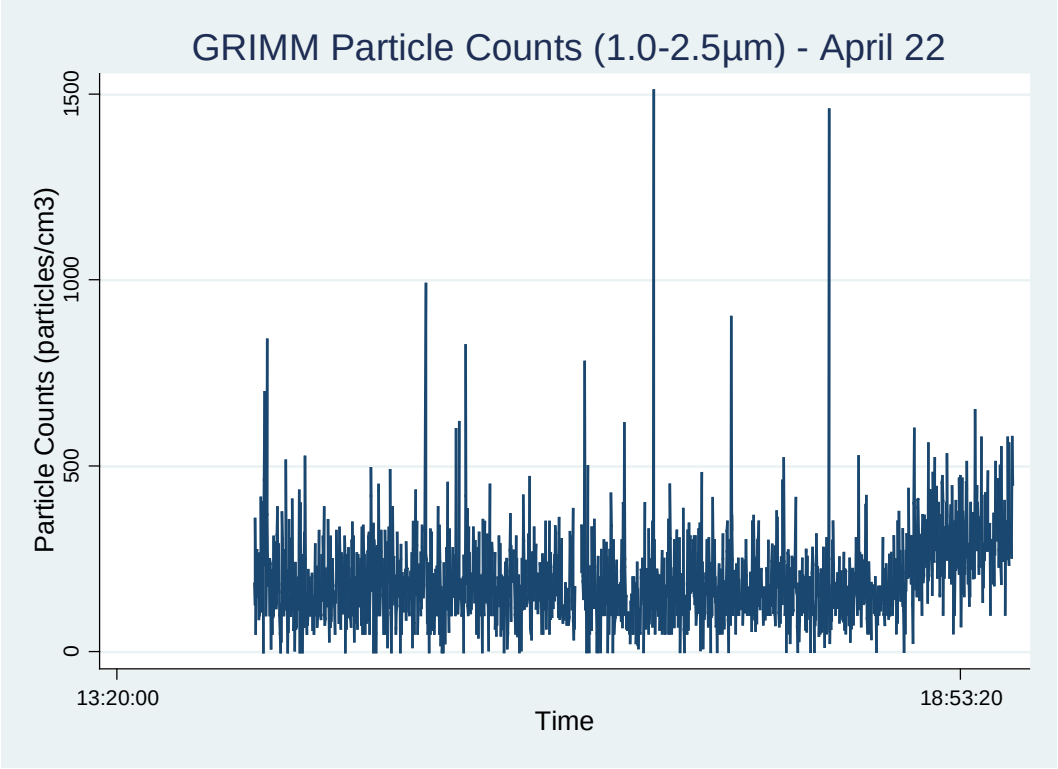

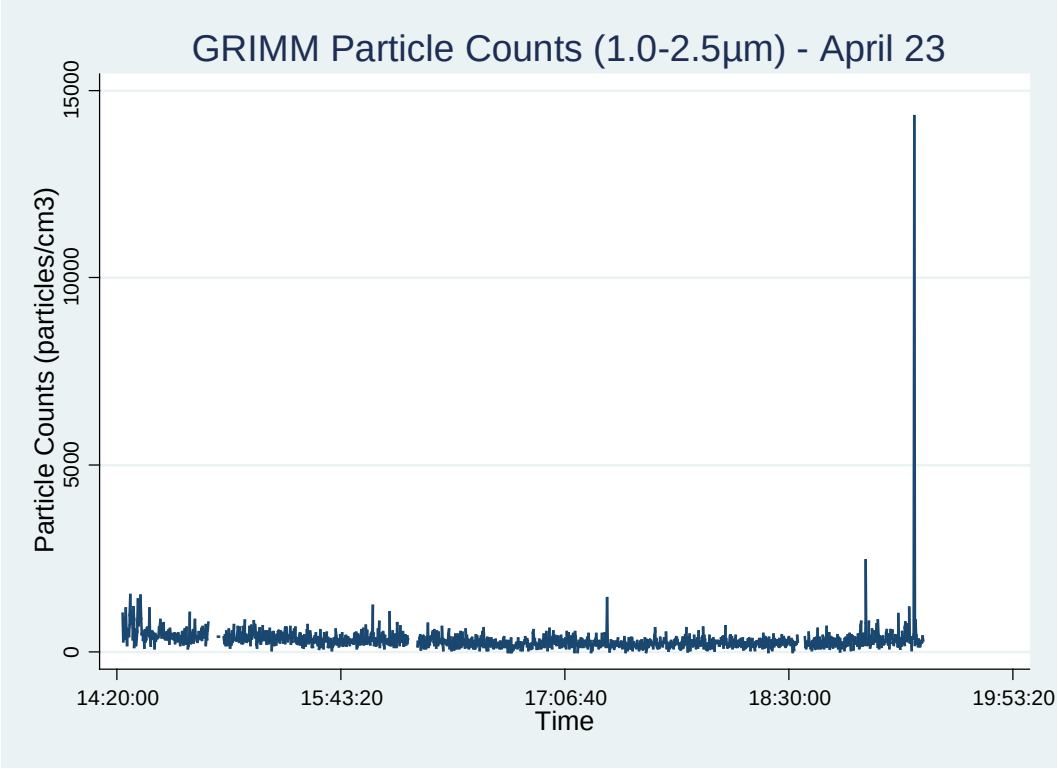

Appendix A9 - Time-Series Plots of the Entire Mobile Monitoring Campaign for Each Sampling Day

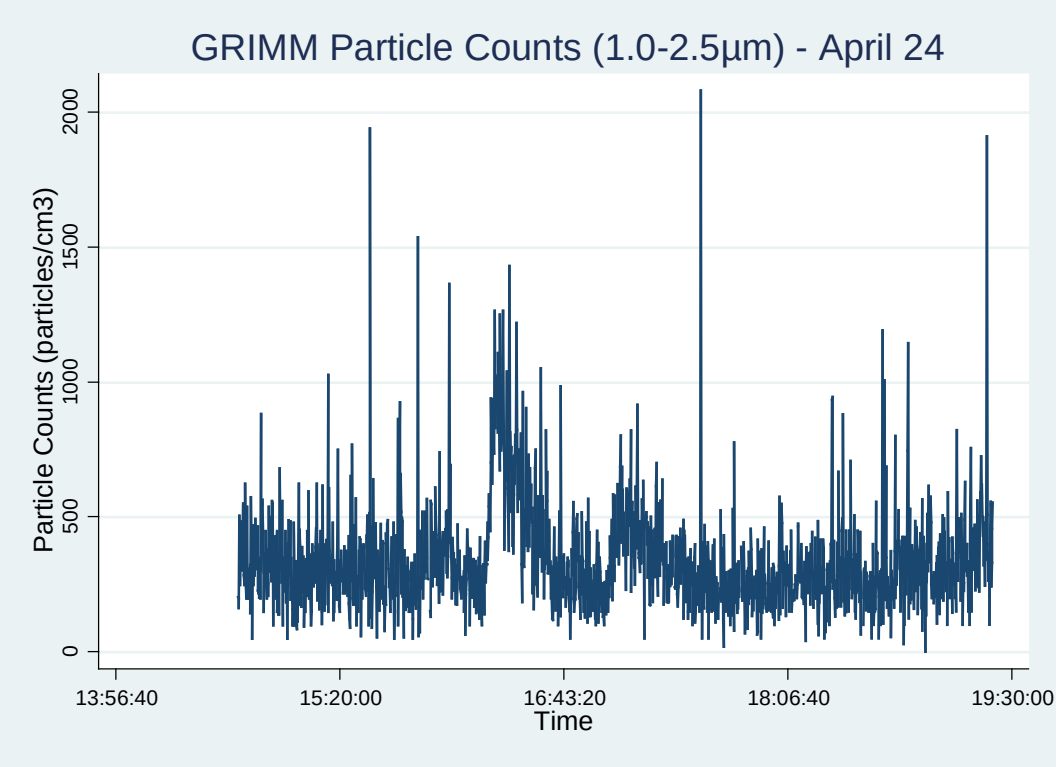

Appendix A10 - Time-Series Plots of the Entire Mobile Monitoring Campaign for Each Sampling Day

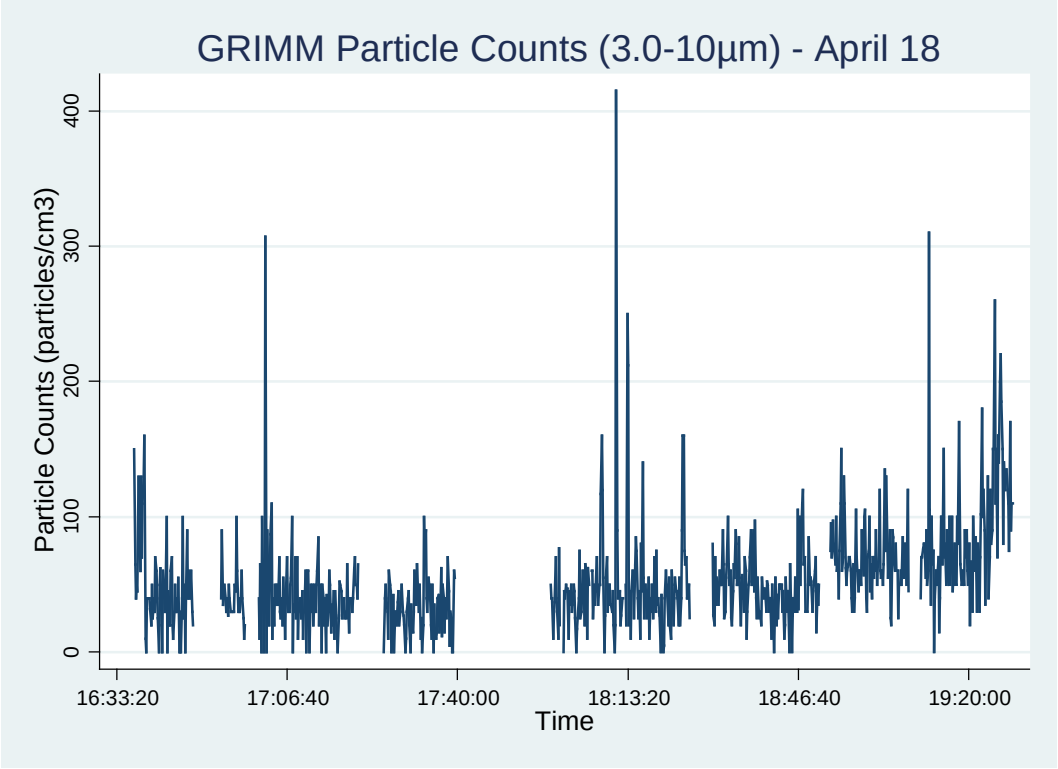

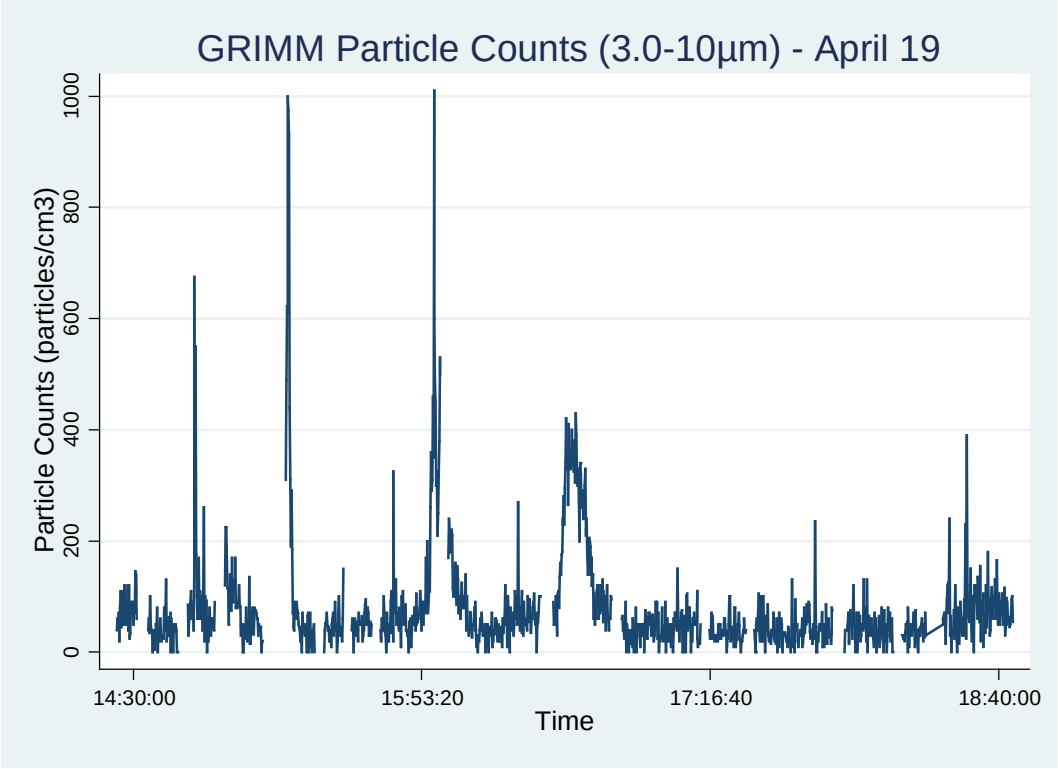

Appendix A10 - Time-Series Plots of the Entire Mobile Monitoring Campaign for Each Sampling Day

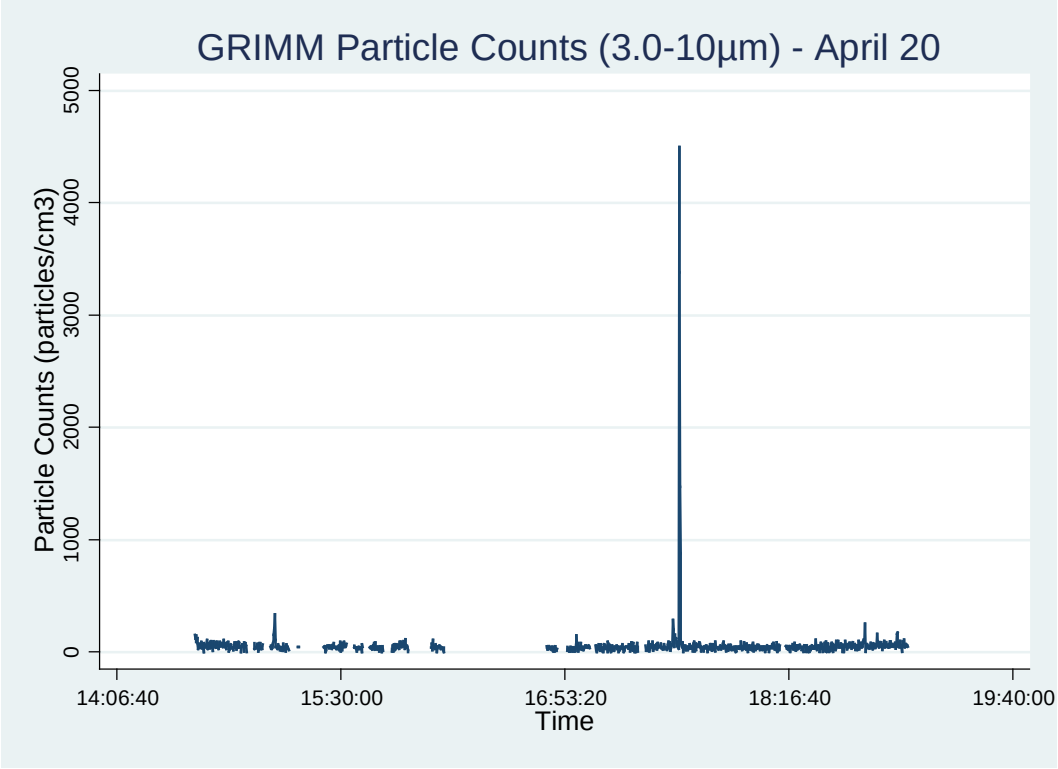

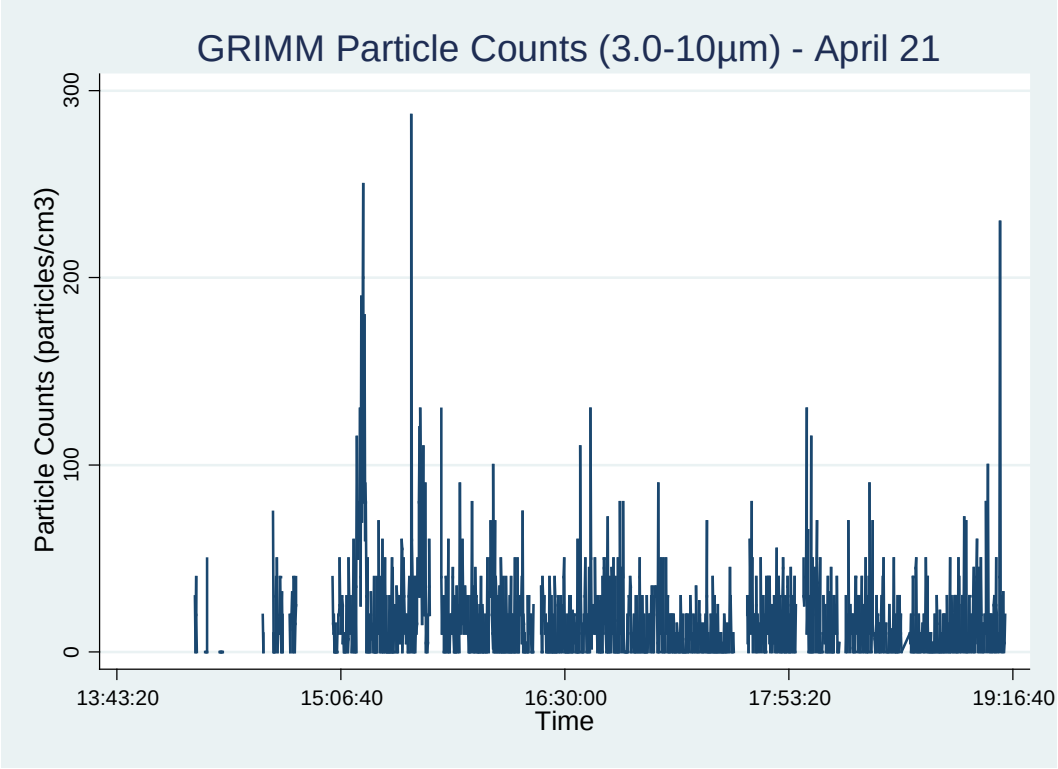

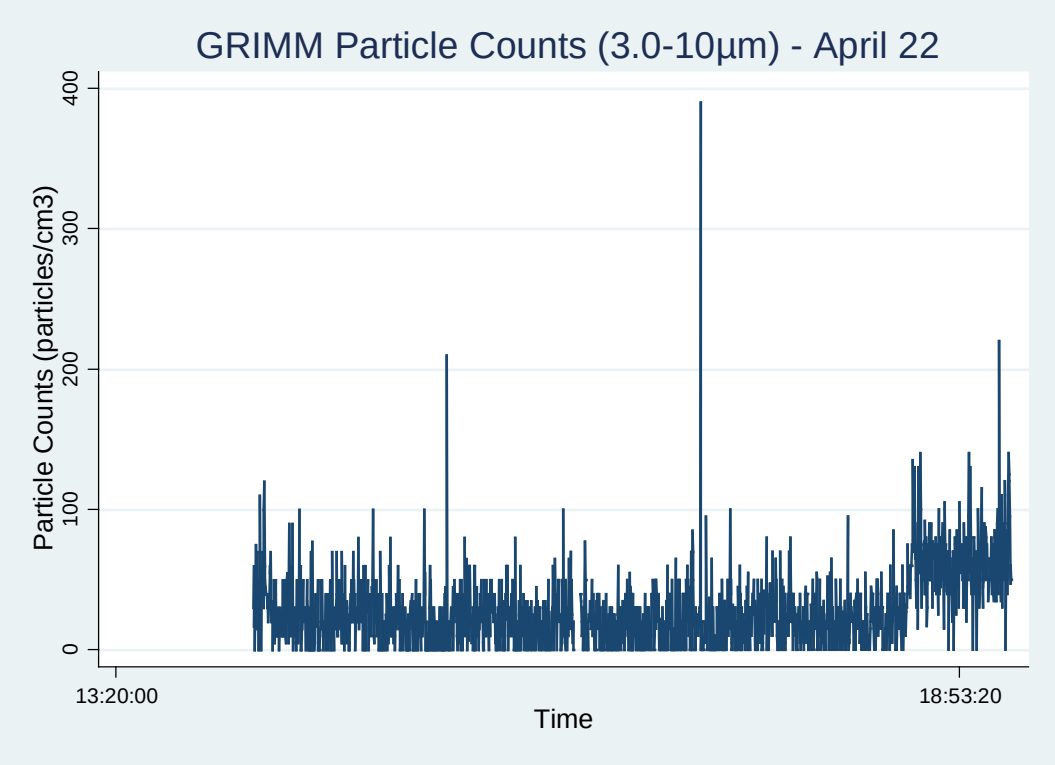
GRIMM Particle Counts (3.0-10µm) - April 22
Particle Counts (particles/cm3)
0
100
200
300
400
13:20:00
18:53:20
Time

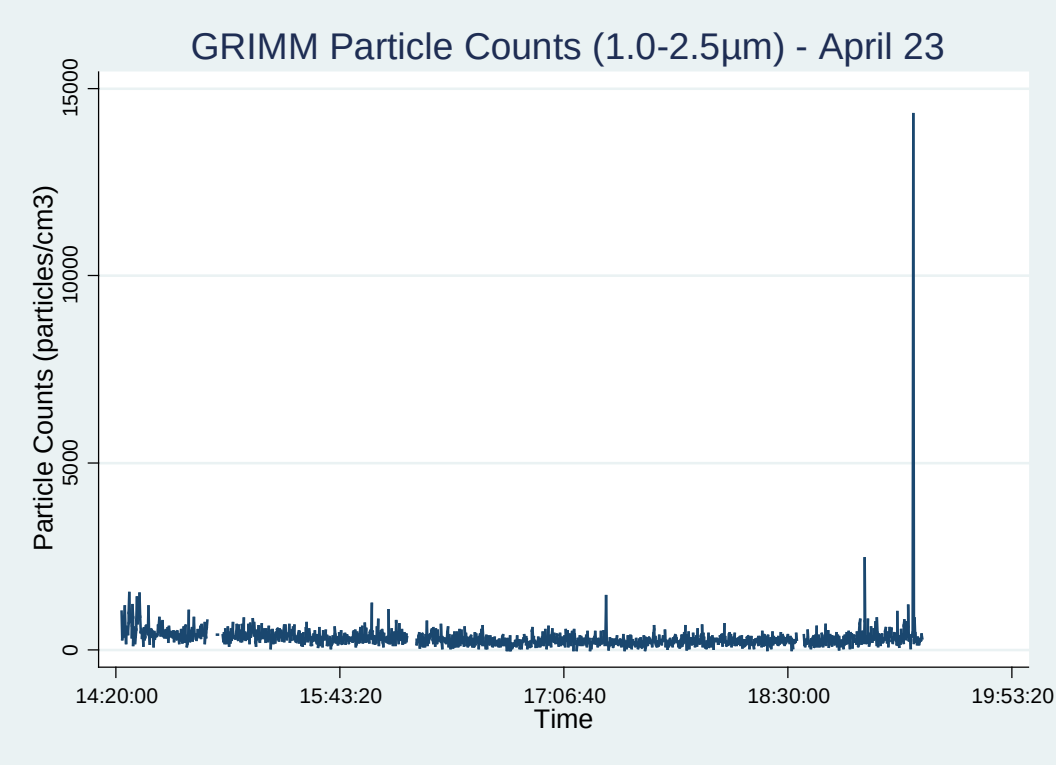
GRIMM Particle Counts (1.0-2.5µm) - April 23
Particle Counts (particles/cm3)
0
5000
10000
15000
14:20:00
15:43:20
17:06:40
18:30:00
19:53:20
Time

Appendix A10 - Time-Series Plots of the Entire Mobile Monitoring Campaign for Each Sampling Day

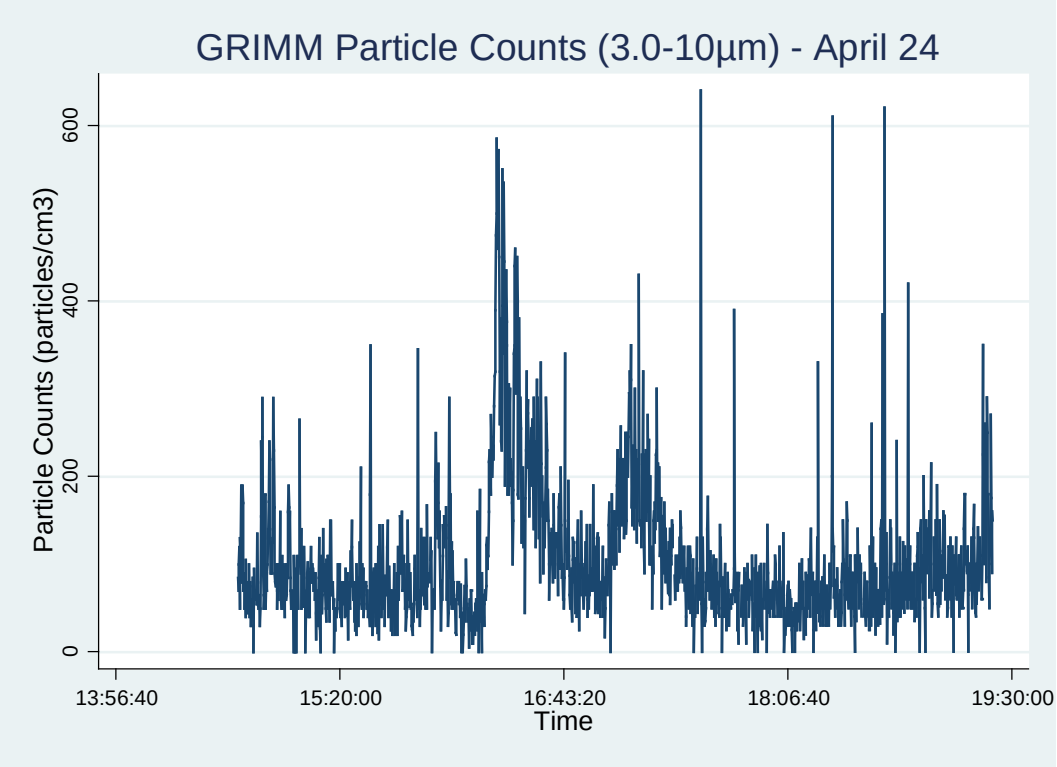

Appendix A11 - Time-Series Plots of the Entire Mobile Monitoring Campaign for Each Sampling Day

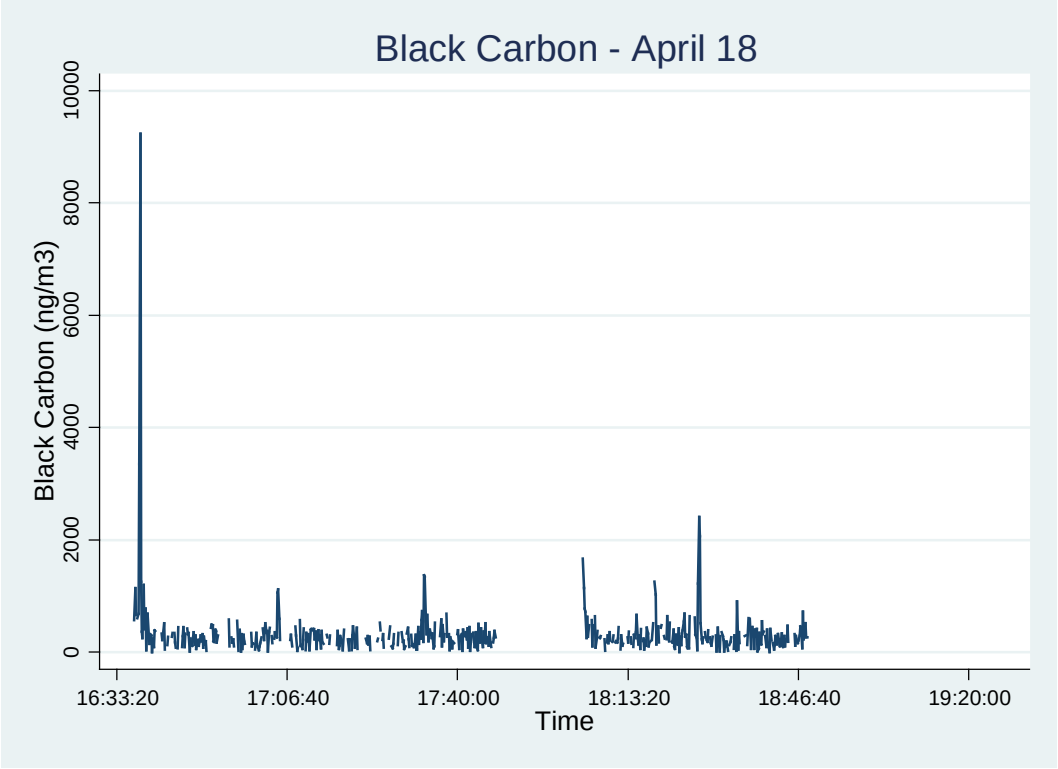

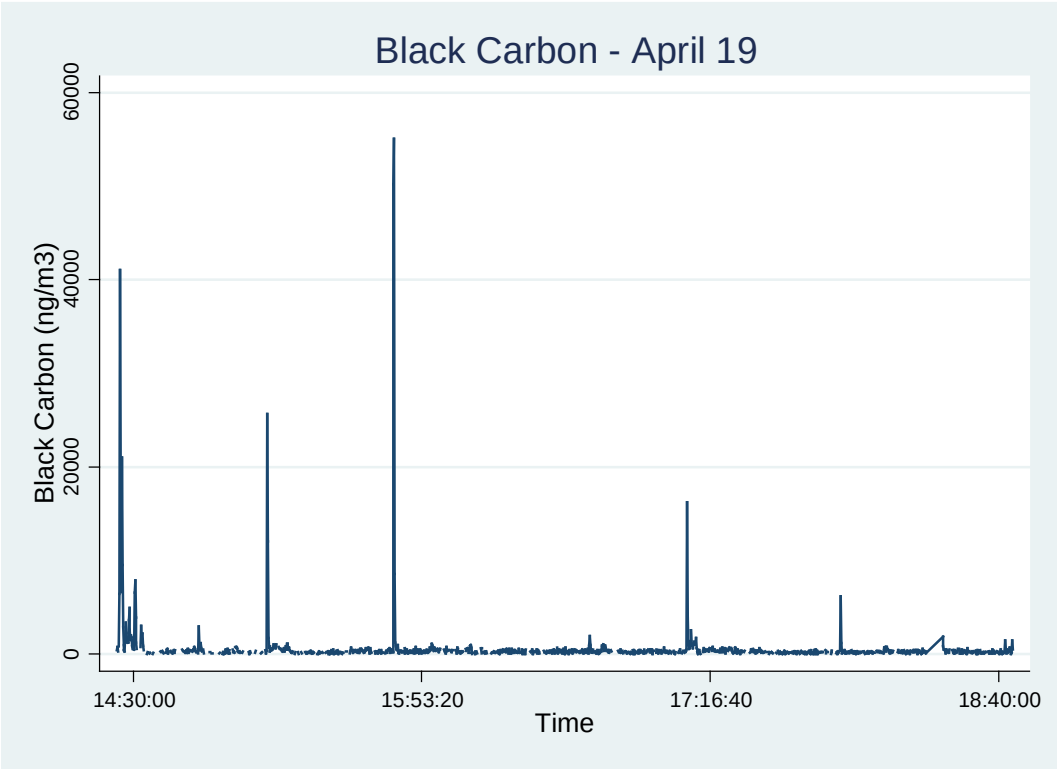

Appendix A11 - Time-Series Plots of the Entire Mobile Monitoring Campaign for Each Sampling Day

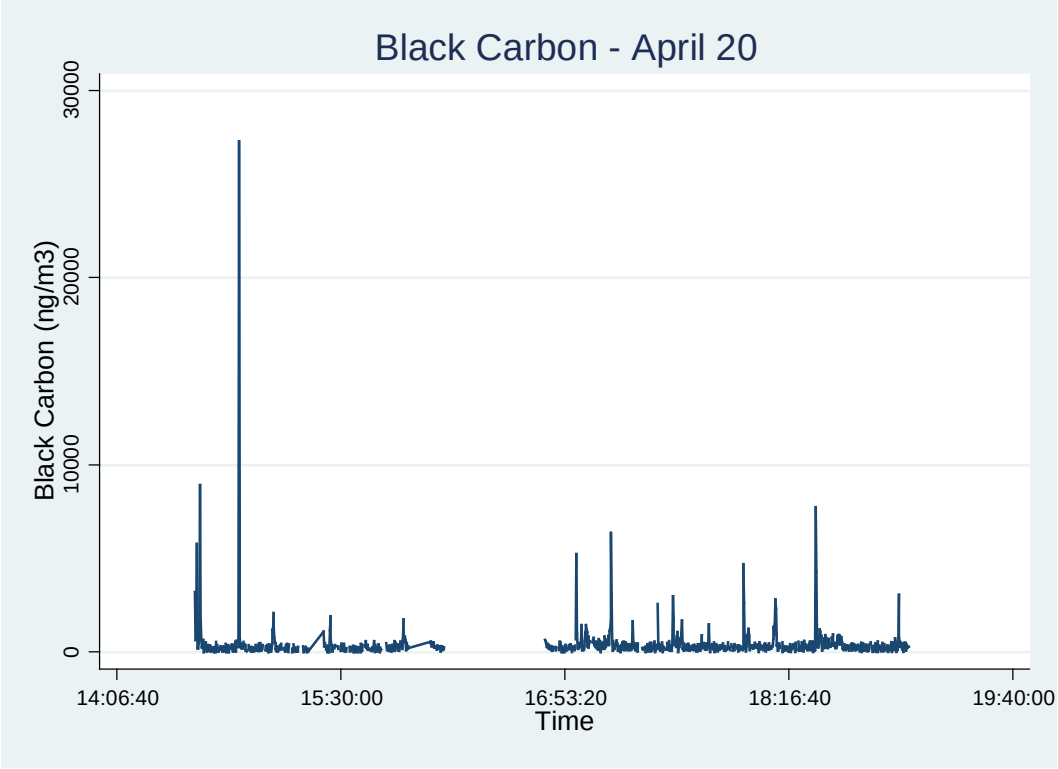

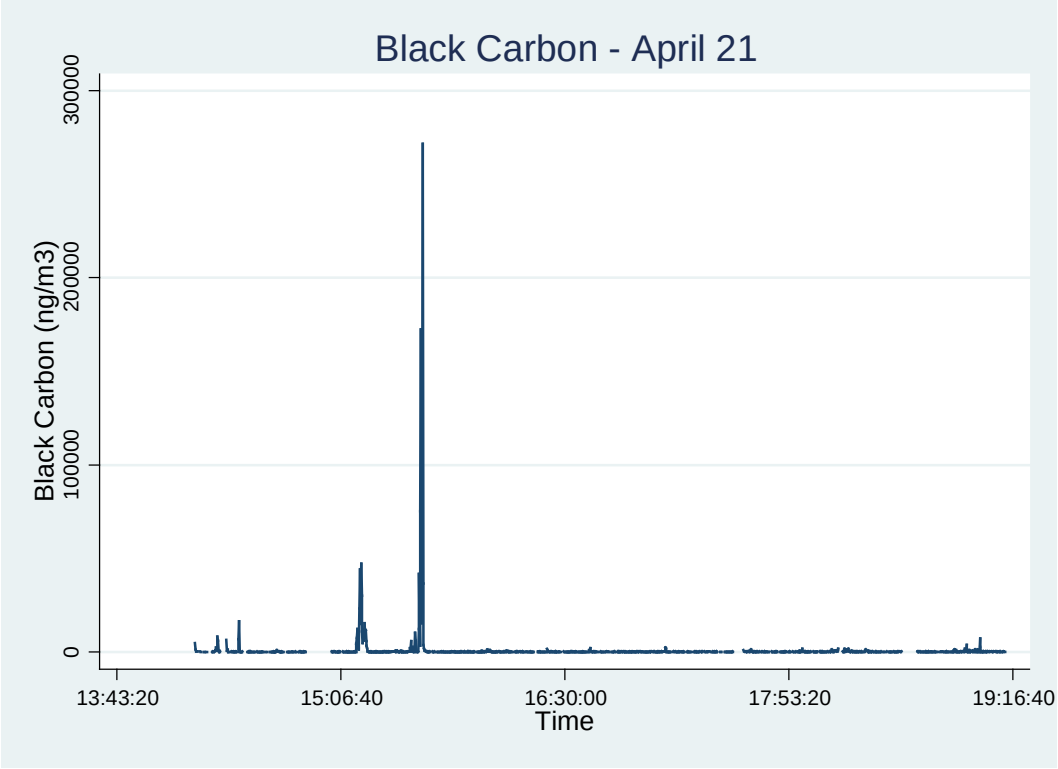

Appendix A11 - Time-Series Plots of the Entire Mobile Monitoring Campaign for Each Sampling Day

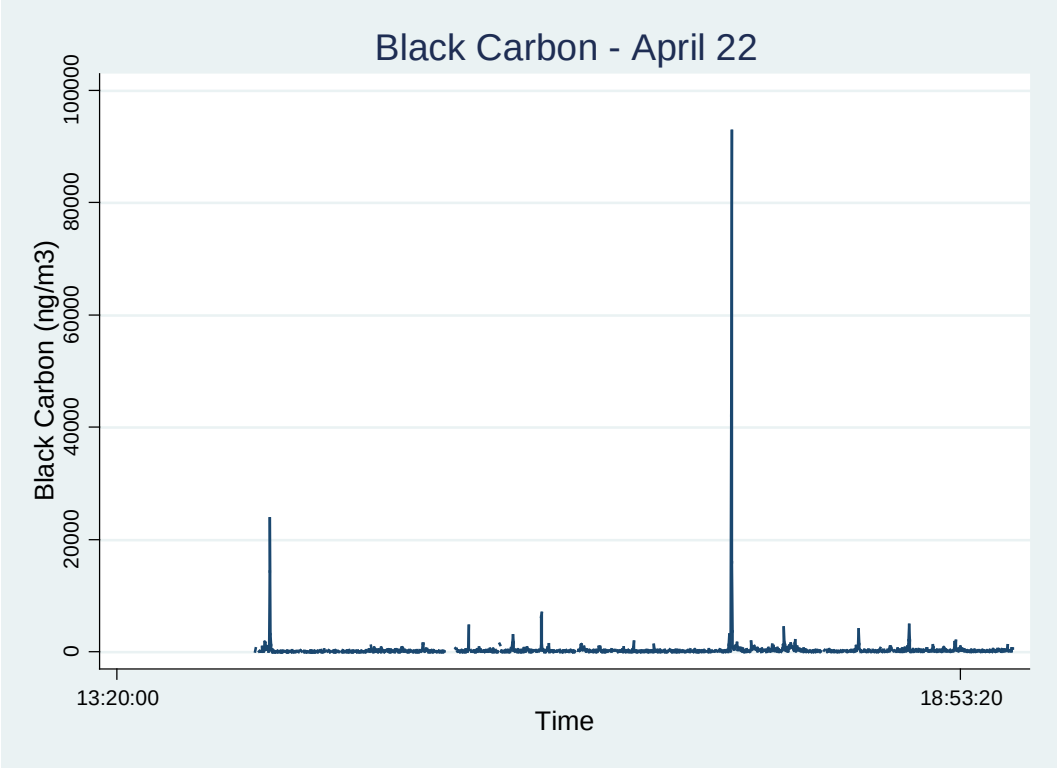

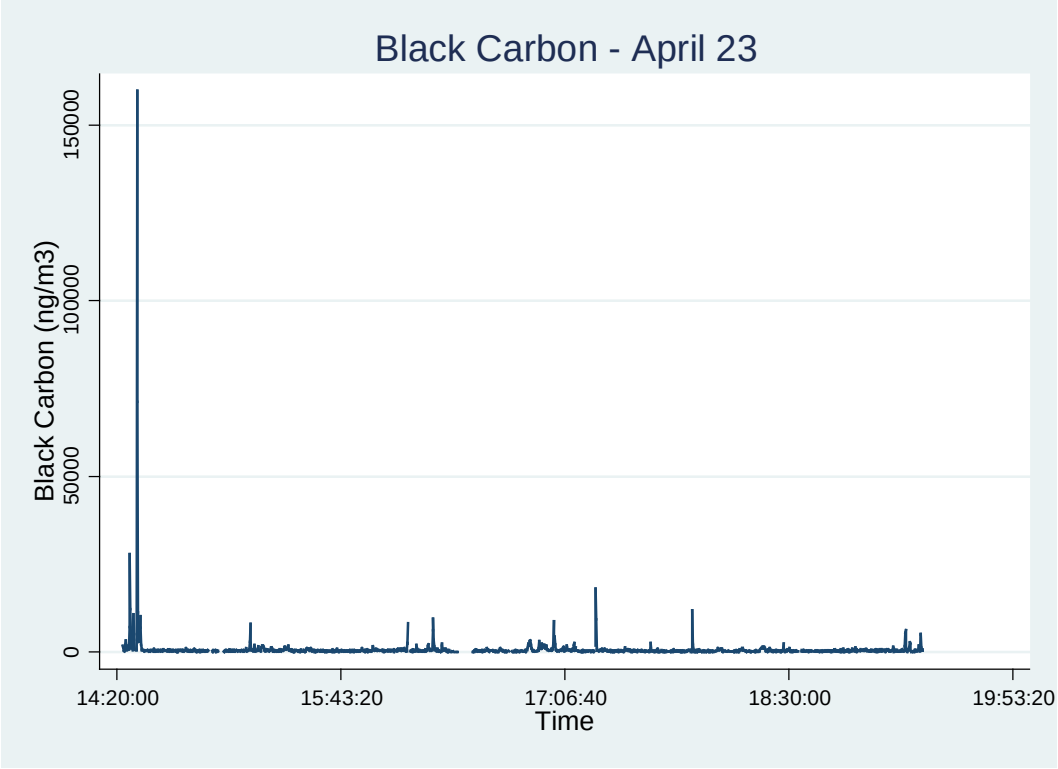

Appendix A11 - Time-Series Plots of the Entire Mobile Monitoring Campaign for Each Sampling Day

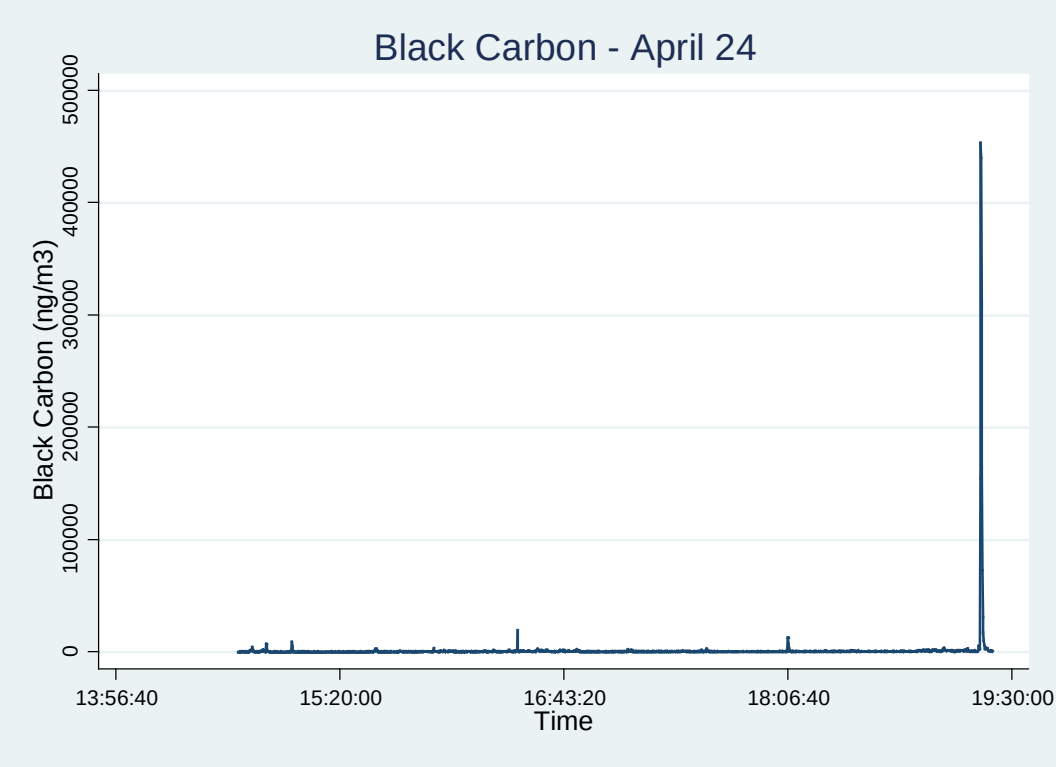

Appendix A12 - Time-Series Plots of the Entire Mobile Monitoring Campaign for Each Sampling Day

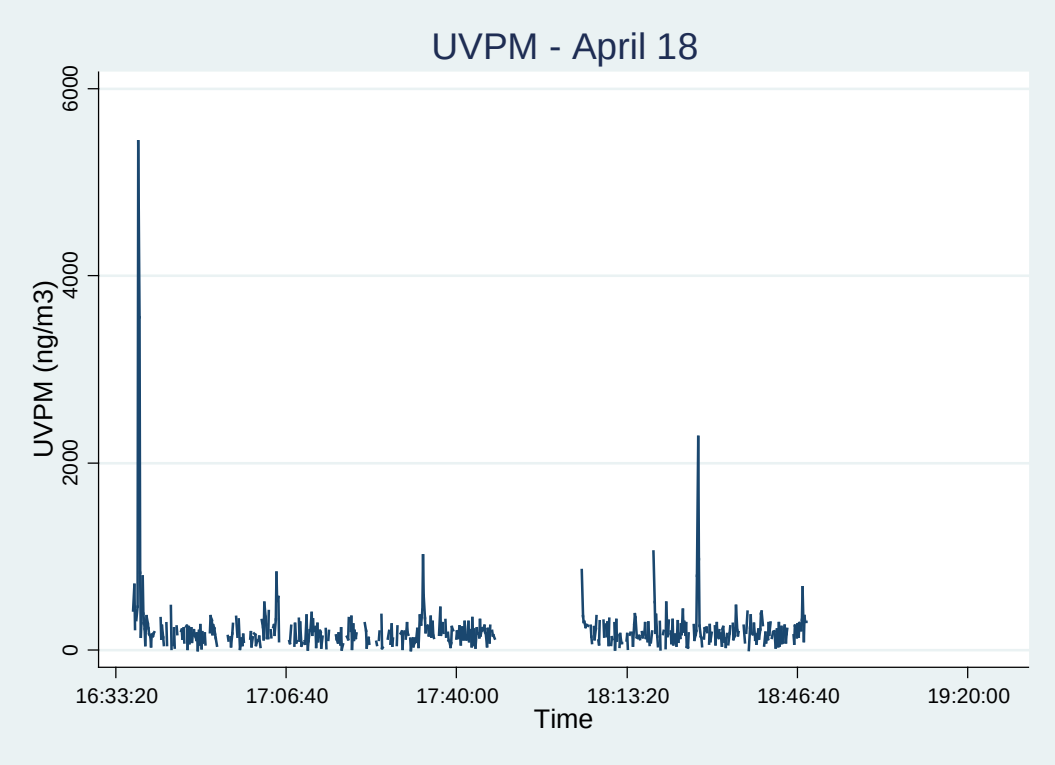

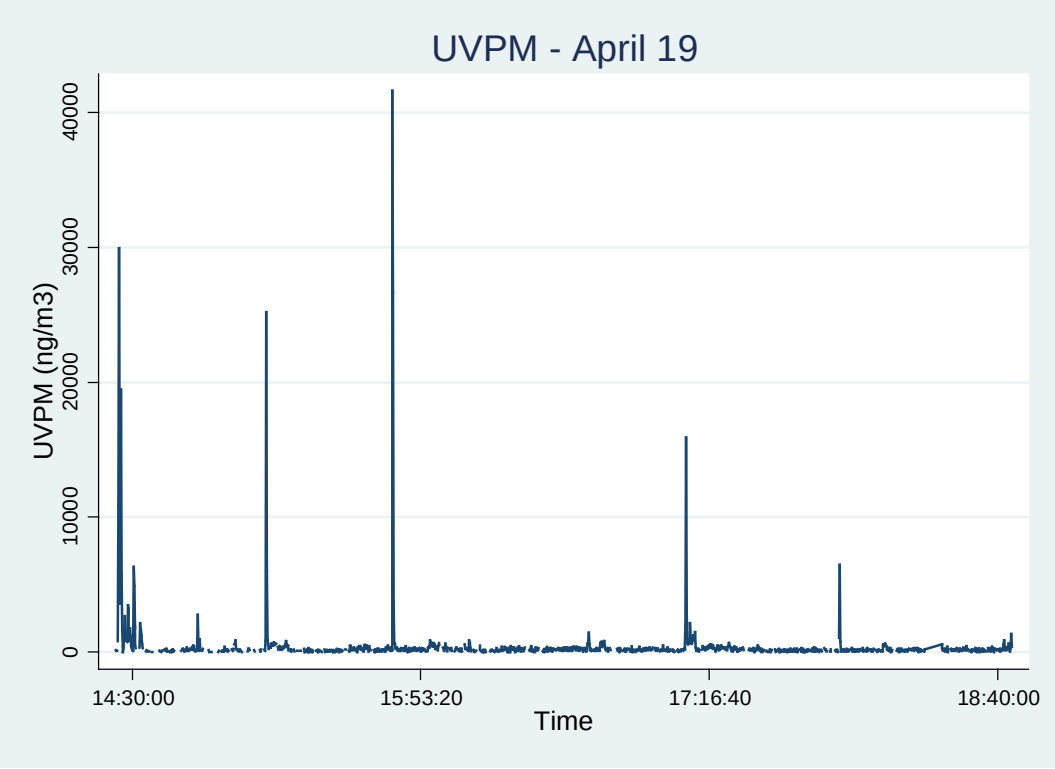

Appendix A12 - Time-Series Plots of the Entire Mobile Monitoring Campaign for Each Sampling Day

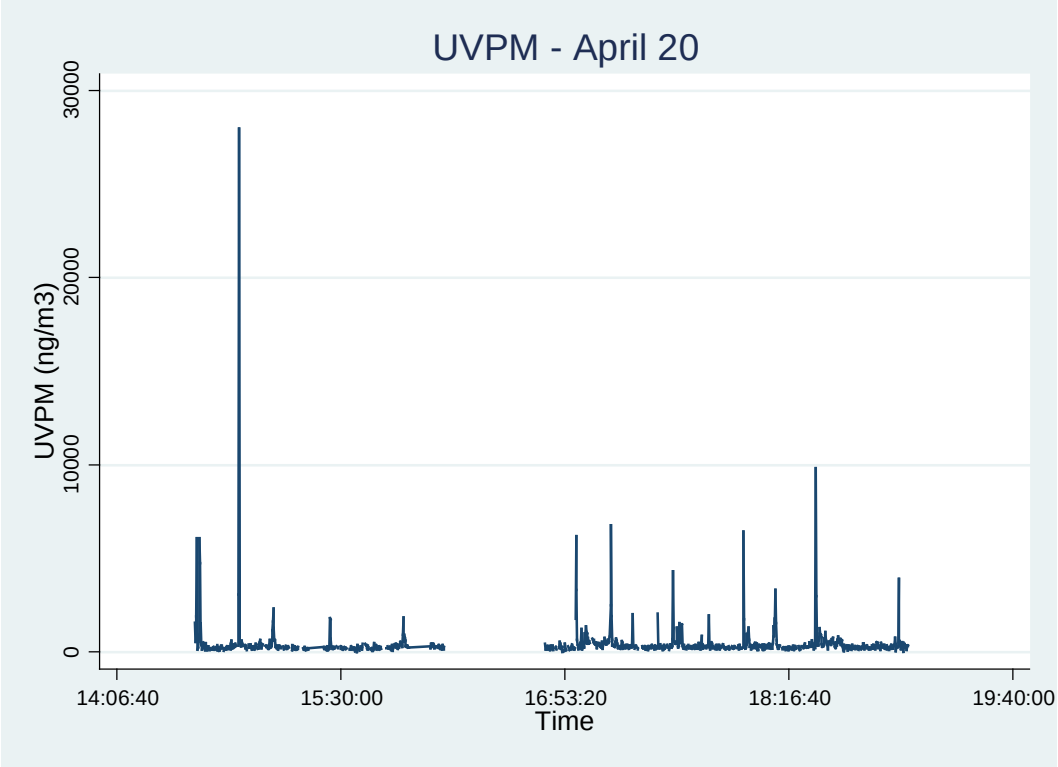

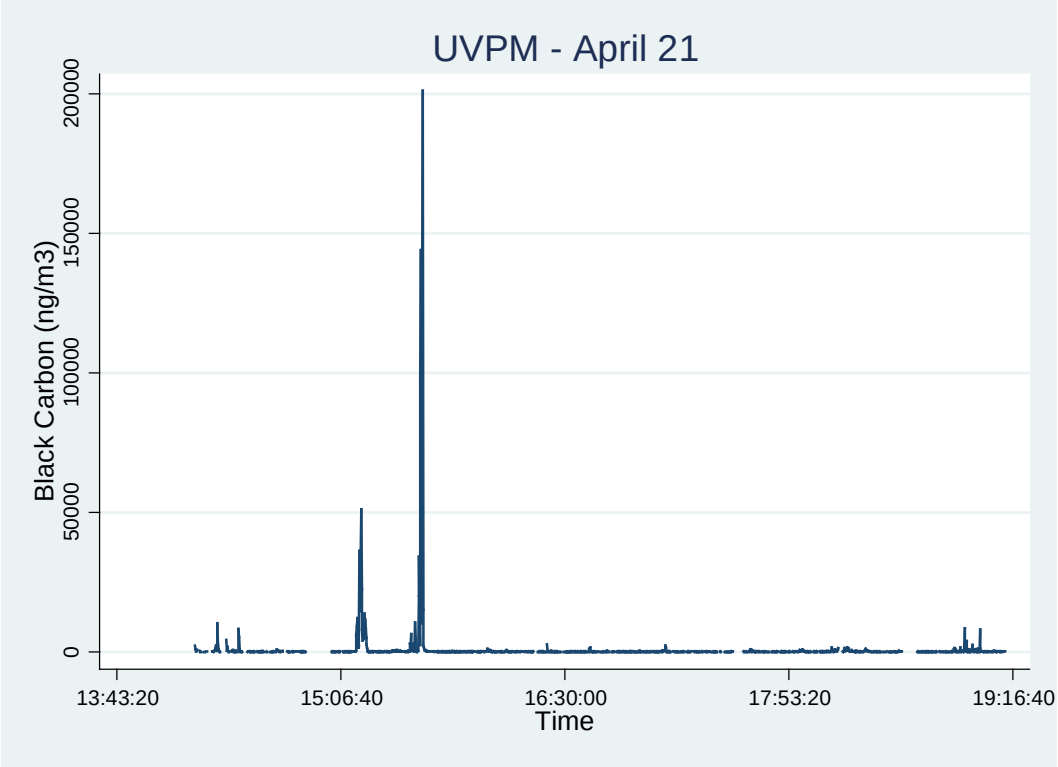

Appendix A12 - Time-Series Plots of the Entire Mobile Monitoring Campaign for Each Sampling Day

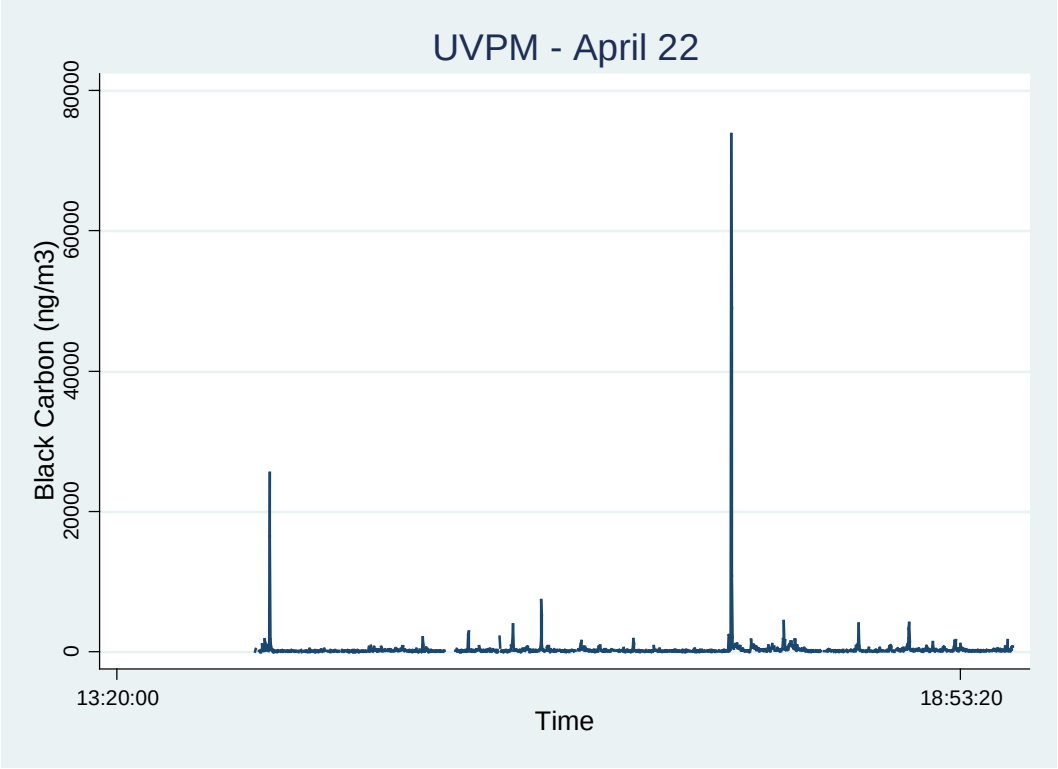

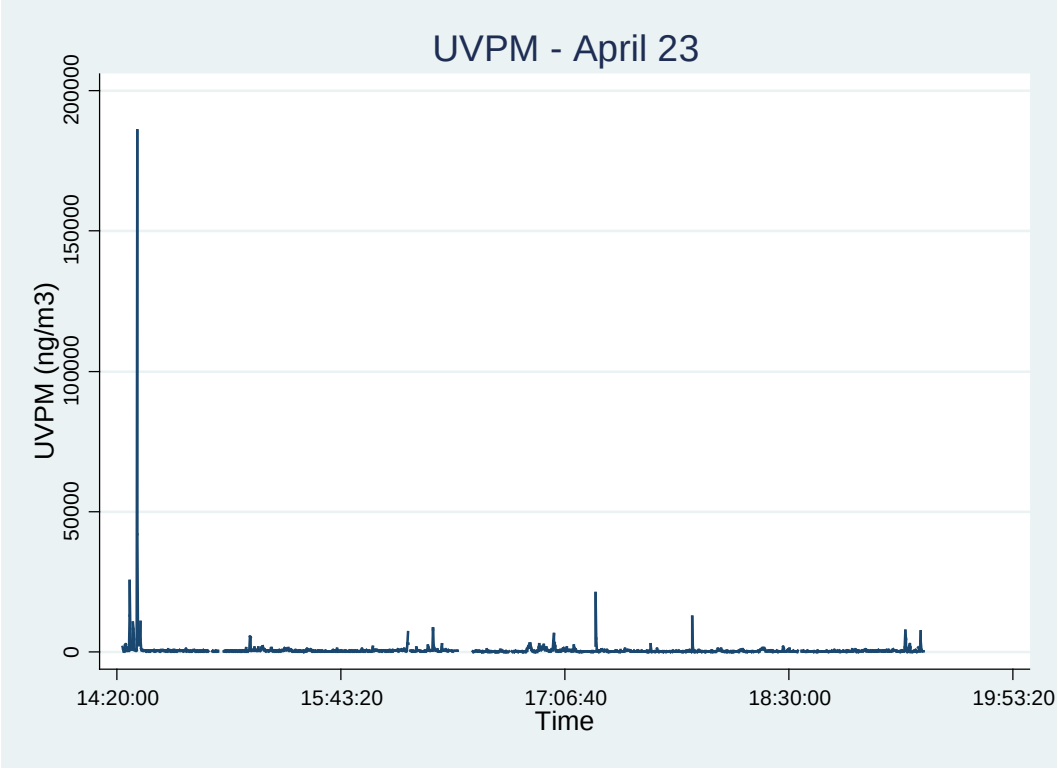

Appendix A12 - Time-Series Plots of the Entire Mobile Monitoring Campaign for Each Sampling Day

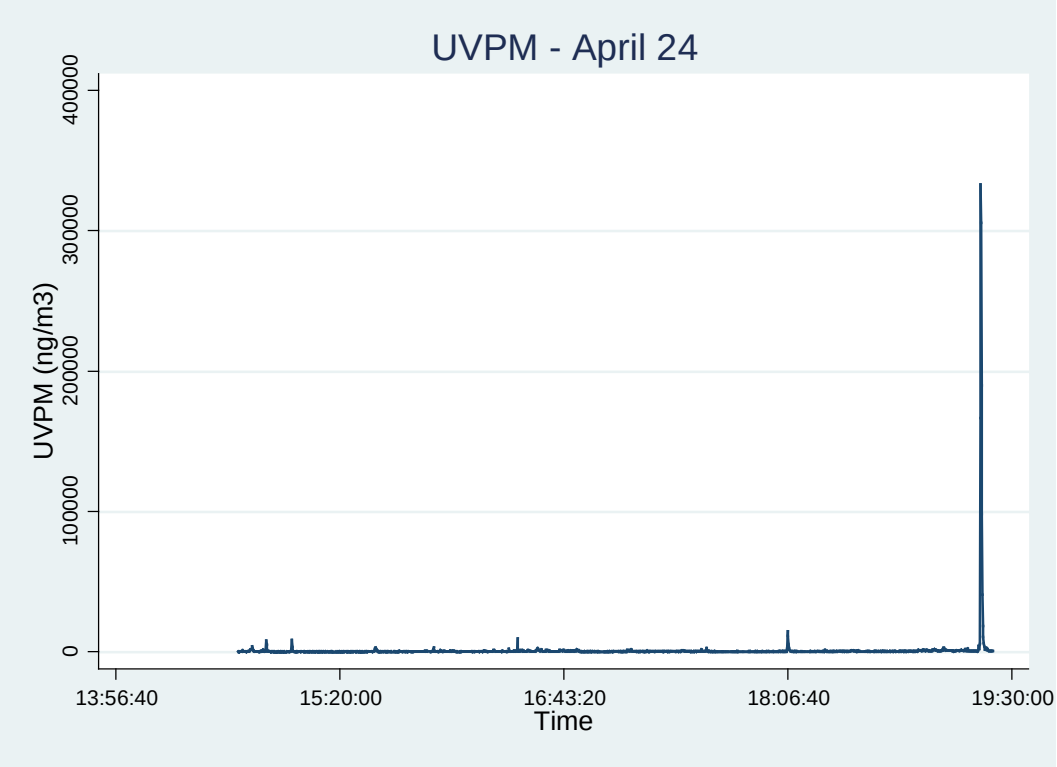

Appendix A13 - Time-Series Plots of the Entire Mobile Monitoring Campaign for Each Sampling Day

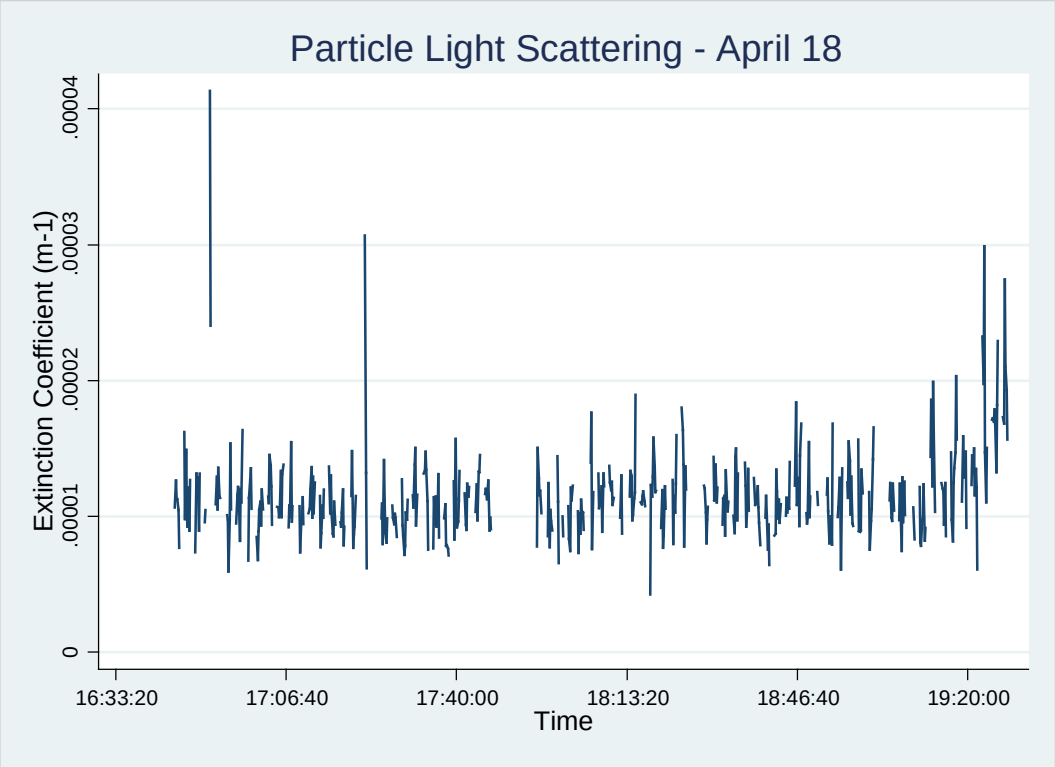

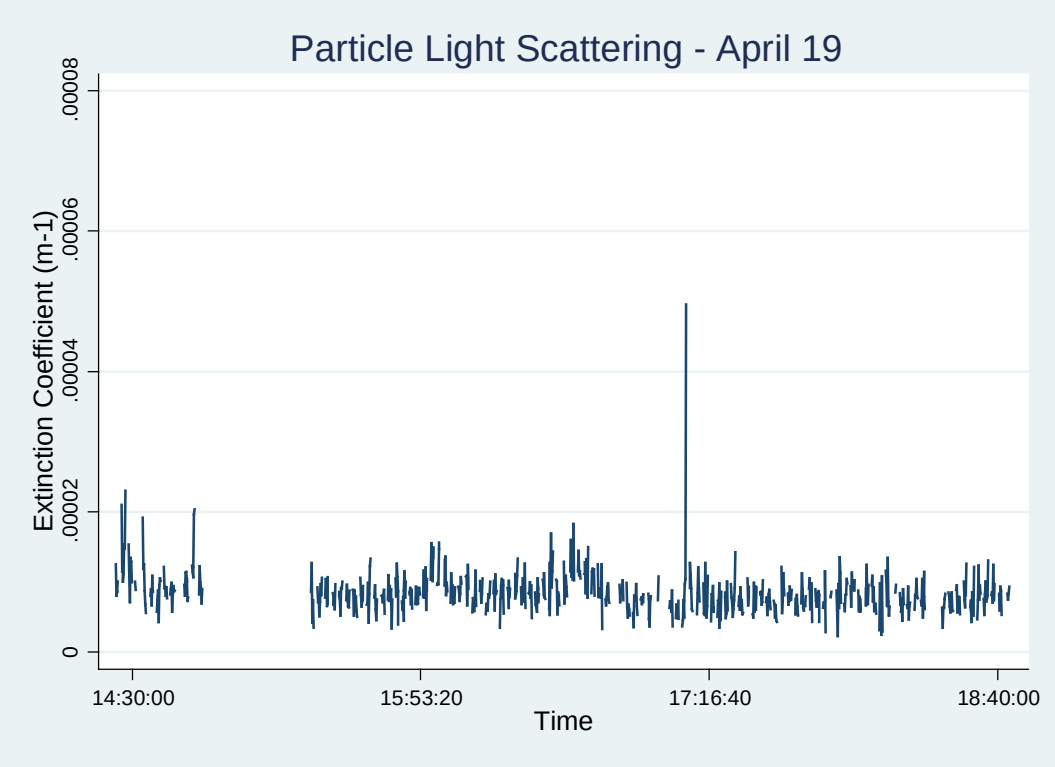

Appendix A13 - Time-Series Plots of the Entire Mobile Monitoring Campaign for Each Sampling Day

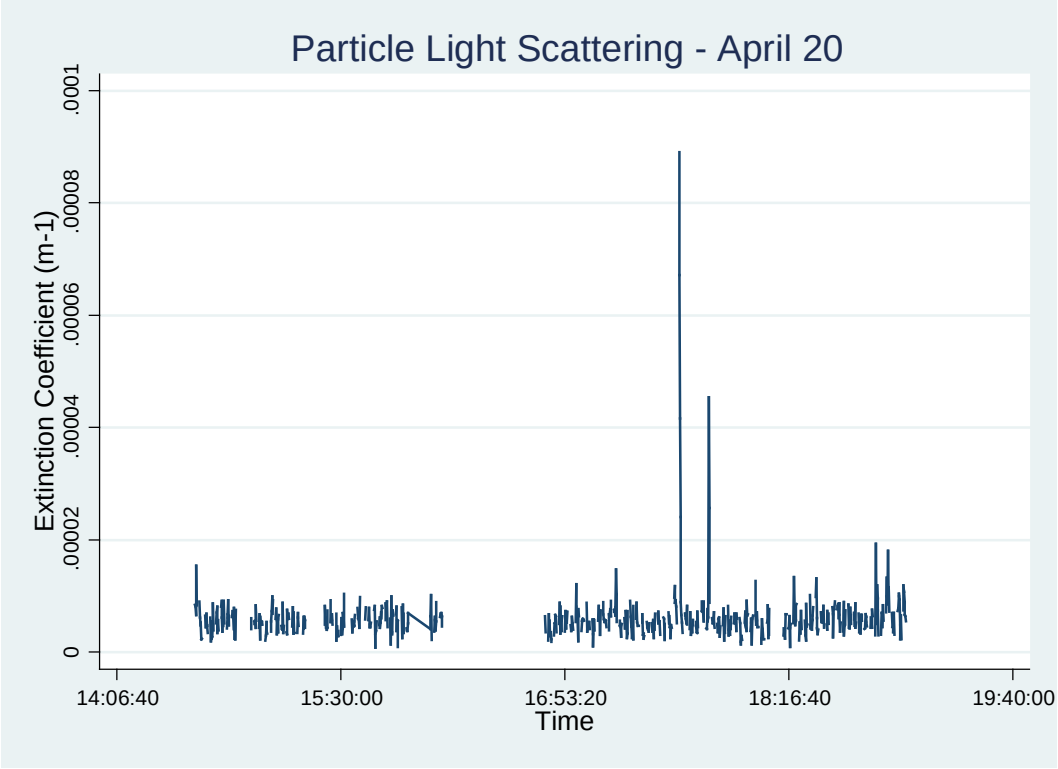

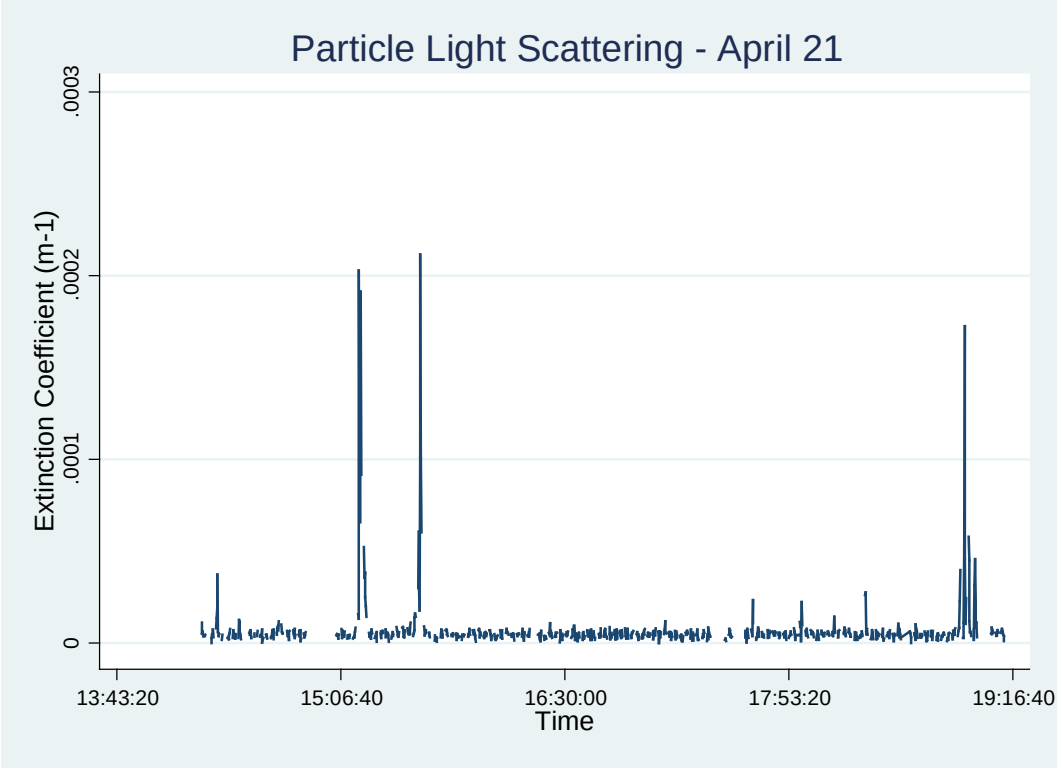

Appendix A13 - Time-Series Plots of the Entire Mobile Monitoring Campaign for Each Sampling Day

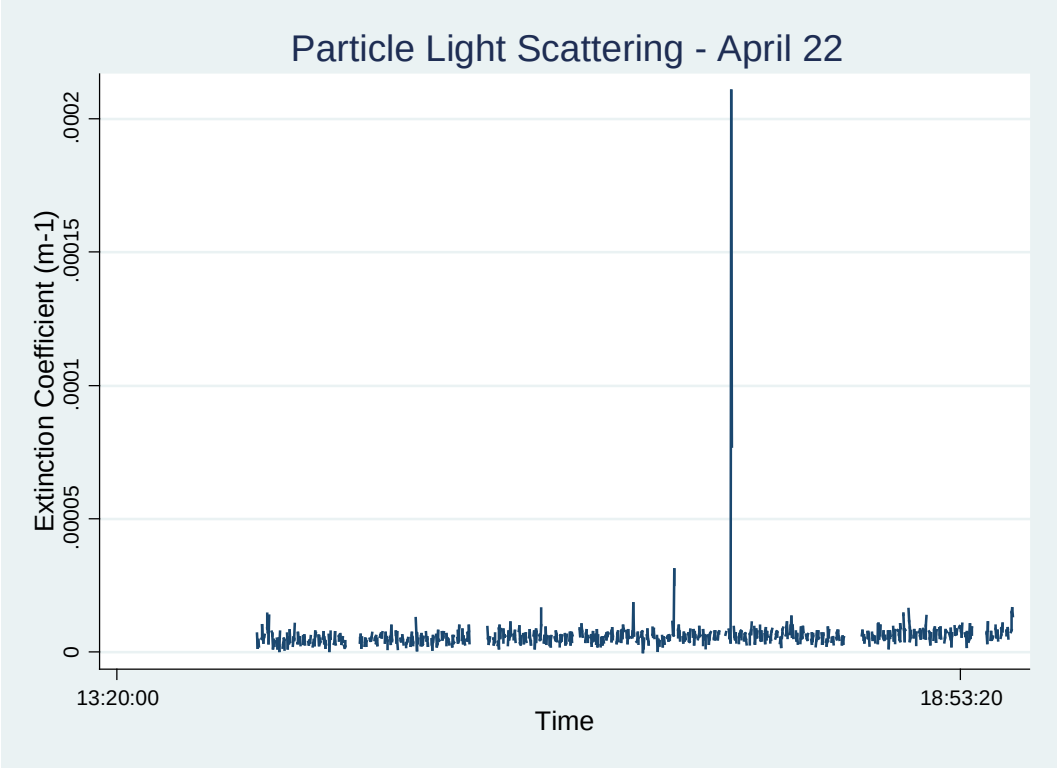

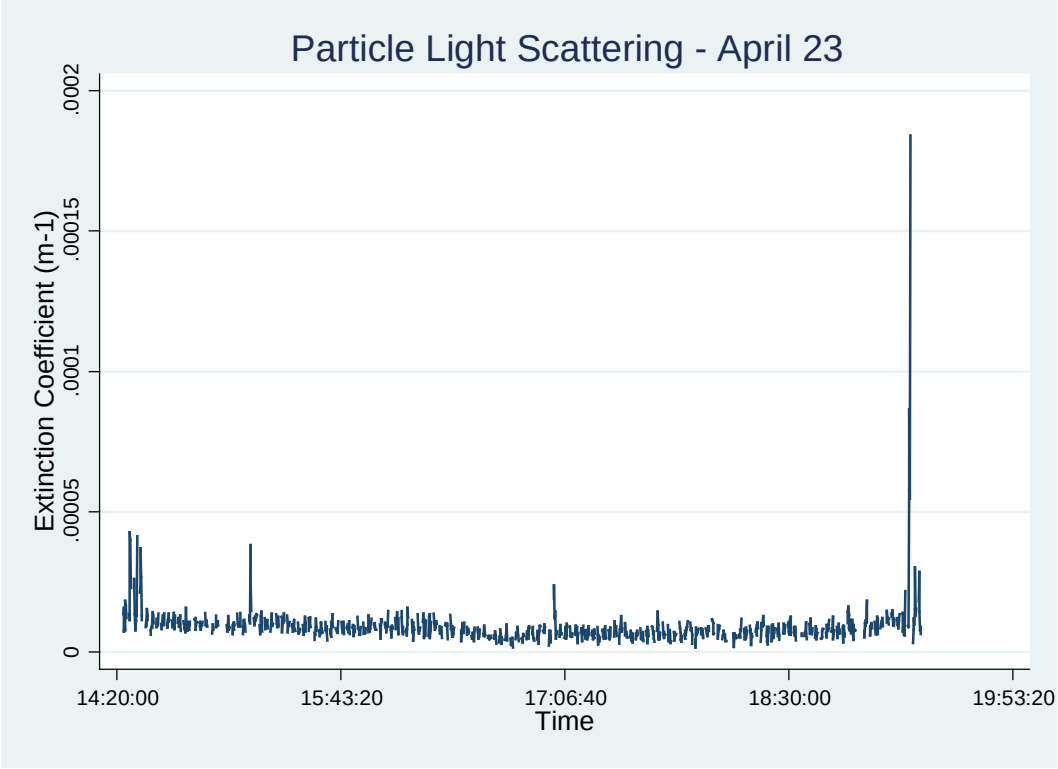

Appendix A13 - Time-Series Plots of the Entire Mobile Monitoring Campaign for Each Sampling Day

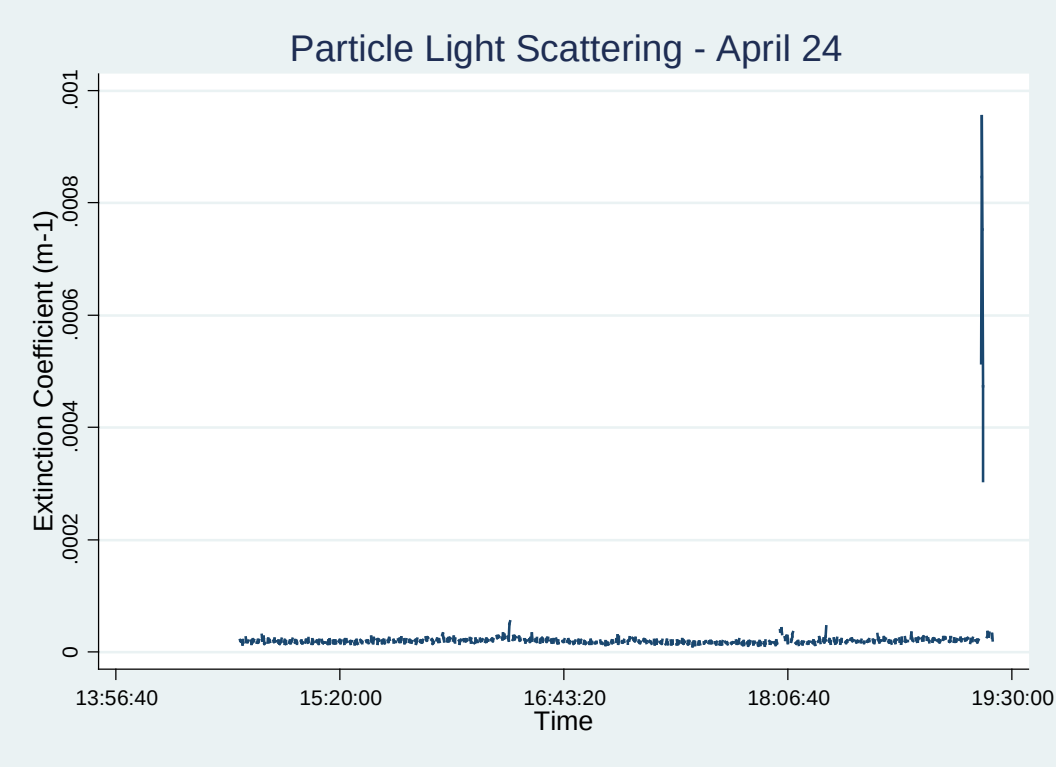

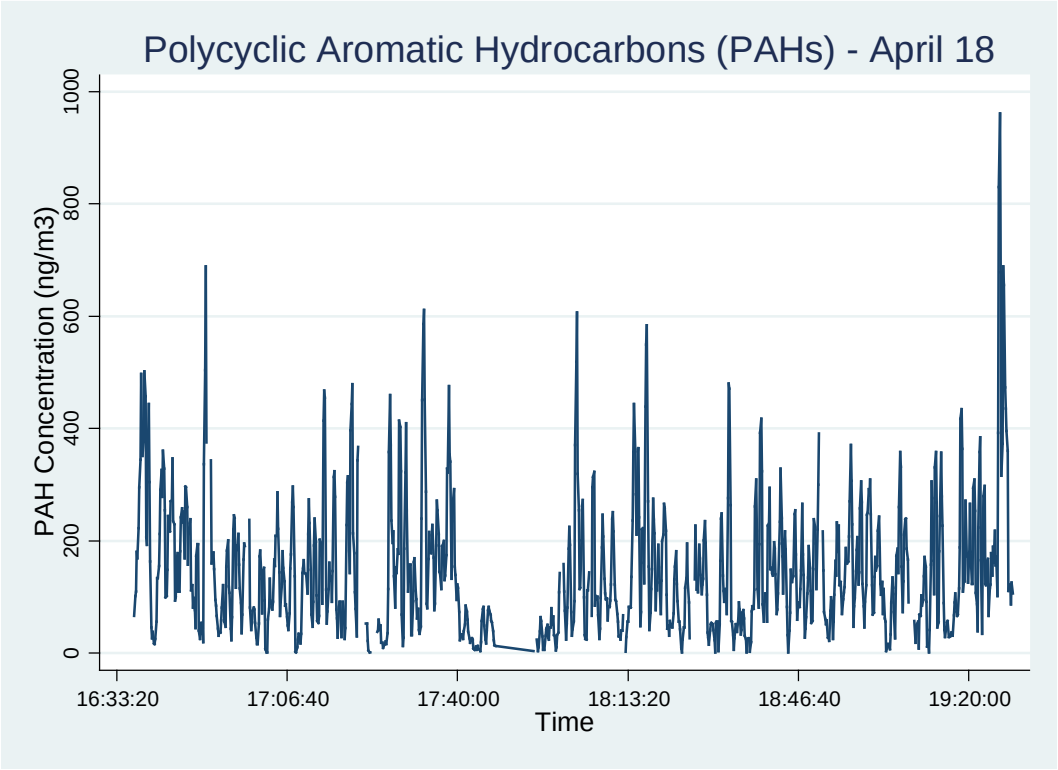
Polycyclic Aromatic Hydrocarbons (PAHs) - April 18
PAH Concentration (ng/m3)
0
200
400
600
800
1000
16:33:20
17:06:40
17:40:00
18:13:20
18:46:40
19:20:00
Time

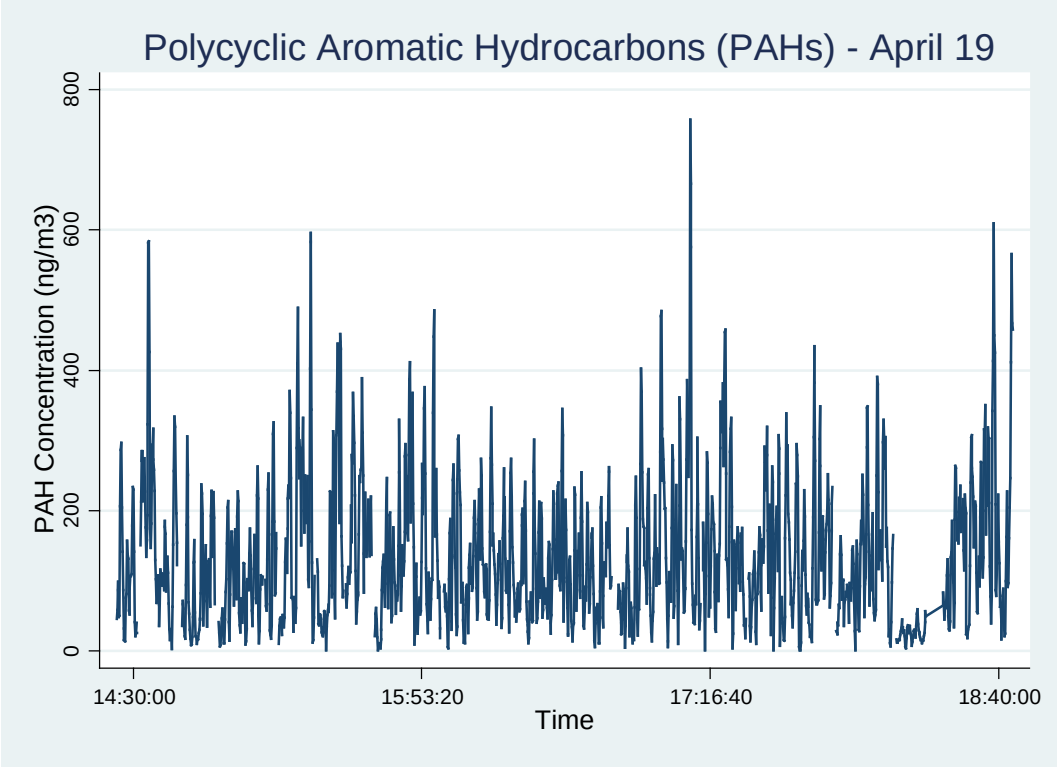
Polycyclic Aromatic Hydrocarbons (PAHs) - April 19
PAH Concentration (ng/m3)
0
200
400
600
800
14:30:00
15:53:20
17:16:40
18:40:00
Time

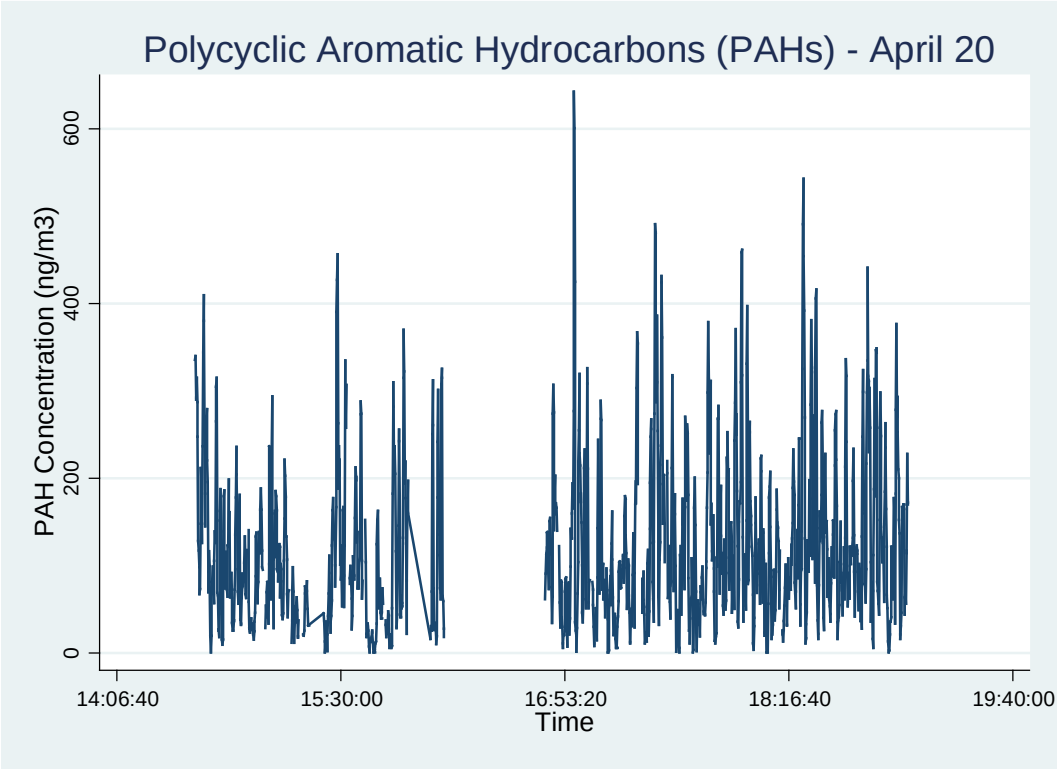
Polycyclic Aromatic Hydrocarbons (PAHs) - April 20
PAH Concentration (ng/m3)
0
200
400
600
14:06:40
15:30:00
16:53:20
18:16:40
19:40:00
Time

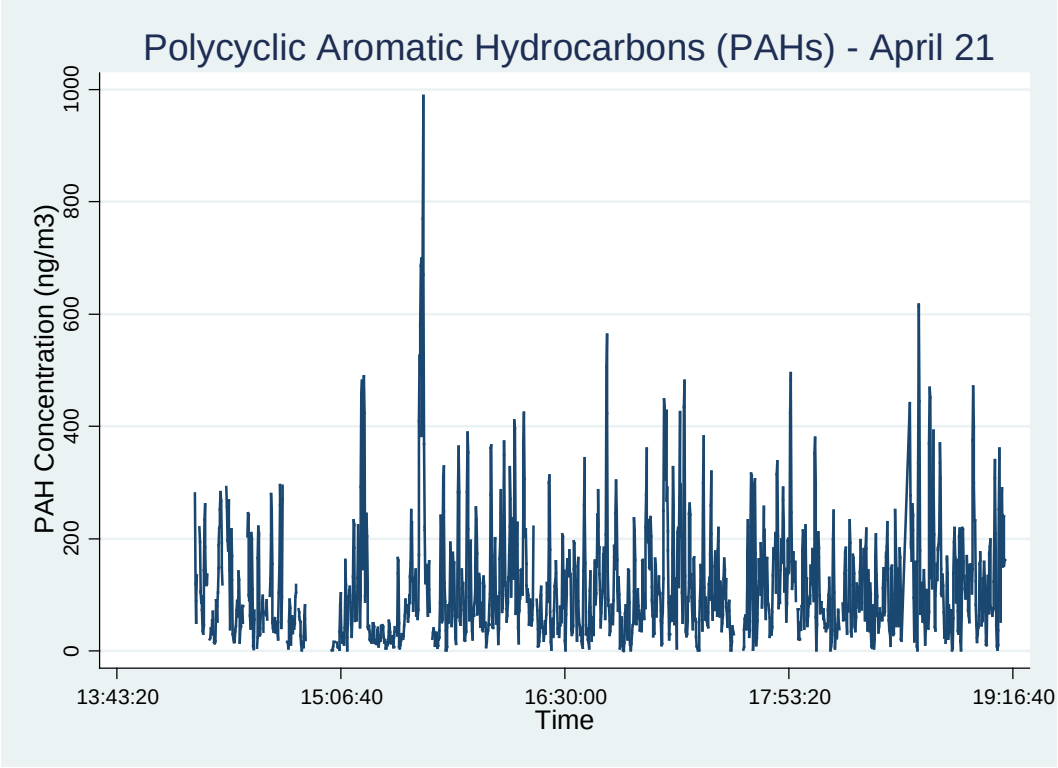
Polycyclic Aromatic Hydrocarbons (PAHs) - April 21
PAH Concentration (ng/m3)
0
200
400
600
800
1000
13:43:20
15:06:40
16:30:00
17:53:20
19:16:40
Time

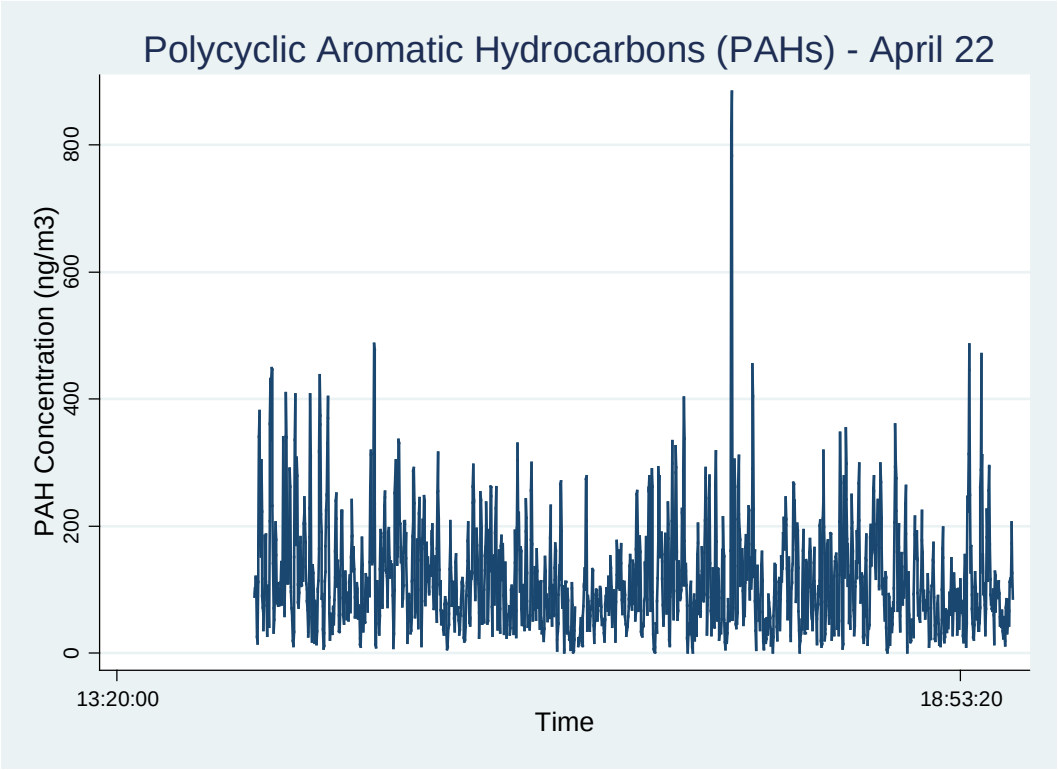
Polycyclic Aromatic Hydrocarbons (PAHs) - April 22
PAH Concentration (ng/m3)
0
200
400
600
800
13:20:00
18:53:20
Time

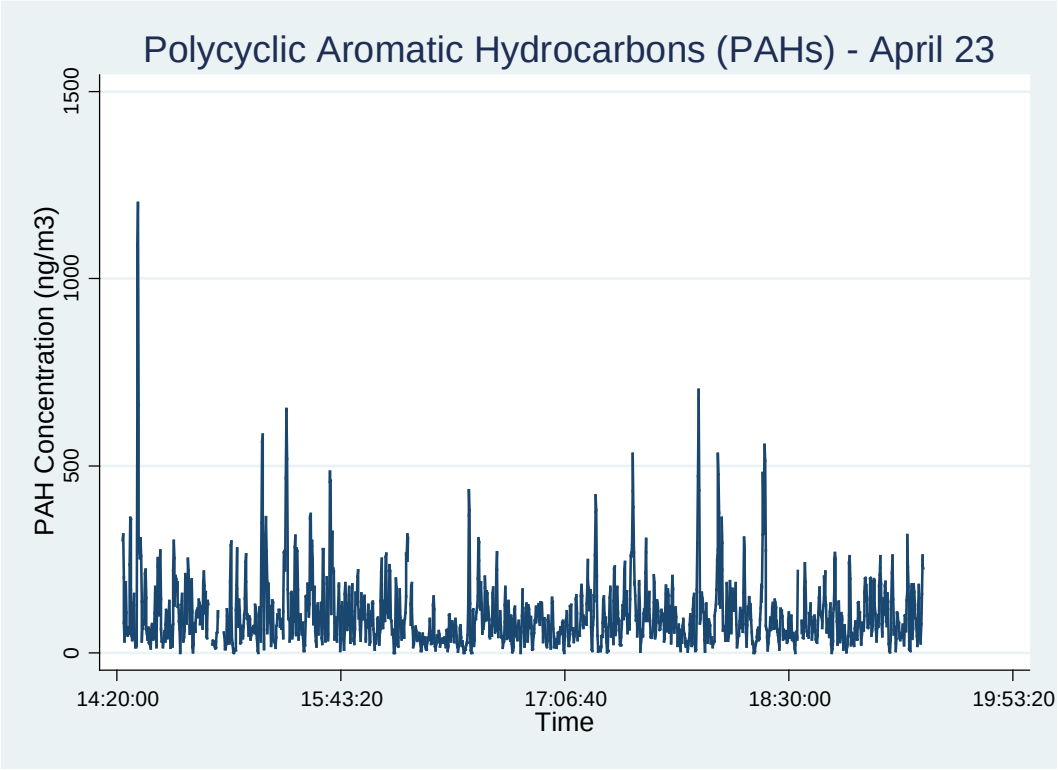
Polycyclic Aromatic Hydrocarbons (PAHs) - April 23
PAH Concentration (ng/m3)
0
500
1000
1500
14:20:00
15:43:20
17:06:40
18:30:00
19:53:20
Time

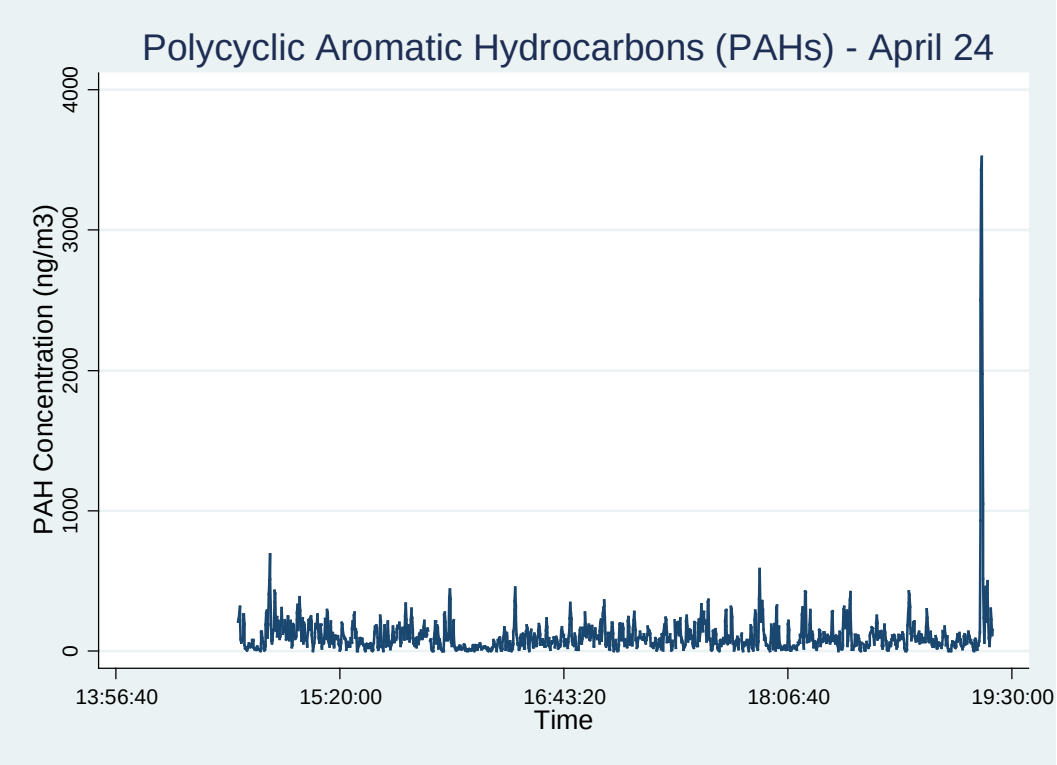
Polycyclic Aromatic Hydrocarbons (PAHs) - April 24
PAH Concentration (ng/m3)
0
1000
2000
3000
4000
13:56:40
15:20:00
16:43:20
18:06:40
19:30:00
Time

Appendix A15 - Time-Series Plots of the Entire Mobile Monitoring Campaign for Each Sampling Day

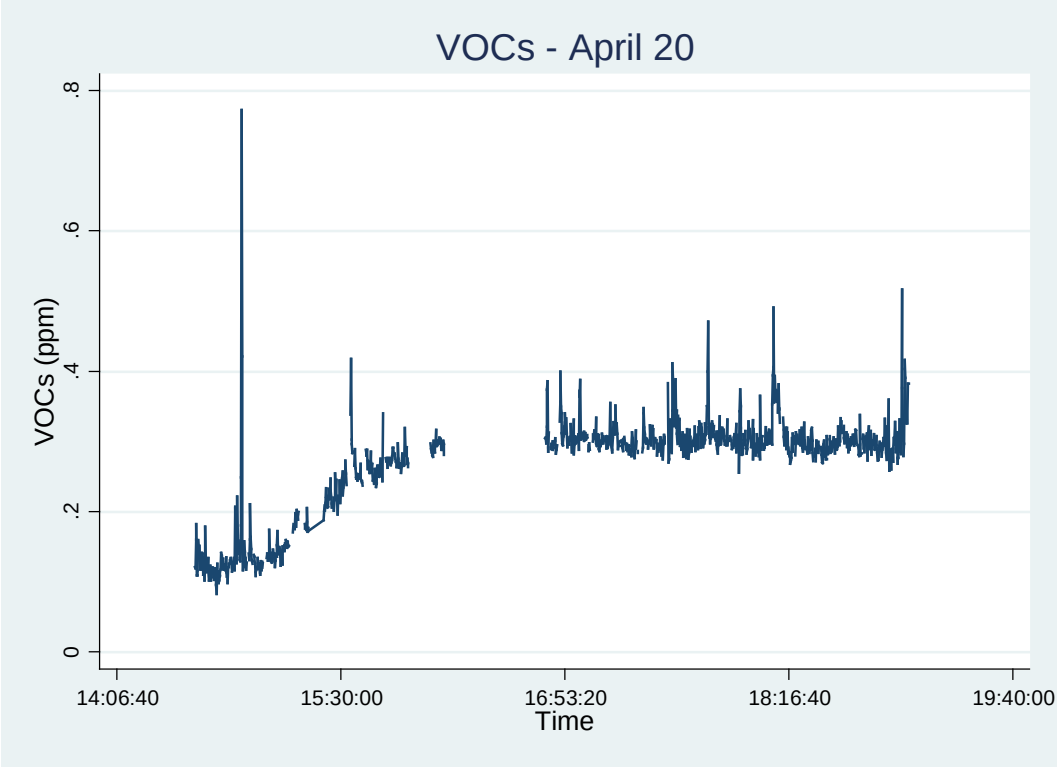

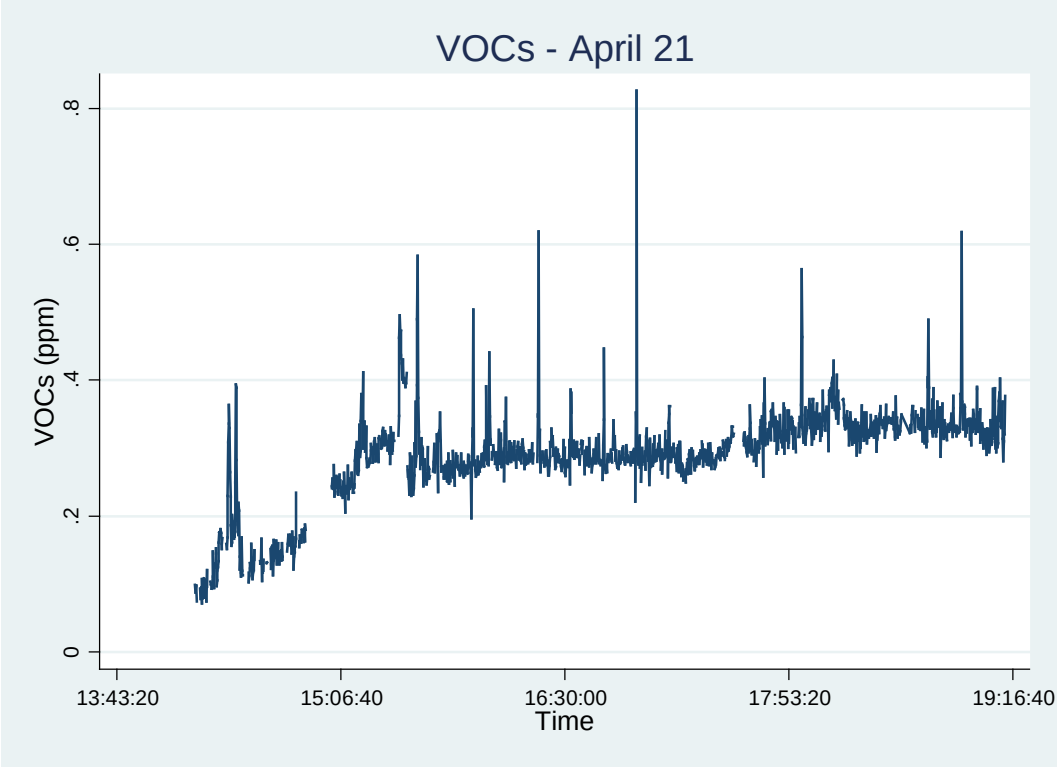

Appendix A15 - Time-Series Plots of the Entire Mobile Monitoring Campaign for Each Sampling Day

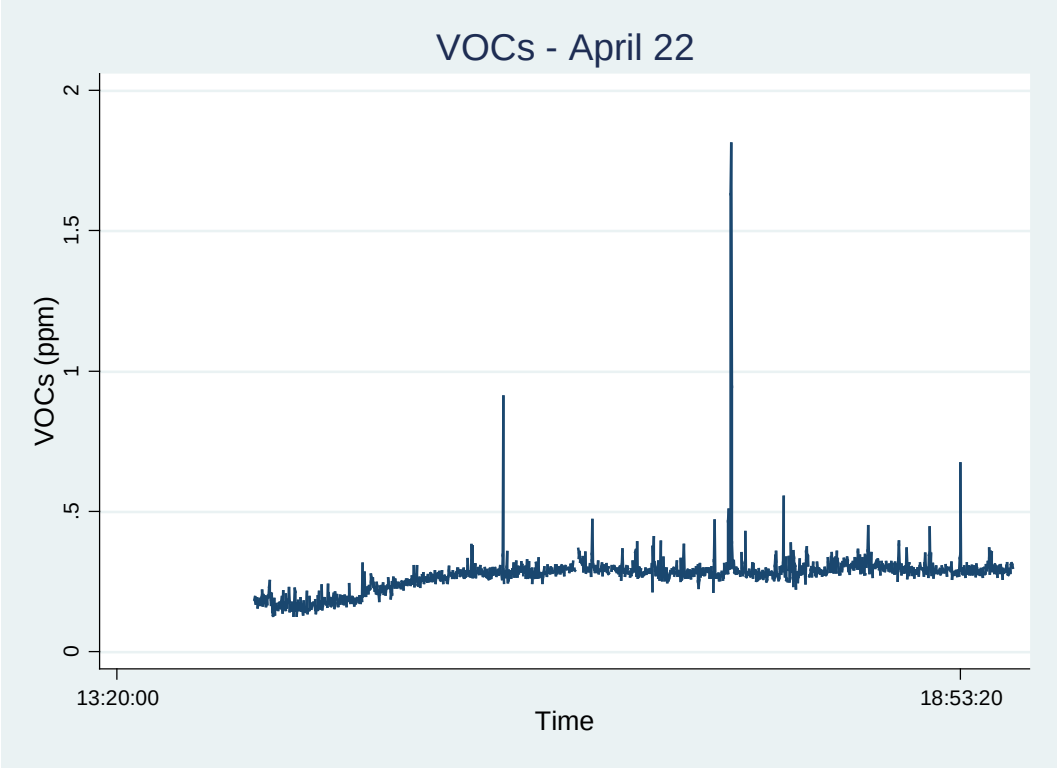

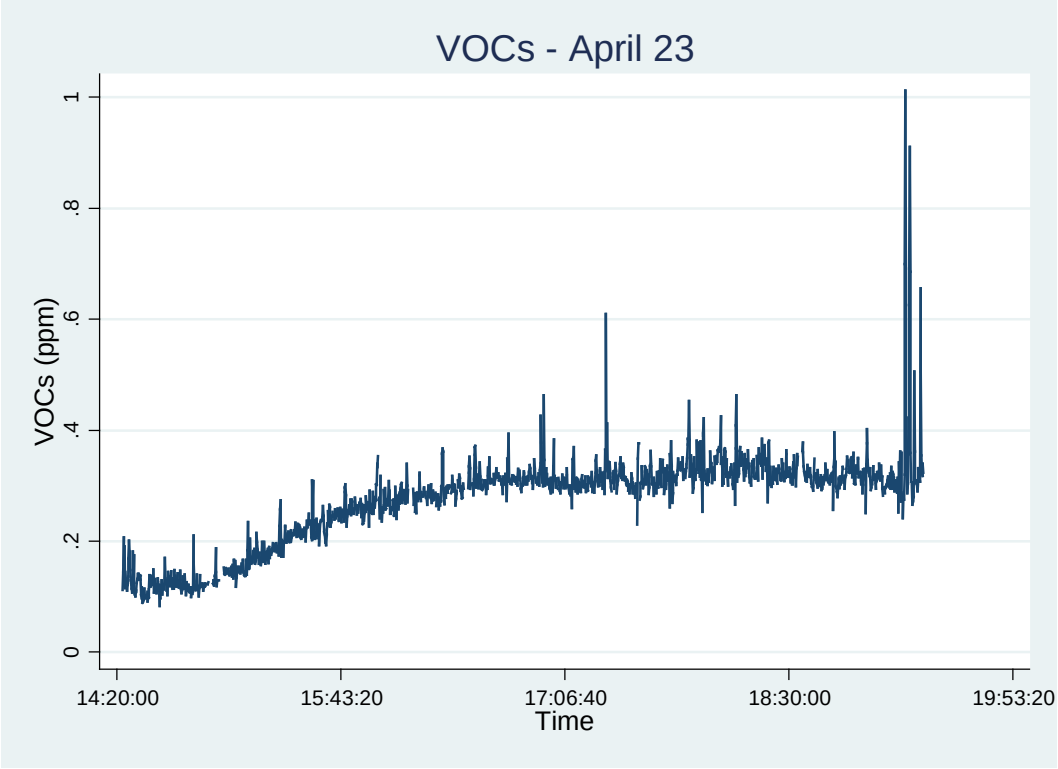

Appendix A15 - Time-Series Plots of the Entire Mobile Monitoring Campaign for Each Sampling Day

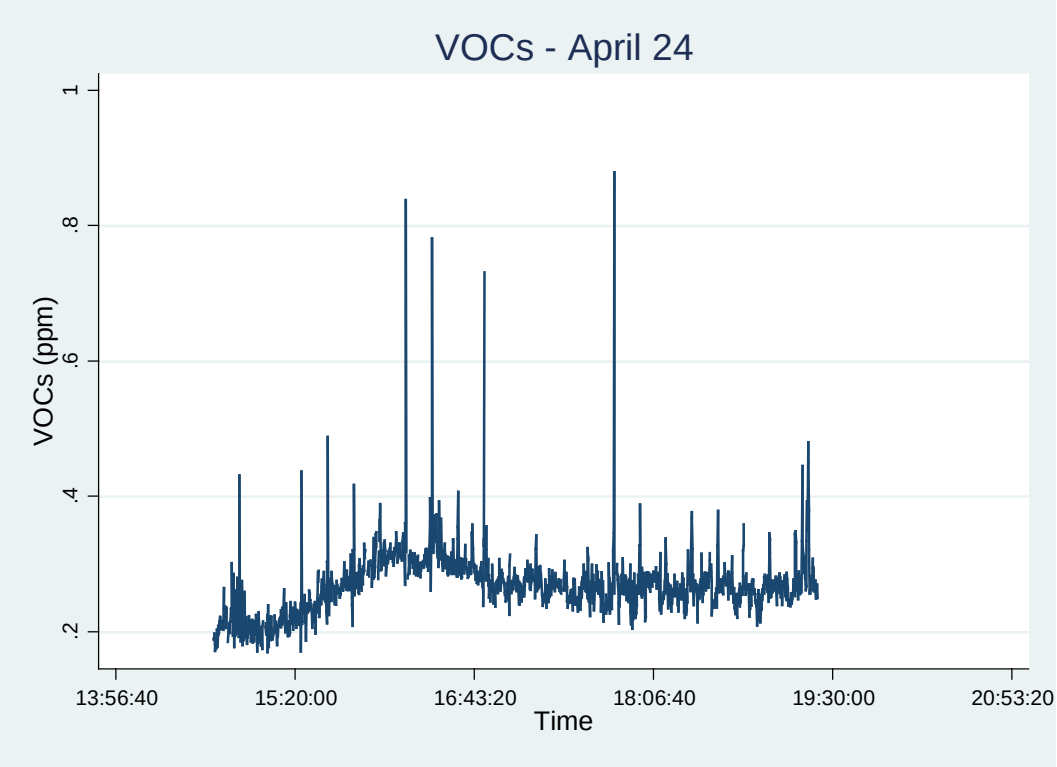

Appendix B

B 1 - AERMOD Generated Dispersion Map (April 18, 2012) for NO_x ($\mu g/m^3$).
Approximate locations of the north and south sampling areas outlined in black.

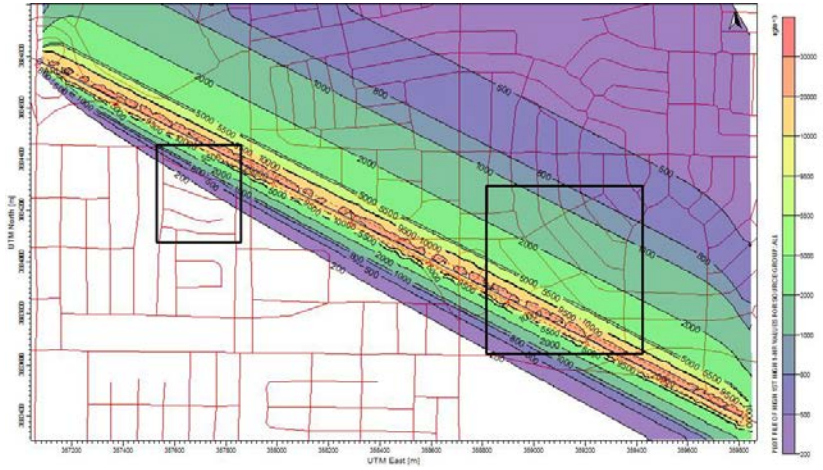

B 2 - AERMOD Generated Dispersion Map (April 19, 2012) for NO_x ($\mu g/m^3$).
Approximate locations of the north and south sampling areas outlined in black.

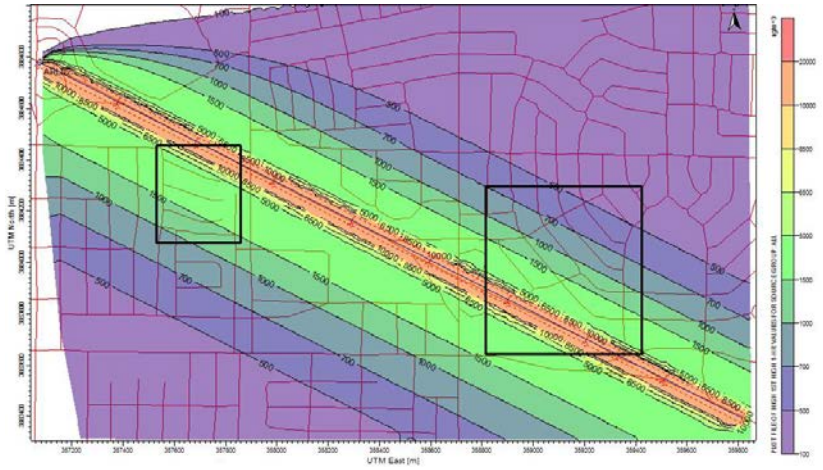

B 3 - AERMOD Generated Dispersion Map (April 20, 2012) for NO_x ($\mu g/m^3$).
Approximate locations of the north and south sampling areas outlined in black.

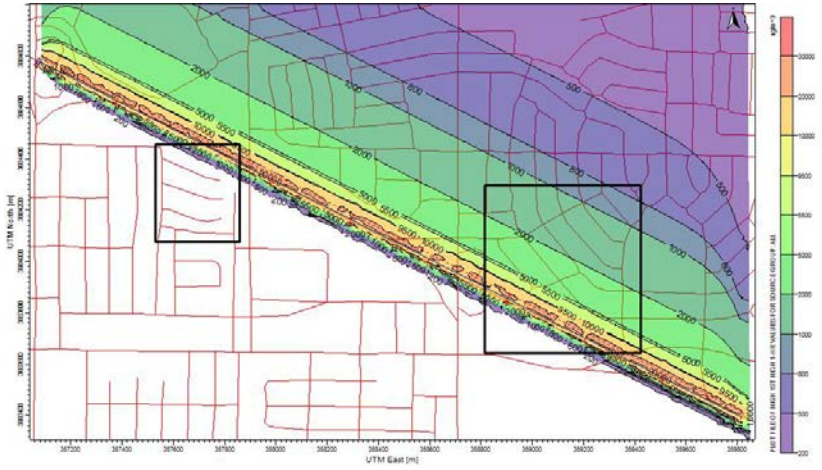

B 4 - AERMOD Generated Dispersion Map for (April 21, 2012) for NO_x ($\mu g/m^3$).
Approximate locations of the north and south sampling areas outlined in black.

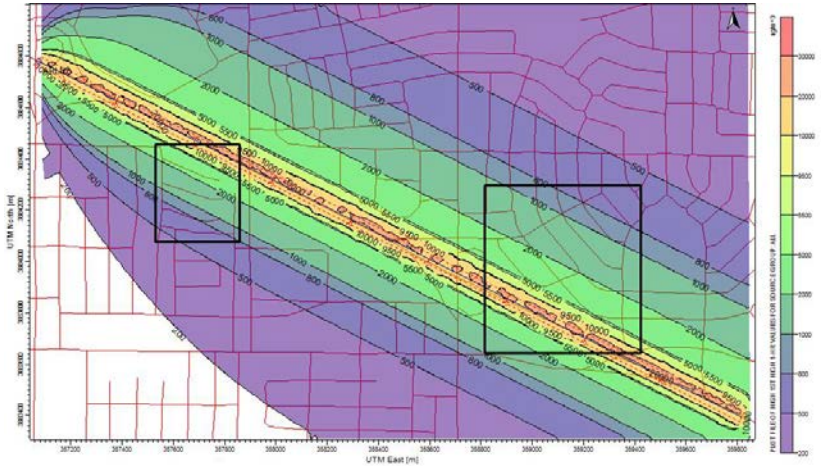

Appendix B

B 5 - AERMOD Generated Dispersion Map for (April 22, 2012) for NO_x ($\mu g/m^3$).
Approximate locations of the north and south sampling areas outlined in black.

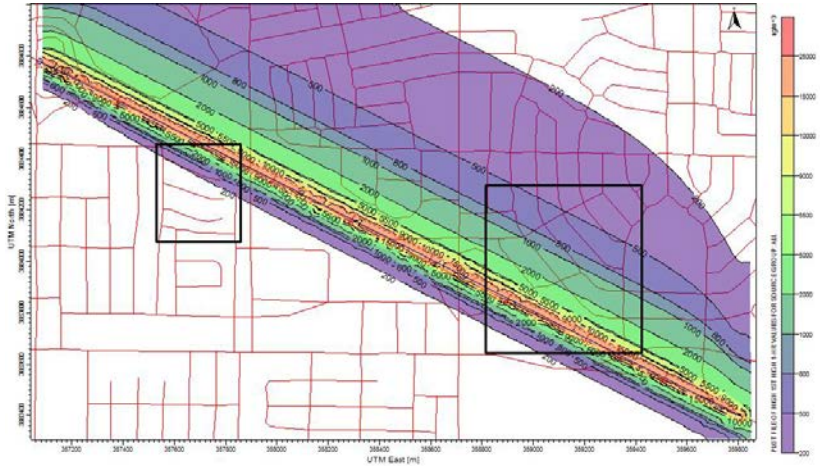

B 6 - AERMOD Generated Dispersion Map for (April 23, 2012) for NO_x ($\mu g/m^3$).
Approximate locations of the north and south sampling areas outlined in black.

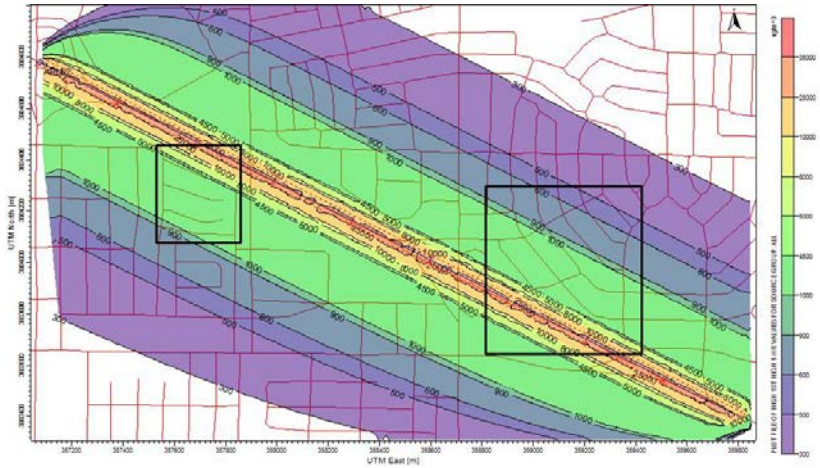

B 7 - AERMOD Generated Dispersion Map for (April 24, 2012) for NO_x ($\mu g/m^3$).
Approximate locations of the north and south sampling areas outlined in black.